# 國立交通大學
# 光電工程研究所
# 碩士論文

# 電壓控制的液晶兆赫輻射用相移器及四分之一波片

# Voltage controlled liquid crystal terahertz phase shifter and quarter wave plate

研究生：陳弘倫

指導老師：潘犀靈 教授

中華民國九十四年七月

# 電壓控制的兆赫輻射用相移器及四分之一波片

# Voltage controlled liquid crystal terahertz phase shifter and quarter wave plate

研究生： 陳弘倫　　Student: Hung-Lung Chen

指導老師： 潘犀靈 教授　　Advisor: Prof. Ci-Ling Pan

國立交通大學
光電工程研究所
碩士論文

A Dissertation
Submitted to Department of Photonics and Institute of Electro-Optic Engineering
College of Electrical Engineering
National Chiao Tung University
In partial Fulfillment of the Requirements
for the Degree of
Master of Engineering

August 2005
Hsinchu, Taiwan, Republic of China

中華民國九十四年八月

# 國立交通大學

## 論文口試委員會審定書

本校光電工程研究所碩士班 陳弘倫 君

所提論文 電壓控制的液晶兆赫輻射用相移器及四分之一波片

合於碩士資格標準、業經本委員會評審認可。

口試委員：賴暎杰　　趙如蘋

賴暎杰 教授　　趙如蘋 教授

洪勝富

洪勝富 教授

指導教授：潘犀靈

潘犀靈 教授

所　長：賴暎杰 教授

賴暎杰 教授

系主任：潘犀靈 教授

潘犀靈 教授

中華民國 94 年 7 月 25 日

# 摘要

我們研製了在兆赫輻射($10^{12}$ 赫茲)波段，以電壓控制其雙折射係數的向列型液晶盒所製作而成的可調式$\pi/2$ 相位調制器及四分之一波片，我們使用了 E7 這種向列型液晶，在 0.2~1.2 兆赫這個波段，E7 的雙折射係數約為 0.17，此外其適用的溫度範圍很大(攝氏-10°~61°)，能夠操作於室溫。我們使用垂直配向的液晶厚樣品，並以銅片作為樣品電極和墊片，以及利用電場控制液晶的排列，讓液晶盒能夠調制相位超過 90 度，因此可將它當作一個兆赫波段的四分之一波片。在頻率為一個兆赫的時候，室溫下 524$\mu$m 的液晶盒操作電壓為 125 伏特(均方根值)，最大的調制角度可達到 92.2°，調制的反應時間分別為 7.5 秒(上升時間)及 373.5 秒(下降時間)，另外此篇論文中，將會描述和比較電控與磁控的相位調制器的特色與優點。

# Abstract

The electrically controlled refractive index in a nematic liquid crystal cell for switchable π/2 phase shifting and quarter wave plate of terahertz wave was demonstrated. We used the nematic LC, E7, which exhibits a birefringence of ~0.17 (0.2~1.2THz), useable at the room temperature range because of the wide nematic range (-10°C~61°C). The thick, homeotropically aligned LC cell with copper sheets used for mylar and electrodes, and the use of electrical field to let the tuning of phase up to 90°, which equivalent a THz quarter wave plate. The maximum phase shift of 92.2° was achieved at 1.00 THz when the interaction length was 524 μm at room temperature. The driving voltage was 125 V (rms), the rise time and fall time of the cell are 7.5 seconds and 373.5 seconds, respectively. Additionally, characteristics and advantages of electrically and magnetically controlled THz phase shifter are described and compared in this thesis.

# Acknowledgement (誌謝)

兩年過得很快，卻讓我留下很多回憶，在老師的帶領，以及同學們的陪伴下，我的碩士班生涯相當的多采多姿，所得到的絕對不僅是學術方面的成長，當然最感謝的是帶領我們的潘犀靈教授和給予我教導的每位老師，在功課、實驗、觀念、日常生活都給予我相當多指導的謝卓帆、陳昭遠、劉子安、李晁逵、王怡超、陳晉瑋學長及藍玉屏學姊，同年級的 cc、小高、小冷、阿隆、羅誠、宗翰、澎澎，學妹乃今，以及趙如蘋老師所帶領的液晶實驗室的學長學弟，對你們每一位我都有說不完的感謝。另外，當然還要感謝全力支持我的父母、親戚、朋友們，我能這麼順利的一路走來，都是因為有你們的陪伴，能夠有現今的成就，絕大部份的功勞都應該屬於你們，真的是…千言萬語也說不盡我的感謝，得到碩士學位，象徵著另一個人生目標的達成，而我現在最大的願望，就是能和大家分享我的喜悅。

# Contents

# List of Figures and Tables

# 1. Introduction

In chapter 1, we introduce terahertz (THz) wave and liquid crystals (LCs), about their history, characteristics, and applications, additionally; former works of our group are also described.

In recent years, the importance of terahertz wave has significantly increased. The terahertz region of the electromagnetic spectrum exists from frequencies of about 300 GHz to 10 THz ($10 \times 10^{12}$ Hz) [1] as shown in Fig. 1.1, i.e., in the region between visible light and radio waves. This corresponds to wavelengths between about 1 and 0.03 mm, so THz can be also called sub-millimeter wave because its wave length is shorter than millimeter wave's. The former limit lies just above the microwave region where satellite dishes and mobile phones operate, whereas the latter limit is located adjacent to infrared frequencies used in devices such as television remote controllers.

At lower frequencies, microwaves and millimeter-waves can be generated by "electronic" devices such as those found in mobile phones. At higher frequencies, near-infrared or visible light is generated by "optical" devices such as semiconductor laser diodes, in which electrons jump across the band gap of semiconductor and emit light.

In physics, THz wave is a very important band of frequency spectrum. In the real world, the region is of great importance to the spectroscopy of condensed matter; for example, the electronic properties of semiconductors and metals are much affected by the bound states whose energies fall in the terahertz frequencies [2], i.e., many band gaps which relate material behaviors are contained, It can show the information of matters, which light at other frequencies can't observed. THz wave can also be applied in radio astronomy [3], telemeter, and medical image. With high speed information age approaching, high-speed devices are needed, which cause the devices should be operated at higher operating frequency. THz also acts the indispensable role.

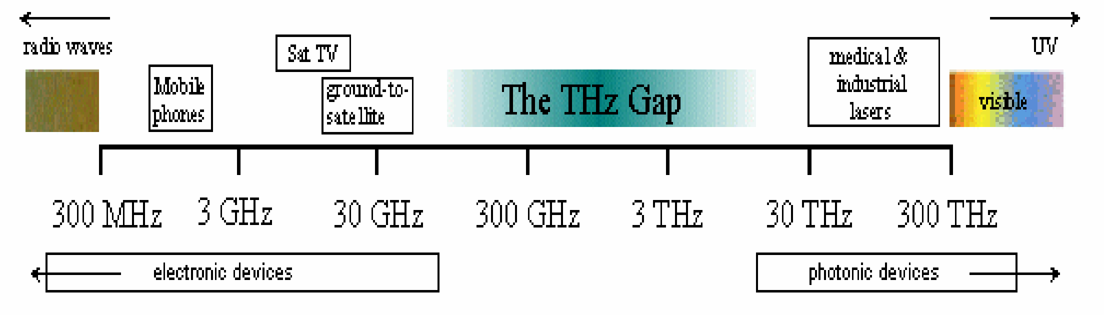

Fig. 1.1 Electromagnetic spectrum

http://www.frascati.enea.it/THz-BRIDGE/

However, neither electronic nor optical devices can conveniently be used in the terahertz region, because not only conventional microwave sources can not work fast enough to produce radiation efficiently in the range between microwaves and infrared light, but also laser diode sources have been limited by thermal effects [4].

Formerly, only Fourier Transform Infra-Red (FTIR) spectroscopy can be used in this region, but unfortunately lacked the brightness of incoherent sources and the functions to measure the real and imagine parts of response functions at a certain frequency are its weaknesses. Therefore, the development of terahertz spectroscopy has been hindered without suitable tools. This situation became better in the 80's with the appearance of ultrashort pulse lasers of ~100 fs pulse duration. Ultrashort pulses can generate broadband THz radiation when they impinge on semiconductors. Recently, advances in ultrafast pulsed laser technology have led to the generation and detection of broad bandwidth terahertz light, Mourou and Auston [5-6] first demonstrated generation and detection of pulsed THz radiation by photoconducting switch with advantages of time resolution of picosecond and sensitivity enhanced by phase-lock technique. In 1996, Zhang et al. [7] developed free-space electro-optic sampling (FS-EOS) technique to enhance signal to noise ratio (S/N ratio) up to 10000 and to achieve much large dynamic range. These techniques have now developed to a level for spectroscopy and sensing. The spectroscopic technique using pulsed THz radiation is called "THz time-domain spectroscopy (THz-TDS)".

THz wave has infinite potential in application of science, therefore our group actively researches many aspects of the application in THz region, for example, biological burned skin measurement, THz communication, and THz image [2], etc. But for further advances in many of the above applications, variety of active and passive THz optical elements are required, such as polarizers, attenuators, detectors, modulators and phase shifters. But, these elements are rarely explored up to now; therefore, the research and development of THz optical components are very important and clamant.

In recent years, liquid crystals [8-10] have been applied in many regimes because its birefringence and the easily changing refractive index by electric or magnetic field. Although it is well known that optical properties of liquid crystals, which are usually used in display devices, alter by applying an electric field to them, their dielectric properties in other frequency ranges are un-neglected. The measurement results of the liquid crystal in microwave and millimeter-wave ranges show that the loss was relatively small and that the liquid crystal possessed a uniform and alterable permittivity over these ranges. Therefore, lots of applications have been demonstrated, for example, fig.1.2 shows the structure of a micro variable phase shifter (published by NHK, Japan Broadcasting Corporation) using liquid crystal. By filling the spacing between the strip line and the ground plane with the liquid crystal, a microwave transmission line can be made. The permittivity of the liquid crystal alters when a bias voltage is applied between the strip line and the ground plane. The signal velocity propagating along the transmission line alters as the permittivity changes, and so the device shown here operates as a variable phase shifter. Our group also discovered various applications by utilizing liquid crystal, for example, liquid crystal THz phase shifter, liquid crystal THz filter, tunable multi-wavelength active mode-locked semiconductor laser with a liquid crystal pixel mirror, etc.

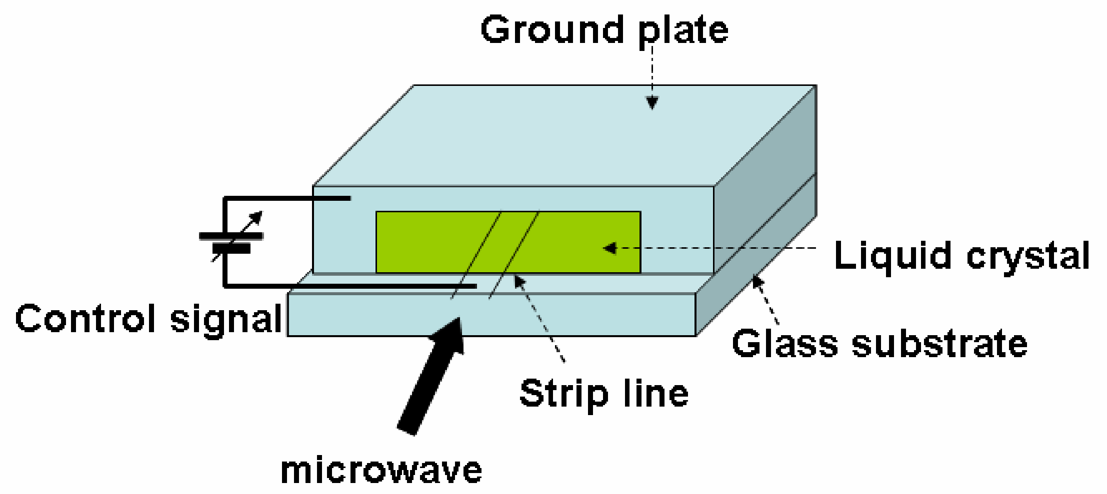

Fig. 1.2 Microwave phase shifter

In THz range, the relationship between frequency and refractive index of one kind of liquid crystal, E7 (Merck) have been researched by our group, these results demonstrate the feasibility of the liquid crystal application in THz region, then, the relationship between temperature and refractive index in THz range were discovered, in consequence, the development of THz optical components is more practical. For optical modulation, phase shifter is a fundamental and important component, but in THz range, tunable range of the former work are too narrow（<40°）and they should be operated at low temperature（<-100°C）[11-13], in order to extend the application, bigger shift angle and higher operating temperature are necessary.

In following chapters, the electrically controlled refractive index in a nematic liquid crystal cell for $\pi/2$ phase shifting of terahertz region will be explained in detail. In chapter 2, we mainly describe theories of terahertz field, liquid crystal, and phase shifters; in chapter 3, our experimental setup, sample fabrication and data processing method are expressed; and then we show our experimental results and discussion in chapter4; at last, we make a conclusion in chapter 5.

# 2. Terahertz Field, Liquid Crystal, and Phase Shifters

We divide this chapter into three parts; in section 2.1 we describe mechanisms of generation and detection of THz radiation. And then, theories of liquid crystal and phase retardation used to draw the theoretical curve are recounted in detail; then we present some relative characteristics of LC in section 2.2, including nematica phase, birefringence, external influence, threshold voltage, phase retardation and its application; at last we express many kinds of phase shifters in section 2.3.

## 2.1 Basics of Generation and Detection of THz beam

Generally, people generate and detect THz radiation by using photoconductive (PC) antennas or electro-optic (EO) materials illuminated with fs laser pulses. Compare with the PC antennas method, EO materials can produce broader bandwidth THz radiation but great lower efficiency of energy conversion. In our experiment, only PC antennas are used, in the following sections, its mechanisms of generation and detection is introduced.

### 2.1.1 Generation of THz Radiation Using PC Antennas

When a femtosecond (fs) laser excites a biased semiconductor with photon energies greater than its bandgap, electrons and holes are produced at the illumination point in the conduction and valence bands, respectively. With the help of an antenna, Fast changes of the density of photocarriers and the acceleration by dint of the applied dc bias ($V_b$)

produce an electromagnetic field radiation. The carrier lifetime in the semiconductor decides the production of ultrashort currents with a full-width half-maximum (FWHM) of 1ps or less strongly [14].

The carrier density behavior in time is given by

$$\frac{dn}{dt} = -\frac{n}{\tau_t} + G(t) \tag{2.1}$$

where $n$ is the carrier density and $G(t) = n_o \exp(\frac{t}{\Delta t})^2$ is the generation rate of carriers due to laser pulse excitation, with $\Delta t$ the laser pulse width, $n_0$ the generated carrier density at $t = 0$, the carrier lifetime $\tau_t$ can be engineered by modifying the annealing temperature for LT-GaAs. The generated carriers are accelerated by the electric field bias with a velocity rate given by

$$\frac{dv_{e,h}}{dt} = \frac{-v_{e,h}}{\tau_{rel}} + \frac{(q_{e,h}E)}{m_{eff,e,h}} \tag{2.2}$$

where $v_{e,h}$ is the average velocity of the carrier, $q_{e,h}$ is the charge of the electron and hole, $\tau_{\mathrm{rel}}$ is the momentum relaxation time, and $E$ is the local electric field, which is less than the applied bias $E_{\mathrm{b}}$ due to the screen effect of space charges. More precisely,

$$E = E_b - \frac{P}{3\varepsilon_r} \tag{2.3}$$

where $\varepsilon_r$ is the dielectric constant and $P$ is the polarization induced by the separation of electrons and holes. The polarization depends on time according to the expression.

$$\frac{dP}{dt} = -\frac{P}{\tau_{rec}} + J \tag{2.4}$$

where $\tau_{\mathrm{rec}}$ is the recombination time between electrons and holes ($\tau_{\mathrm{rec}}$ = 10 ps for LT-GaAs) and $J = env_h + (-e)nv_e$ is the current density. The far-field radiation is given by

$$E_{THz} \propto \frac{\partial J}{\partial t} \propto ev\frac{\partial n}{\partial t} + en\frac{\partial v}{\partial t} \tag{2.5}$$

where $v = v_e - v_h$. The transient electromagnetic field $E_{\mathrm{THz}}$ consists of two terms: the first term describes the carrier density charge effect while the second term describes the effect of charge acceleration due to the electric field bias.

### 2.1.2 Detection of THz Radiation Using PC Antennas

The electric field of a Gaussian beam on the detector [15] as shown in Fig. 2.2 can be expressed as:

$$E(x,y) = E_o \exp[\frac{-(x^2 + y^2)}{w_1^{\ 2}}] \tag{2.6}$$

where $w_1$ is spot size. The total resistance over the detector is:

$$R = \frac{\rho_M L_M + \rho_s L_S}{td} \approx \frac{\rho_s L_S}{td} \tag{2.7}$$

where $L_M$ is the total length of the metal electrodes, $L_S$ is the length of the switch area between the two electrode tips, $\rho_M$ and $\rho_S$ are their resistivities, respectively, and $d$ is the width of the electrode and the gap area. The average resistivity $\rho_S$ is much larger than $\rho_M$ owing to the low duty cycle of the driving laser (100 fs/10 ns $=10^{-5}$). The resistivity $\rho_S$ depends on the photogenerated carrier density, which for homogeneous illumination of power $P_{\mathrm{laser}}$ scales as

$$\rho_s = \frac{L_S d}{\xi \cdot P_{laser}} \tag{2.8}$$

where $\xi$ is a conversion factor between laser power and number of photogenerated carriers. The average field strength $\overline{E}$ across the detector gives rise to a potential difference $U = \overline{E}(L_M + L_S)$, so the average current is

$$I = \frac{U}{R} = \frac{\overline{E}(L_M + L_S)}{{L_S}^2} td\xi \cdot P_{laser} \tag{2.9}$$

The average electric field across the detector area is

$$\overline{E(L,d)} = \frac{1}{Ld}\int_{-\frac{L}{2}}^{\frac{L}{2}}\int_{-\frac{d}{2}}^{\frac{d}{2}} E(x,y)dxdy = \frac{E\pi {w_1}^2}{Ld} Erf(\frac{L}{2w_1})Erf(\frac{d}{2w_1}) \tag{2.10}$$

where *Erf* is the error function, and $L= L_M + L_S$. The peak strength of the electric field, $E_0$, can be expressed in terms of the total power in the THz beam:

$$P_{THz} = \frac{1}{2}c\varepsilon_o \int_{-\infty}^{\infty}\int_{-\infty}^{\infty} E^2(x,y)dxdy = \frac{1}{2}\pi {w_1}^2 c\varepsilon_o {E_o}^2 \tag{2.11}$$

$$\Rightarrow Eo = \frac{2}{w_1}\sqrt{\frac{P_{THz}}{\pi c\varepsilon_o}} \tag{2.12}$$

By inserting Eq. (2.14) into the expression for the detector current, Eq. (2.11), we get

$$I(v) = \xi \cdot P_{laser}\sqrt{\frac{cP_{THz}}{\pi\varepsilon_o}} \frac{2R_L t}{{L_S}^2 dw_o(n-1)}\frac{1}{v} Erf[\frac{L}{2}\frac{(n-1)\pi w_o}{cR_L}v]Erf[\frac{d}{2}\frac{(n-1)\pi w_o}{cR_L}v] \tag{2.13}$$

when focusing spot size $\lim_{\lambda \to o} w_1(d_{focus}) = \frac{c}{\pi v w_o}\frac{R_L}{(n-1)}$.

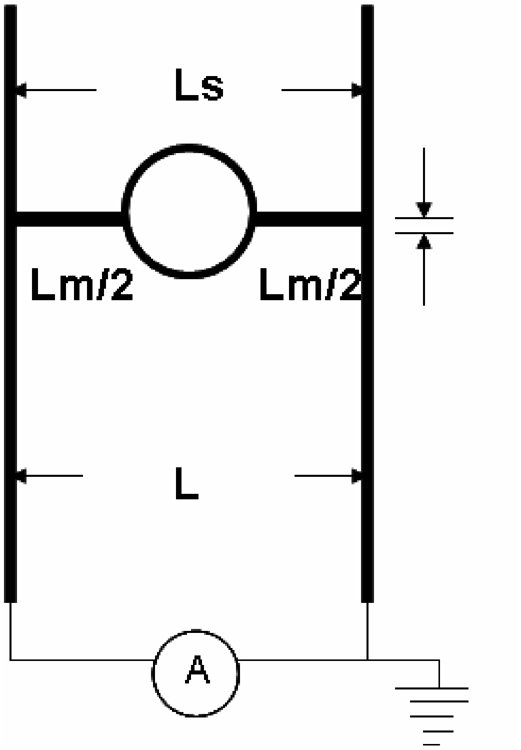

Fig. 2.1 Structure of antenna detector

### 2.1.3 Applications

Terahertz spectroscopy affords easy access to both the real and imaginary parts, providing a wealth of additional information.

In addition, many previous measurements have been based on single-frequency or narrow-band measurements, contradictorily; THz-TDS is inherently a broadband technique.

THz technologies have made great progress for aiming at applications such as radio astronomy, remote-sensing, spectroscopy [16-18], optical properties of semiconductors and dielectrics [19], imaging of general substances [20-22], and biomedical imaging [23-24]. It also can be applied to find specific spectroscopic fingerprints of biological matter in this region [25]. Since the features of THz imply in various areas of science, it is clearly THz age will come soon.

## 2.2 Basics of Liquid Crystal

Liquid crystal (LC) materials [8-10, 26-27] generally have several characteristics; the most important one is the birefringence, due to their nature, that is, they have two indices of refraction or so-called “double refraction”. By utilizing this, people can do lots of applications.

### 2.2.1 The Liquid Crystal Phase

General solid changes to transparent liquid because of rising temperature to its melting point, but, certain matters have special characteristics; they do not transfer phase from solid state to liquid state but by way of so called ‘liquid crystal’ compound state, transfer to the usual liquid.

Molecules in a solid are constrained to occupy only certain positions. We describe this condition by saying that the solid phase possesses positional order. Moreover, the molecules in the ways they orient themselves with respect to one another. We say the solid phase also possesses orientational order. When a solid melts to a liquid, both types of order are lost completely, the molecules move and tumble randomly. When a solid melts to a liquid crystal, however, the positional order may be lost although some of the orientational order remains. The molecules in the liquid crystal phase are free to move about in much the same fashion as in a liquid, but as they do so they tend to remain oriented in a certain direction. This orientational order is not nearly as perfect as in a solid; in fact, the molecules of a liquid crystal spend only a little more time pointing along the direction of orientation than along some other direction. Still this partial alignment does represent a degree of order not present in liquids and thus requires that we call this condition a new phase or state of matter, Fig. 2.2 illustates the order present in the solid, liquid crystal, and liquid phases [26].

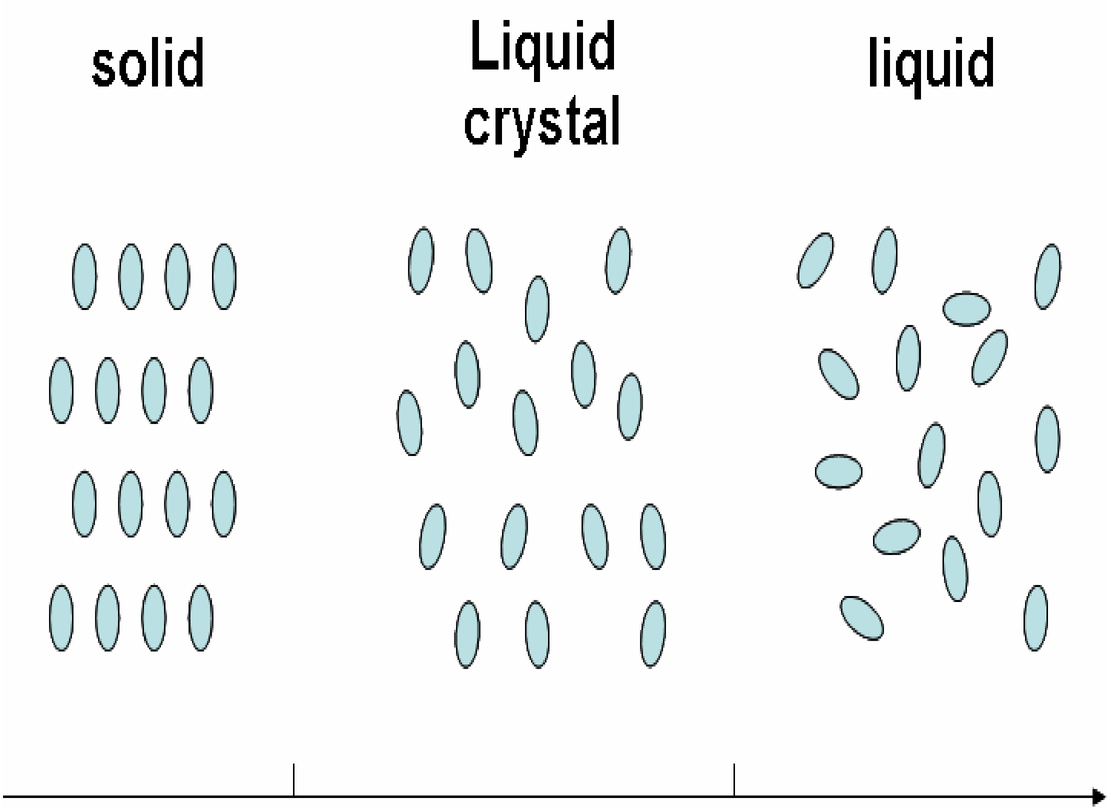

Fig. 2.2 Schematic illustration of the solid, liquid crystal, and liquid phases.

### 2.2.2 Nematic Liquid Crystal

At present, there are extremely many kinds of liquid crystal which uses broadly, according to the conformation, liquid crystal can be divide into nematic LC, smectic LC, and cholesteric LC etc.

Nematic came by Greek, means “silk”, the nematic liquid crystal shown in fig. 2.3 is a transparent or translucent liquid, its molecules are parallel arrangement and rotate as a rod that causes the polarization of light waves to change as the waves pass through the liquid, but actually is not like the smectic liquid crystal, which has the straticulate structure, nematic liquid crystal has birefringence in optics. Compares to smectic liquid crystal, nematic liquid crystal has smaller viscosity coefficient and smaller fluidity, the fluidity is caused by the easier free motion in the long-axis direction of the NLC molecule. The nematic phase is characterized by molecules that have no positional order but to point in the same direction.

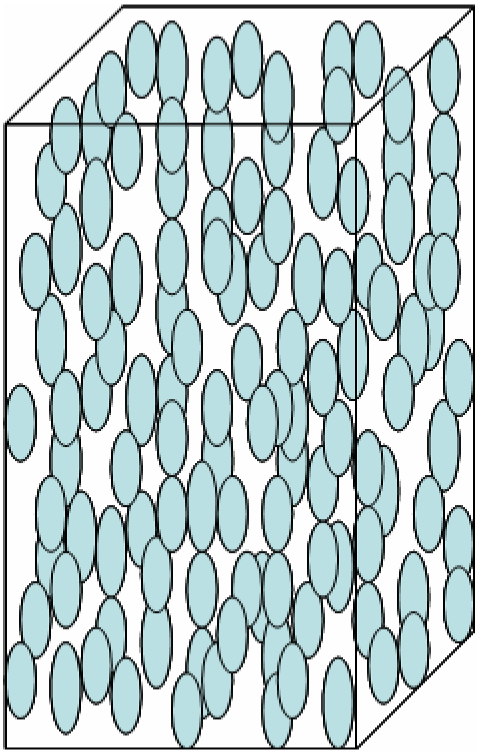

Fig. 2.3 Nematic liquid crystals

### 2.2.3 Birefringence

Birefringence, or double refraction, is the division of a ray of light into two rays (the ordinary ray and the extraordinary ray) when it passes through certain types of material, such as liquid crystals, depending on the polarization of the light. This is explained by assigning two different refractive indices to the material for different polarizations. The birefringence is quantified by

$$\Delta n = n_e - n_o \qquad (2.14)$$

where $n_o$ is the refractive index for the ordinary ray, that means the electrical field of the incident light perpendicular to the n-k plane, and similarly, $n_e$ is the refractive index for the extraordinary ray, that means the electrical field of the incident light not perpendicular to the n-k plane. When the incident direction of light is not parallel to the optical axis of the liquid crystal molecules, the extraordinary ray should be written as following:

$$n_{eff} = \left(\frac{\sin^2\theta}{n_{//}2} + \frac{\cos^2\theta}{n_{\perp}2}\right)^{-1/2} \qquad (2.15)$$

$\theta$ is the angle between the direction of the incident light and the optical axis.

Therefore, the birefringence should be changed to:

$$\Delta n = n_{eff} - n_o \qquad (2.16)$$

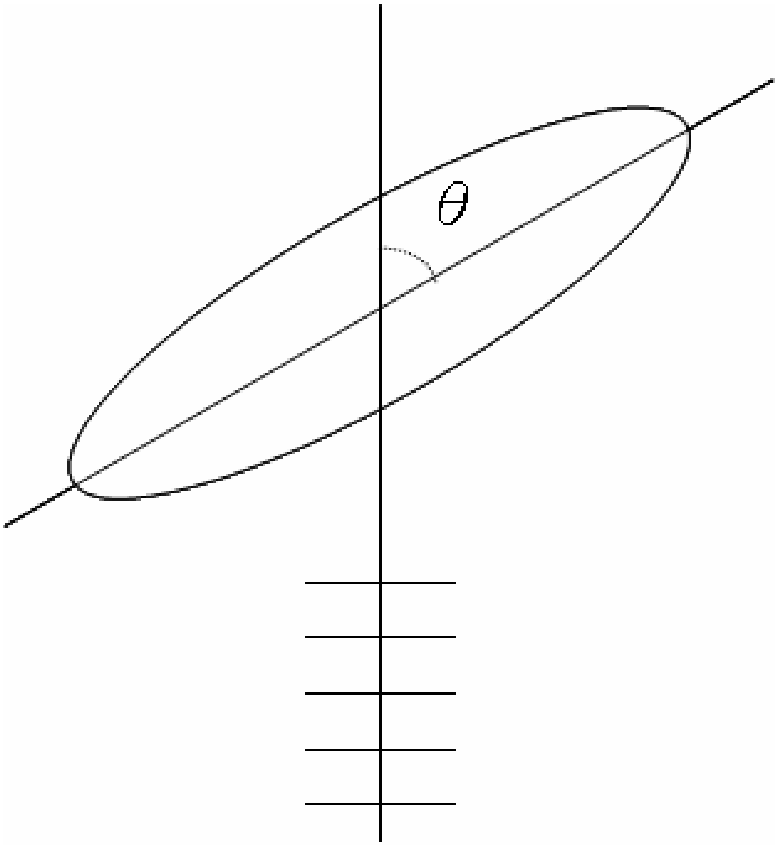

Fig. 2.4 $n_{eff}$ is function of θ

### 2.2.4 External Influences on Liquid Crystals

Scientists and engineers are able to use liquid crystals in a variety of applications, because external perturbation can cause significant changes in the macroscopic properties of the liquid crystal system. Both electric and magnetic fields can be used to induce these changes. The magnitudes of the fields as well as the speed at which the molecules align are important characteristics industry deals with. Finally, special surface treatments can be used in liquid crystal devices to force specific orientations of the director.

### 2.2.4.1 Electric and Magnetic Field Effects

The response of liquid crystal molecules to an electric field is the major characteristic utilized in industrial applications [28-29]. The ability of the director to align along an external field is caused by the electric nature of the molecules. One end of a molecule has a net positive charge while the other end has a net negative charge results the permanent electric dipoles. When an external electric field is applied to the liquid crystal, the dipole molecules tend to orient themselves along the direction of the field. In Fig.2.5, the black arrows represent the electric field vector and the red arrows show the electric force on the molecule.

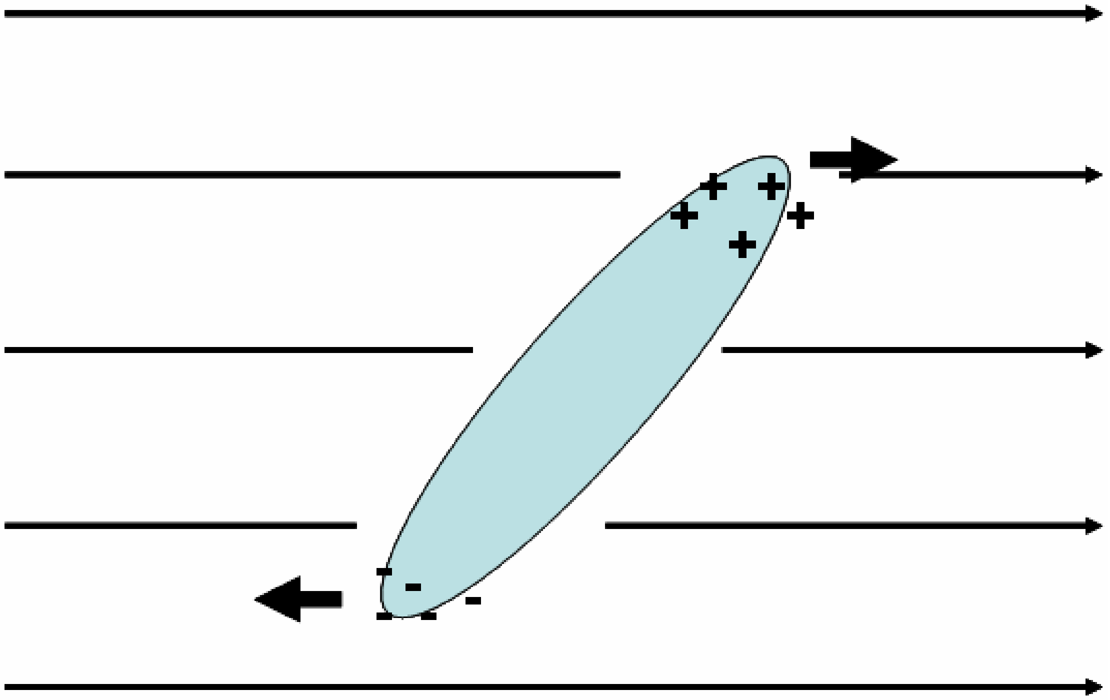

Fig. 2.5 Accumulation of positive and negative charge result the permanent electric dipoles

Even if a molecule does not form a permanent dipole, it can still be influenced by an electric field. In some cases, the field produces slight re-arrangement of electrons and protons in molecules such that an induced electric dipole results. While not as strong as permanent dipoles, orientation with the external field still occurs.

The effects of magnetic fields on liquid crystal molecules are analogous to electric fields. Because magnetic fields are generated by moving electric charges, permanent magnetic dipoles are produced by electrons moving about atoms. When a magnetic field is applied, the molecules will tend to align with or against the field.

### 2.2.4.2 Surface Preparations

The liquid crystal molecular arrangement can be divided into many kinds, below we list some commonly used ways and give the simple explanation to the liquid crystal arrangement [10].

(1) Homoetropic arrangement: all LC molecules are vertical aligned to both substrates.

(2) Homogeneous arrangement: all LC molecules are parallel aligned to both substrates and face the same direction.

(3) Tilted arrangement: all LC molecules are inclined aligned with a certain angle to both substrates and face the same direction.

(4) Hybrid arrangement: LC molecules are vertical aligned to one side of substrate, and parallel aligned to the other side of substrate; therefore, LC molecules are continuously inclined between both substrates.

(5) Twisted arrangement: all LC molecules are parallel aligned to both substrates, but the direction of each substrates Mutually has 90 included angles.

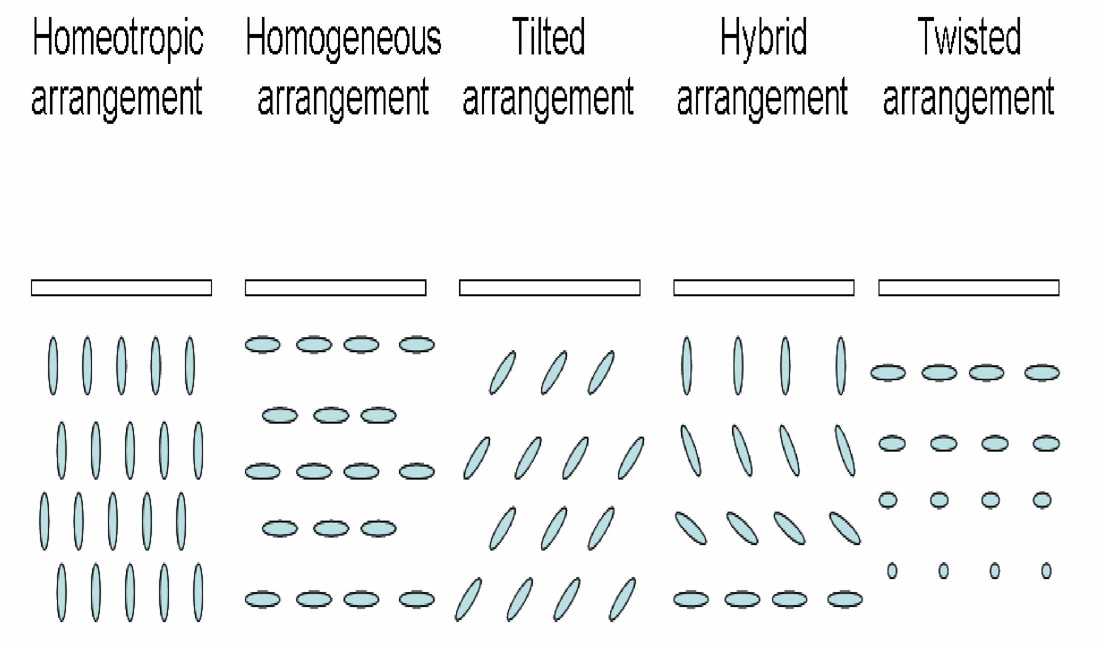

Fig. 2.6 Mechanism of various alignments

In the absence of an external field, the director of a liquid crystal is free to point in any direction. It is possible, however, to force the director to point in a specific direction by introducing an outside agent to the system. For example, when a thin polymer coating (usually a polyimide) is spread on a glass substrate and rubbed in a single direction with a cloth, it is observed that liquid crystal molecules in contact with that surface align with the rubbing direction. The currently accepted mechanism for this is believed to be an epitaxial growth of the liquid crystal layers on the partially aligned polymer chains in the near surface layers of the polyimide.

### 2.2.4.3 Freedericksz Transition

The competition between orientation produced by surface anchoring and by electric field effects is often exploited in liquid crystal devices. Consider the case in which liquid crystal molecules are aligned parallel to the surface and an electric field is applied perpendicular to the cell as in Fig.2.7. At first, as the electric field increases in magnitude, no change in alignment occurs. However at a threshold magnitude of electric field, deformation occurs, where the director changes its orientation from one molecule to the next. The occurrence of such a change from an aligned to a deformed state is called a Freedericksz transition and can also be produced by the application of a magnetic field of sufficient strength.

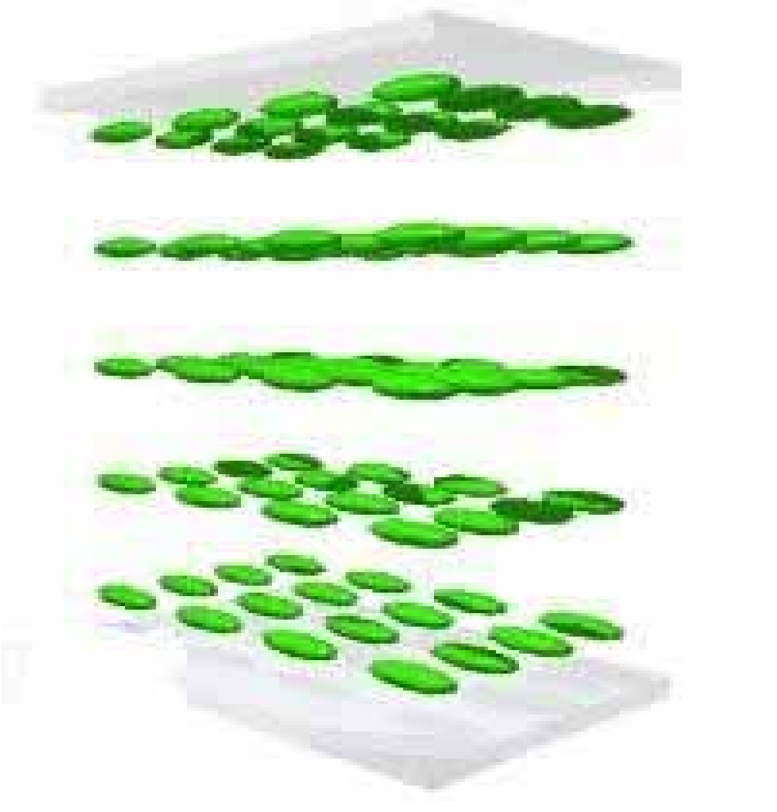

Fig. 2.7 Liquid crystal molecules are aligned parallel to the surface and an electric field is applied perpendicular to the cell

The Freedericksz transition [8] is fundamental to the operation of many liquid crystal displays because the director orientation (and thus the properties) can be controlled easily by the application of a field. Refer to the Applications section for more information about liquid crystals used in displays

### 2.2.3 Threshold Voltage

Threshold voltage ($V_{th}$) in this experiment is the voltage at which liquid crystal molecules begins to rotate. In the case 3 of the Freederiksz transition model, $V_{th}$ can be derived by following calculation:

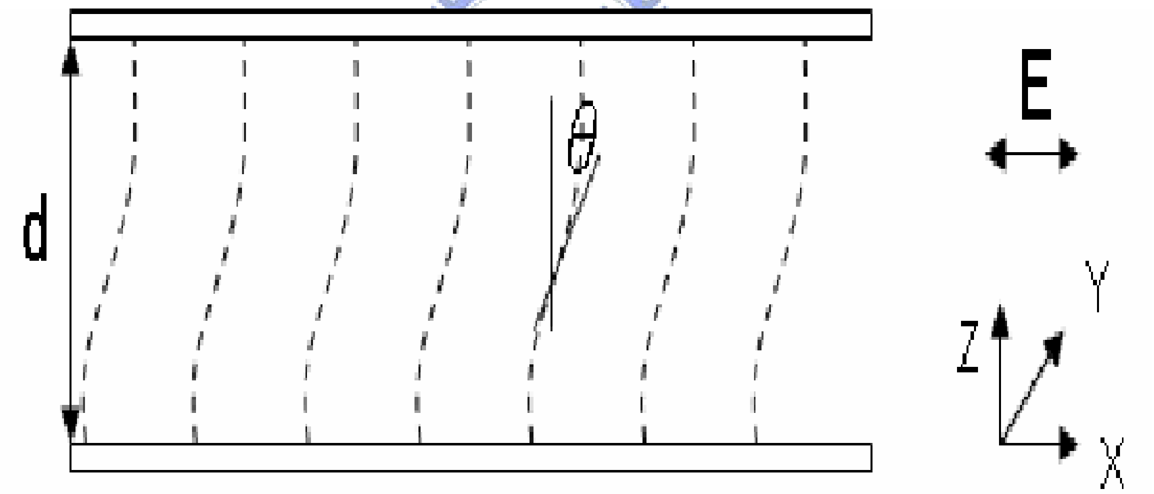

Fig. 2.8 Case 3 of the frederiks transition

Assume the angle between z axis and the direction of liquid crystal can be expressed as a function of z

$$\theta = \theta(Z) = \theta_m \cdot \sin(\frac{\pi}{d} Z) \tag{2.17}$$

Where $\theta_m$ is the maximum rotate angle affected by electrical field.

The distortion free energy density per unit volume of NLC cell can be written as

$$f_d = \frac{1}{2}K_1(\nabla \cdot n)^2 + \frac{1}{2}K_2(n \cdot \nabla \times n)^2 + \frac{1}{2}K_3(n \times \nabla \times n)^2 \tag{2.18}$$

In case 3, $n_z = n\cos\theta$, $n_x = \sin\theta$, $ny = 0$, $f_d$ is reduced to the forms

$$f_d = \frac{1}{2}K_1 \sin^2\theta(\frac{d\theta}{dZ}) + \frac{1}{2}K_3 \cos^2\theta(\frac{d\theta}{dZ}) \tag{2.19}$$

$K_1$, $K_2$, and $K_3$ are the splay, twist, and bend elastic constant, respectively. After integral, the distortion free energy density per unit area is obtained

$$F_d = \int_0^d f_d dz = \frac{1}{4}K_3 \frac{\pi^2}{d}\theta_m{}^2 + \frac{1}{16}(K_1 - K_3)\frac{\pi^2}{d}\theta_m{}^4 \tag{2.20}$$

Electrical field also effects in an insulating nematics

$$\vec{D} = \varepsilon_V \vec{E} + (\varepsilon_P - \varepsilon_V)(\hat{n} \cdot \vec{E})\hat{n} \tag{2.21}$$

Where $\varepsilon_v$ and $\varepsilon_p$ are the vertical and parallel dielectric constant, respectively.

The energy density per unit volume produced from electrical field is

$$f_e = -\frac{1}{4}\int D \cdot dE = -\frac{\varepsilon_V}{8\pi}E^2 - \frac{\varepsilon_a}{8\pi}(\hat{n} \cdot \vec{E})^2 \tag{2.22}$$

Where $\varepsilon_a = \varepsilon_p - \varepsilon_v$

The electrical energy density per unit area is

$$F_e = -\frac{\varepsilon_a E^2}{8\pi}\int \sin^2\theta dz \approx -\frac{\varepsilon_a E^2}{8\pi}\theta_m{}^2 \frac{d}{2} \tag{2.24}$$

The total free energy is

$$F = F_d + F_e = \theta_m{}^2(\frac{1}{4}K_3\frac{\pi^2}{d} - \frac{1}{16\pi}\varepsilon_a E^2 d) + \theta_m{}^4(....) \tag{2.25}$$

At *Ec*, the coefficient of $\theta_m{}^2$ is zero

$$\frac{K_3\pi^2}{d} = \frac{\varepsilon_a E^2}{4\pi} d \qquad (2.26)$$

Then, Vc in cgs units is as follow:

$$V_c = 2\pi^{\frac{3}{2}}\sqrt{\frac{K_3}{\varepsilon_o\varepsilon_a}} \qquad (2.27)$$

Vc in MKS units is rewritten as

$$V_c = \pi\sqrt{\frac{K_3}{\varepsilon_o\varepsilon_a}} \qquad (2.28)$$

### 2.2.6 Application of Liquid Crystal

The arrangement of LC molecules is not as solidity as crystal, it is soft and easy to distort by the external force, therefore, it can be affected by electric field, magnetic field, heat, light, stress, attracts of heterogeneous matter and so on, the molecules would be rearranged, the distortion, or characteristics would change, therefore LC may apply to the LC display, LC optics component [10], etc.

## 2.3 Phase Shifters

The phase shifter, as a general-purpose component, finds use in a variety of communication and radar systems, microwave instrumentation and measurements systems; many kinds of phase shifter will be introduced below.

### 2.3.1 Phase Retardation

Suppose that the E-field of an incident monochromatic plane wave has components parallel and perpendicular to the optic axis, two separate plane waves will propagate through the crystal. Since $v_{//} > v_{\perp}$, $n_o > n_e$, and the e-wave will move across the specimen more rapidly than the o-wave. After traversing a superposition of the e- and o-waves, which now have a relative phase difference of ΔΦ. Keep in mind that these are harmonic waves of the same frequency whose E-fields are orthogonal. The relative optical path length difference is given by

$$\Lambda = d(n_e - n_o) \tag{2.29}$$

and since $\Delta\varphi = k\Lambda$, the phase difference, in radians, is

$$\Delta\varphi = \frac{2\pi}{\lambda} d(n_e - n_o) \tag{2.30}$$

THz wave produce different time delay when it pass through different media, i.e. different refract index. As we show in fig. 2.9, when THz pass through the free space (the refract index of free space is ~1), the time delay would larger than pass through the other media, we take it for reference. Then we radiate another THz wave through a liquid crystal sample with positive refract index ($n_e > n_o$), the THz wave can be separated to two parts, one is Ordinary-wave and another one is extraordinary-wave, the two parts "see" different refract index when passing through the LC sample, and cause different time delay, we call them △$t_o$ and △$t_e$ , by substituting eq. (2.29) and eq. (2.30), we can easily obtain the phase difference.

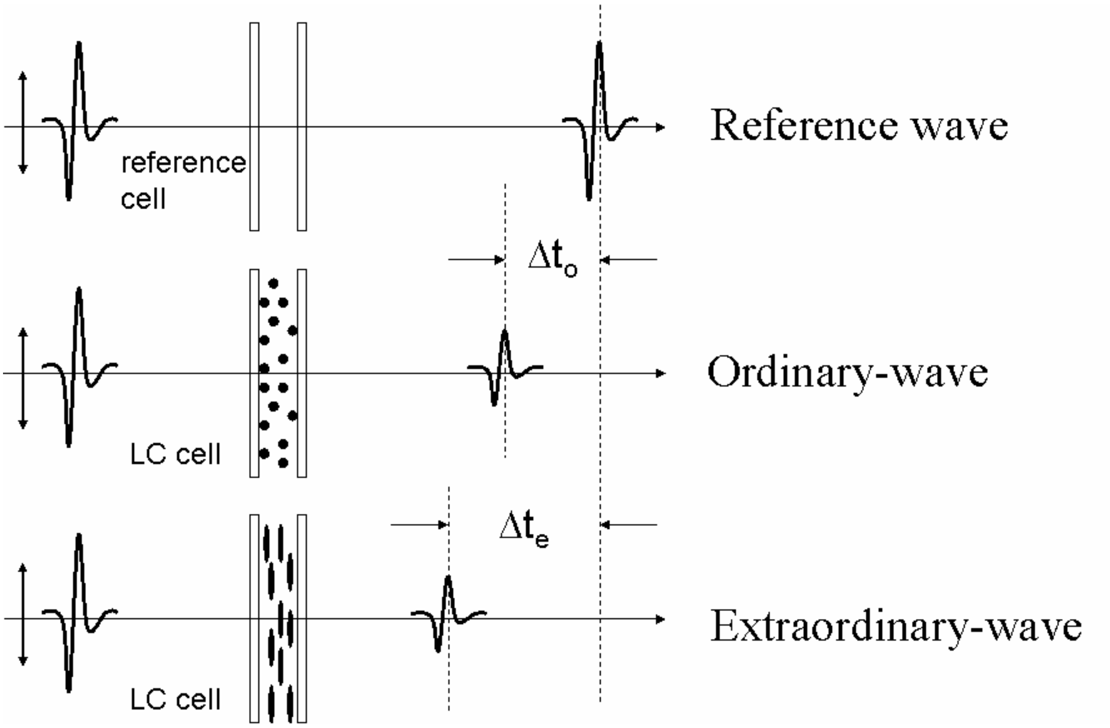

Fig. 2.9 Difference time delay produced by the THz wave transmitting through different refractive index

2.3.2 Micro Wave and Millimeter Wave Phase Shifters [30]

Phase shifters can be broadly classified as mechanical or electronic, depending on whether the phase control is achieved through mechanical or electronics tuning, these phase shifters may be classified as ferrite, semiconductor device, active FET, or bulk semiconductor phase shifters etc. in the following sections, we briefly describe some common phase shifter used in micro wave and millimeter wave.

### 2.3.2.1 Mechanical Phase Shifters

Mechanical phase shifters are generally constructed in coaxial line or metallic waveguides. The phase of the device is varied by means of mechanical tuning, such as a variation in the physical length of the line or rotation-displacement of a dielectric slab inside a waveguide. As compared with the electronic phase shifters, mechanical phase shifters are rugged, simple to fabricate, and have very low loss.

### 2.3.2.2 Ferrite Phase Shifters

The basis of operation of all ferrite devices is the interaction between the electromagnetic waves and the spinning electrons in a magnetized ferrite. In a magnetized ferrite, the magnetic dipole moment of the spinning electron processes about the applied field, and its precession frequency is directly proportional to the magnitude of this dc magnetic field. Ferrite phase shifters have been realized mostly in waveguide geometry. Other geometries, such as the coaxial line, strip line, and micro-strip line, have been employed as well but to a much lesser extent. These phase shifters can be designed to operate either in analog or digital mode.

### 2.3.2.3 Semiconductor Device Phase Shifters

The semiconductor phase shifters considered here are those that use semiconductor junction devices as electronic control elements. Examples of devices that can act as electronic switches are the p-i-n diode, GaAs

FET, and the Schottky diodes.

### 2.3.2.4 Active FET Phase Shifters

Phase shifters that amplify the RF signal in addition to the phase shift are knows "active" phase shifters. The GaAs metal semiconductor (MESFET) in particular, the dual-gate MESFET, is the key control element that enables this dual function. Both analog and digital phase shifters have been realized.

### 2.3.2.5 Bulk Semiconductor Phase Shifters

The use of bulk semiconductor elements is reported to be an attractive practical alternative to the use of semiconductor junction devices in realizing phase shifters at millimeter-wave frequencies. In addition to circumventing the problem of having to fabricate minute concentrated junctions, the bulk element offers an extended medium for millimeter-wave interaction, particularly in terms of higher bandwidth and power handling.

### 2.3.2.6 Traveling-Wave Phase Shifters

The traveling-wave tube (TWT) is an excellent example of a traveling-wave phase shifter. The operation of TWT is based on the interaction between an electron beam and waves on a traveling-wave structure. The TWT phase shifter has certain practical limitations: a high noise figure and interdependent phase and gain. Furthermore, the phase shifters are bulky and heavy. Because of these limitations and the subsequent development of other attractive phase shifters such as the ferrite and semiconductor types, the use of the TWT device as a phase shifter has receded.

### 2.3.3 THz Phase Shifters

Beforetime, Libon et al. [31] used a mixed type-I/type-II GaAs/AlAs multiple-quantum-well sample to demonstrate an optically controllable and tunable terahertz filter. Long-lived electron–hole pairs in the quantum wells, which allow for efficient THz attenuation over a large THz spot size for extremely low optical cw power. Because the shifting of the THz wave forms can be optically controlled via the carrier density and hence the complex refractive index, this quantum well structure can therefore also be used as a THz phase shifter. The optically induced change of the GaAs quantum wells from a dielectric to a conducting material leads to the observed attenuation and the shifting of the THz wave forms. A good phase shifter can tunes the phase from 0 to 2π, in THz region, the characteristics of liquid crystal are applied in phase shifter. Magnetically and electrically controlled liquid crystal phase shifters are introduced as follow.

#### 2.3.3.1 Magnetically Tunable THz Phase Shifter

Magnetically tunable THz phase shifter [32] was publicized by our group; fig 2.10 demonstrates the LC THz Phase shifter, which consists of a rotary magnet homeotropically and a aligned LC cell. The rotation axis is perpendicular to both of the polarization direction and the propagation direction of the THz wave. θ is the magnetic inclination angle, which is defined as the angle between the magnetic field and the propagation direction. The effective refractive index of LC changes with the LC molecular orientation controlled by the angle θ. The phase shift, δ(θ), due to magnetically controlled birefringence is given by

$$\delta(\theta) = \int_{0}^{L} \frac{2\pi f}{c} \Delta n_{eff}(\theta, z) dz \tag{2.31}$$

where L is the thickness of LC layer, .$n_{eff}$ is the change of effective birefringence, f is the frequency of the THz waves and c is the speed of light in vacuum.

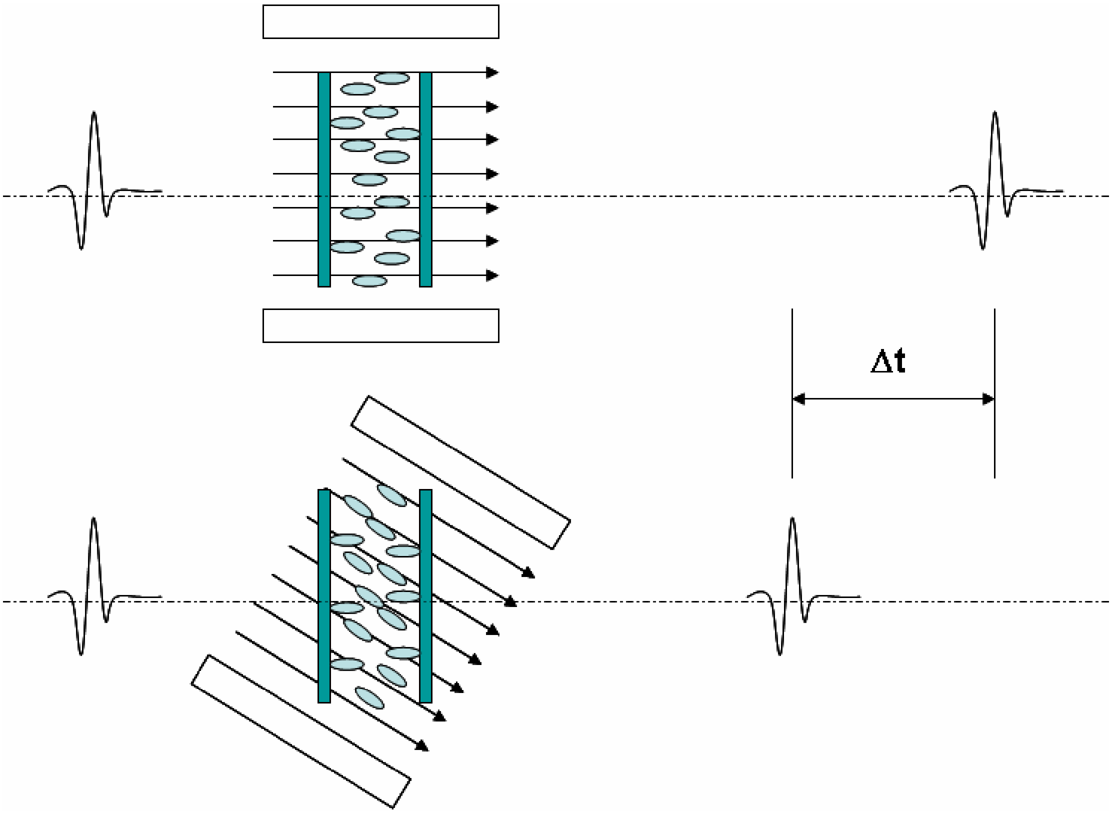

Fig. 2.10 Relative position of the magnet and the liquid crystal cell

Fig 2.11 shows the relative position of the magnet and the liquid crystal cell, when we rotate the magnet, the liquid crystal would be aligned along the direction of the magnetic field, such that the effective refraction coefficient is changed, which causes phase retardation.

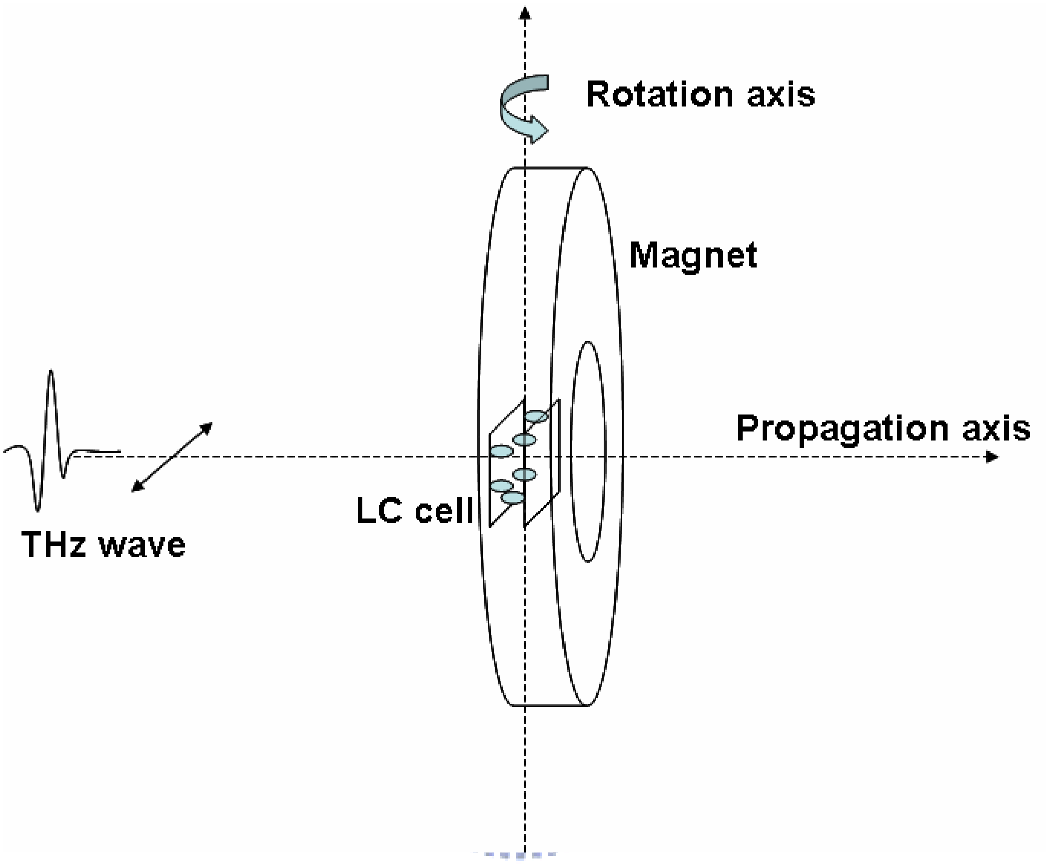

Fig 2.11 Schematic diagram of a magnetically controlled THz phase shifter

Because the magnetic field is large enough such that the LC molecules are reoriented parallel to the magnetic field, the phase shift, $\delta(\theta)$ can then be re-written as

$$\delta(\theta) = 2\pi L \frac{f}{c} \{ [ \frac{\cos^2(\theta)}{n_o^2} + \frac{\sin^2(\theta)}{n_e^2} ] - n_o \} \tag{2.32}$$

where $n_o$ and $n_e$ are the ordinary and extra-ordinary refractive indices of the LC. The theoretical phase shift can be calculated if we know the $n_o$ and $n_e$ of LC and the thickness of the LC layer.

### 2.3.3.2 Voltage Dependent Birefringence

#### 2.3.3.2.1 Electrically Controlled 4.07° Terahertz Phase Shifter [33]

Fig. 2.12 schematically shows the configuration of a variable phase shifter with a nematic LC cell for phase shifting of THz signals propagating in free space. The cell was produced by sandwiching the commercial available LC, 5CB (Merck) between two fused silica windows as substrates. The thickness of the cell was $36.5 \pm 1.5 \mu m$, and the substrates were deposited the gold strips in 3mm width (one on each substrate) cross at an angle of ~30°, onto the inner surfaces of the substrates of the cell as electrodes. At the probing position, the strips were separated by about 3 mm. The cell was homogeneously aligned such that the director or optical-axis of the LC was parallel to one of the gold strips. An ac voltage at 1 kHz was applied to the electrodes. Consider a linearly polarized THz beam passing through the cell with LC having positive dielectric anisotropy. Without or with small bias field (root mean square value) which is smaller than a threshold value, LC molecules would not or only slightly be affected, the transmitted THz beam will remain linearly polarized if the polarization of the incident THz beam is parallel or perpendicular to the LC director. Once the bias field is larger than a threshold value, this bias field will reorient the direction of LC toward the bias field direction; this phenomenon is so called Fréedericksz transition. As a result, the effective refractive index of the LC layer will change. The phase shift due to the electrically controlled birefringence is given by

$$\delta = \frac{2\pi L f \Delta n_{eff}}{c} \qquad (2.33)$$

where L is the LC layer thickness, is the frequency of THz wave, $\Delta n_{eff}$ is the average effective birefringence and is the speed of light in vacuum.

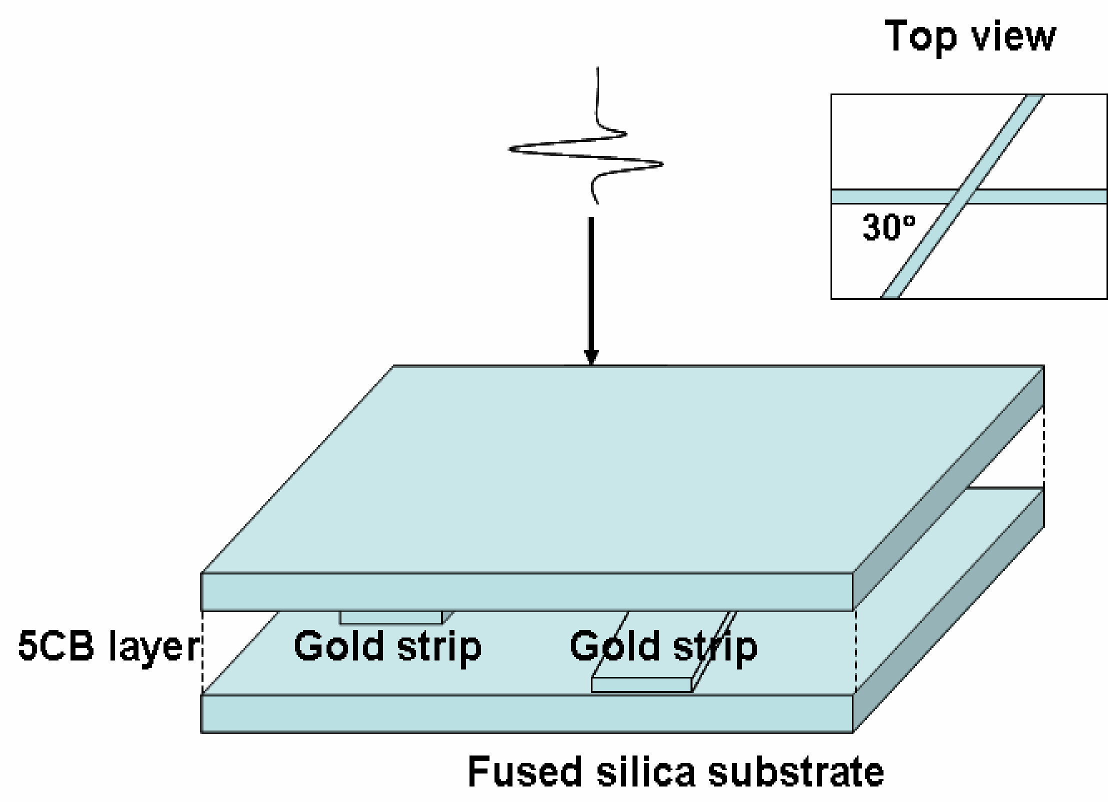

Fig. 2.12 Schematic diagram of a THz phase shifter using a LC 5CB cell. The inset shows the top view of 5CB cell.

### 2.3.3.2.2 Electrically Controlled π/2 Terahertz Phase Shifter

The structure of electrically controlled cell using a NLC E7 cell is shown in Fig 2.13.

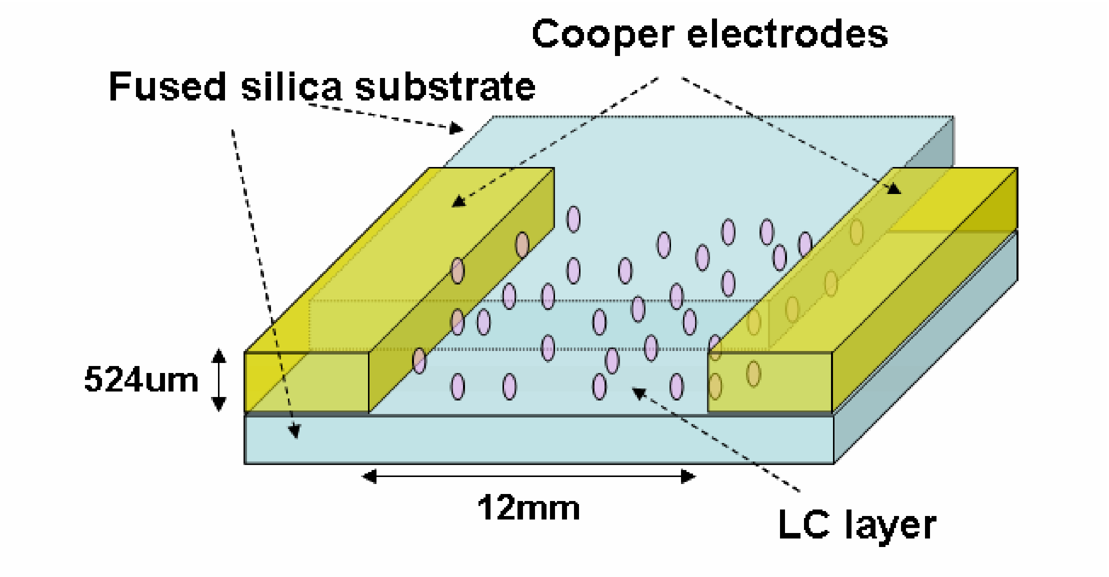

Fig 2.13 Schematic diagram of an electrically controlled THz phase shifter

The sample was fabricated with the liquid crystal layer between two fused silica substrates. The two copper pieces (purity 99.94%) were sandwiched between two substrates as spacers and electrodes. The electrodes were parallel to each other. The substrates were coated by dimethyloctadecyl-(3-trimethoxysilyl)-propylammonium- chloride (DMOAP) so that the orientation of the liquid crystal was perpendicular to the substrates (so-called homeotropic alignment [34]). In our experiment, the linearly polarized THz beam passed through the E7 layer which has positive dielectric anisotropy. Without any bias, the effective refractive index of LC is $n_o$. Once the bias increases beyond the threshold voltage ($v_{th}$), the director of the LC will be induced to reorient toward the direction of the electric field. The above phenomenon is called the Frederiks transition. Subsequently, the effective refractive index of the LC will be changed. The phase shift due to the electrically controlled birefringence is given by

$$\delta = {}^{2\pi d f \Delta n_{eff}(v)}\!\!\diagup_{c} \tag{2.34}$$

where d is the thickness of the LC layer, f is the frequency of THz wave, $\Delta n_{eff}(v)$ is the average effective birefringence varied with applied voltages and c is the speed of light in vacuum.

It should be attend that the difference from magnetically and electrically controlled phase shifter. For the magnetically controlled one, the permanent magnet provides the enough magnetism so that the orientation of the LCs in the NLC cell is induced to the direction of the magnetic field. In the electrically controlled case, the voltage is gradually applied from 0 volt, under the threshold voltage, liquid crystal molecules are not affected to rotate by electrical field. If the applied voltage is higher than the threshold voltage, liquid crystal molecules rotate different angle as they are in different part of the cell. It is mainly decided by the distance from the molecules and the fused silica substrates, the short one is affected by stronger effort of the substrate. The longer one is weaker affected by substrate but largely by the electrical field. Until the voltage is high enough that most molecules in the NLC cell rotate parallel to the electrical field, the shift angle is finally saturate. Therefore, theoretical curve should be separated in several parts according to the applied voltage.

The alternating current (AC) voltage (square wave) was applied to the electrodes from 0 to 125V (rms) at 1 kHz. The analyses of case 3 in the Frederiks transition to the electric case was derived, and the differences between the splay elastic constant and the bend one of LC were so close to be negligible. We can obtain the subsequent results. The birefringence is not changed and the molecules are not reoriented for applied voltages $v<v_{th}$, where

$$v_{th}=\pi\frac{L}{d}\left(\frac{k_3}{\varepsilon_a\varepsilon_o}\right)^{\frac{1}{2}} \tag{2.35}$$

and $k_3$ and $\varepsilon_a$ are the bend elastic constant and anisotropic dielectric constant of E7 respectively. L is the separate distance of two electrodes.

Before deriving the phase shift angle, correct $\Delta n_{eff}(v)$ value should be calculated at first. There are two factors affect the orientation of the LCs, distortion and electrical field. By finding the lowest value of the total energy which is the sum of distortion and electrical energy, $\theta$ (v,z) will be known.

Form eq. 2.23 and 2.26, total energy per unit volume is expressed as

$$f=f_d+f_e=\frac{1}{2}K_1\sin^2\theta(\frac{d\theta}{dZ})+\frac{1}{2}K_3\cos^2\theta(\frac{d\theta}{dZ})+\frac{\varepsilon_v}{2}E^2+\frac{\varepsilon_a}{2}(\hat{n}\cdot\vec{E})^2 \tag{2.36}$$

At equilibrium

$$\frac{d}{dz}[(k_1\sin^2\theta+k_3\cos^2\theta(\frac{d\theta}{dz})^2)+\varepsilon_a\sin^2\theta]=0 \tag{2.37}$$

$\frac{d\phi}{dz}=0$ ,$\phi_m$ the maximum value in the center

$$\varepsilon_o\varepsilon_a E^2\sin^2\phi_m=(K_1\sin^2\phi+k_3\cos^2\phi)(\frac{d\phi}{dz})^2+\varepsilon_o\varepsilon_a E^2\sin\phi \tag{2.38}$$

$$\int_0^{\frac{d}{2}}(\varepsilon_o\varepsilon_a)^{1/2}\,Edx=\int_0^{\phi_m}(\frac{k_1\sin^2\phi+k_3\cos^2\phi}{\sin^2\phi_m})d\phi \tag{2.39}$$

$\phi_m$=0 for threshold electric field vector

$$\frac{d}{2}\sqrt{\varepsilon_o\varepsilon_a}Ec=\frac{d}{2}\sqrt{K_3}\ ,\quad Ec=\frac{\pi}{d}\sqrt{\frac{K_3}{\varepsilon_o\varepsilon_a}} \tag{2.40}$$

To measure the optical phase difference P between light polarization in the x and y direction

$$P = \frac{2\pi}{\lambda}\int_{-\frac{d}{2}}^{+\frac{d}{2}}(n(x) - n_o)dx\,,\quad n(x) = \left(\frac{\cos^2\phi}{n_o^{\ 2}} + \frac{\sin^2\phi}{n_e^{\ 2}}\right)^{-\frac{1}{2}} \tag{2.41}$$

$$\phi = P(E) - P(0) = \frac{dn_o 2\pi}{\lambda}\left(-1 + \frac{2Ec}{\pi E}\int_O^{\phi_m}\left(\frac{1 + K\sin^2\phi}{(1 + v\sin^2\phi)(\sin 2\phi_m - \sin 2\phi)}\right)^{1/2} d\phi\right) \tag{2.42}$$

Where $v = \dfrac{n_o^{\ 2} - n_e^{\ 2}}{n_e^{\ 2}}$

$$x = \frac{dEc}{\pi E}\int_0^{\phi}\left(\frac{1 + k\sin^2\phi}{\sin^2\phi_m - \sin^2\phi}\right)d\phi \tag{2.43}$$

$$n(x) = n_e n_o (n_e^{\ 2}\cos^2\phi + n_o^{\ 2}\sin^2\phi)^{-1/2}\,,\quad k = \frac{k_1 - k_3}{k_3}$$

$$\phi = \frac{2\pi d n_o}{\lambda}\left(v\frac{E - Ec}{Ec}\frac{1}{K+1} - v\frac{1}{(K+1)^2}\left(3 + \frac{9}{4}v - \frac{5}{4}(v+1)\right)\left(\left(\frac{E - Ec}{Ec}\right)^2 + ....\right)\right) \tag{2.44}$$

(a)For $0<v-v_{th}<<v_{th}$, the voltage dependence of birefringence is given by

$$\Delta n_{eff}(v) = (n_e - n_o)\frac{n_o}{n_e}\left[\left(1 + \frac{n_o}{n_e}\right)\left(\frac{v - v_{th}}{v_{th}}\right)\right] \tag{2.45}$$

where $n_o$ and $n_e$ are the ordinary and extraordinary refractive indices of E7.

(b)For $v-v_{th}>>v_{th}$

$$\Delta n_{eff}(v) = (n_e - n_o)\left[1 - \frac{2}{v}\left(\frac{k_3}{\varepsilon_a\varepsilon_0}\right)^{\frac{1}{2}}\frac{L}{d}\right] \tag{2.46}$$

By utilizing the above-mentioned formulas, the experimental data can be compared with theoretical model.

### 2.3.3.2.3 In-Plain Switch THz Phase Shifter

Fig 2.14 illustrates the LC THz Phase shifter, the schematic is similar to the copper electrode THz phase shifter, consists of a homeotropically aligned fused silica substrates LC cell and NLC cell. The only one different between in-plain switch THz phase shifter and copper electrode one is conductive electrode. Copper electrode THz phase shifter take coppers as not only electrodes but also mylar; but we coated a thin gold layer on one substrate for electrode of the in-plain switch phase shifter, and controlled the cell gap by utilizing Teflon as mylar. The phase shift, $\delta(\theta)$, is given by

$$\delta(\theta) = \int_0^L \frac{2\pi f}{c} \Delta n_{eff}(\theta, z)\,dz \tag{2.47}$$

where L is the thickness of LC layer, .$n_{eff}$ is the change of effective birefringence, f is the frequency of the THz waves and c is the speed of light in vacuum.

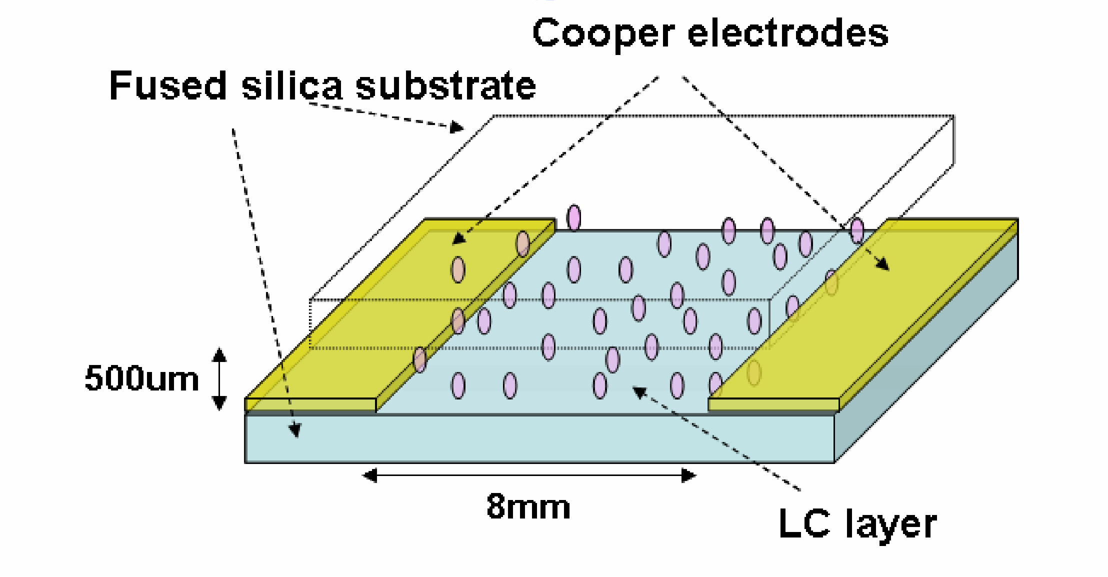

Fig 2.14 Schematic diagram of in-plain switch THz phase shifter

Compare with the copper electrode THz phase shifter, in-plain switch phase shifter has several disadvantage, (1) Gold electrode is more expensive than cooper electrode, additionally, coating a gold layer on the substrate is much difficult than aligning a copper sheet. (2) Gold electrode layer is too thin such that it is easy to be effaced. (3) $\Delta n_{eff}$ is not easy to simulate because it is the function of the rotation angle of LC, which is determined by the position in the NLC cell, and affected by more than one dimensional variety. (4) The farther distance between LC molecular and the electrode is, the smaller influence to the LC molecular, therefore, by observing fig.2.16, we can find that with the same cell thickness and LC, the phase shifter angle is smaller than the cooper electrode cell.

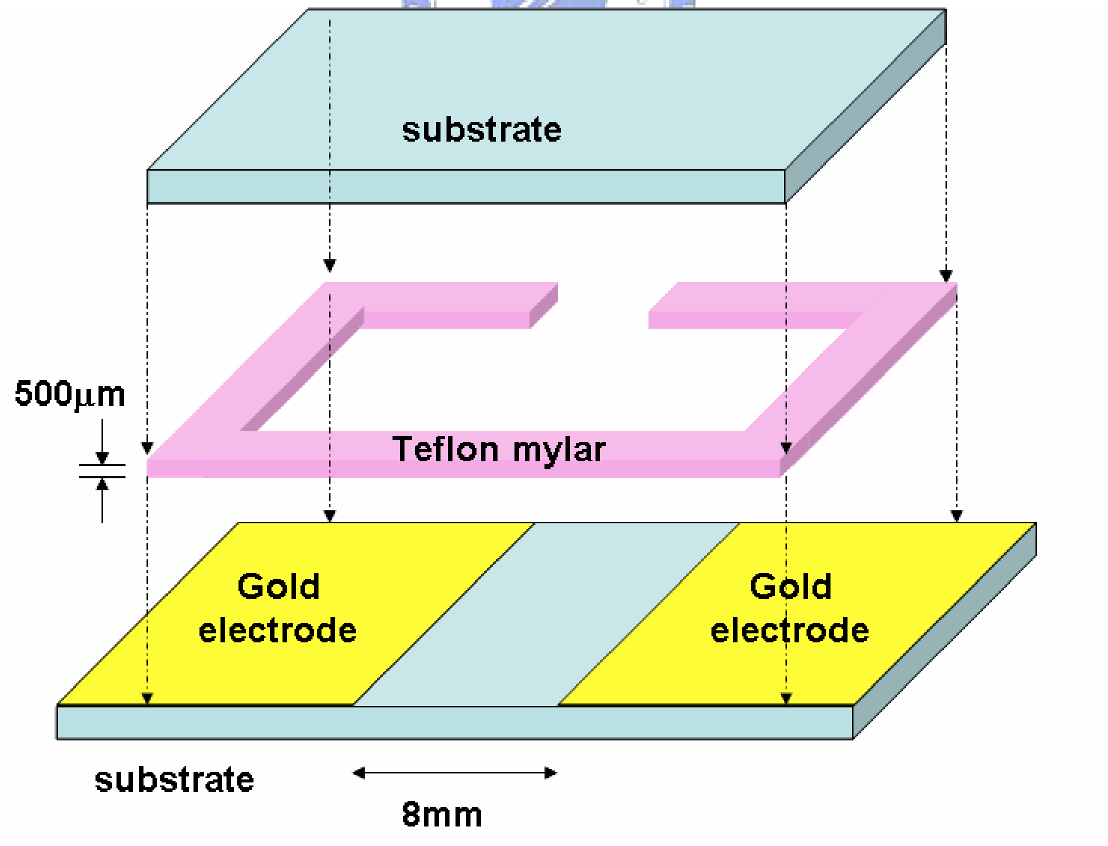

Fig. 2.15 In-plain swtich electrode pattern and sample alignment

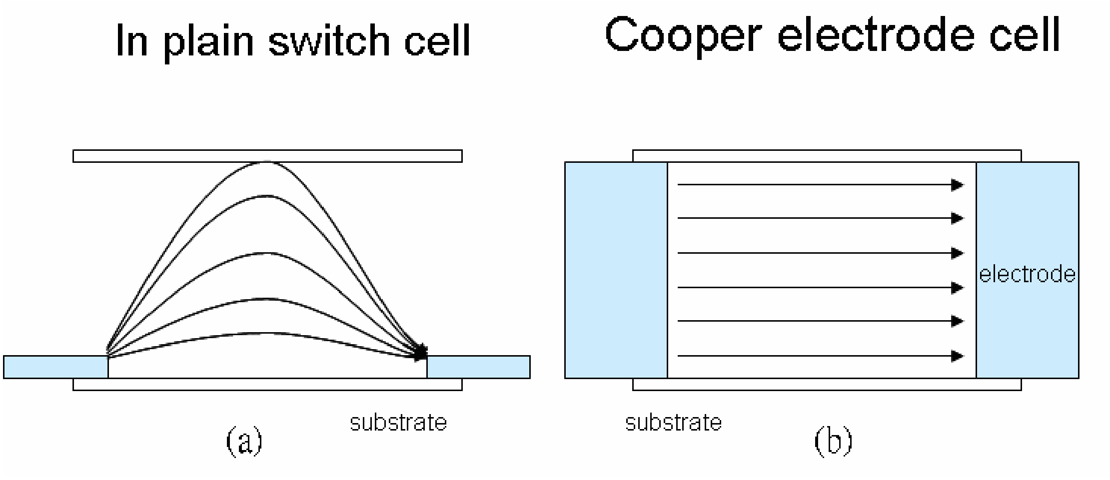

Fig 2.16 The schematic diagram of electrical field distribution (a) in-plain switch cell (b) cooper electrode cell

For these reasons, we know the cooper electrode cell is the better choice for phase shifter.

### 2.3.4 Wave Plate

To suit different applications, phase retardation plates are available. Wave plates are made from materials which exhibit birefringence. The velocities of the extraordinary and ordinary rays through the birefringent material vary inversely with their refractive indices. This difference in velocities gives rise to a phase difference when the two beams recombine. At any specific wavelength the phase difference is governed by the thickness of the retarder - waveplate.

If the angle between the electric field vector of the incident linearly polarized beam and the retarder principal plane of the quarter-waveplate is 45, the emergent beam is circularly polarized. When a quarter waveplate is double passed, i.e. by mirror reflection, it acts as a half waveplates and rotates the plane of polarization to a certain angle. Quarter waveplate are used in creating circular polarization from linear or linear polarization from circular, ellipsometry, optical pumping, suppressing unwanted reflection and optical isolation.

The transmitting and receiving antenna of our experiment are both parallel relative horn configurations, to further verify the quarter waveplate operation in this experiment; we rotated the liquid crystal sample, the transmitting antenna parallel to ground can produce the parallel polarization radiation, the receiving antenna only can receive the horizontal electric field, the field (amplitude) transmission should vary sinusoidally with the rotation angle, with a period of $\pi/2$, it can be known by following computation.

$\theta$ is defined as the angle between the long axis of the liquid crystal and the horn of the transmitting antenna.

$$E_T = \begin{bmatrix} E_x \\ E_y \end{bmatrix} = E_o \begin{bmatrix} 1 \\ 0 \end{bmatrix} \tag{2.48}$$

In order to calculate conveniently, we define the new coordinate in the liquid crystal long axis direction.

We can transfer the matrix from XY to X'Y' by transverse matrix R, in addition, we also consider the influence of reflection between different interfaces.

Where we know in our experiment, the refractive index of LC $n_e=n_{//}=1.79$, $n_o=n_{\perp}=1.62$, the refractive index of substrates and free space are $n_{glass}=1.9$ and $n_{air}=1$, respectively, the transmittance of different interfaces is $t=2n_i/(n_i+n_t)$,

$$R = \begin{bmatrix} \cos\theta & \sin\theta \\ -\sin\theta & \cos\theta \end{bmatrix} \tag{2.49}$$

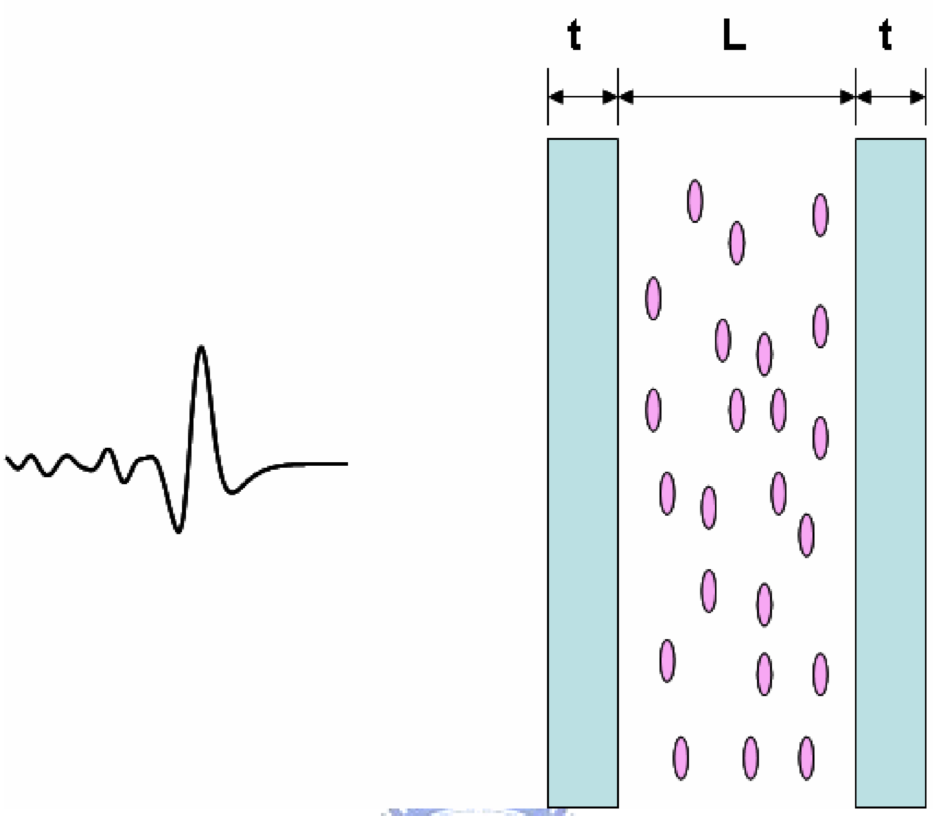

Fig. 2.17 Diagram of THz transmitting through LC cell

Then $E_T$ can be transferred to $E_{T'}$

$$E_{T'} = RE_T = E_o \begin{bmatrix} \cos\theta & \sin\theta \\ -\sin\theta & \cos\theta \end{bmatrix} \begin{bmatrix} 1 \\ 0 \end{bmatrix}$$

$$\Rightarrow E_{T'} = E_o \begin{bmatrix} \cos\theta \\ -\sin\theta \end{bmatrix}_{X'Y'} \qquad (2.50)$$

After passing through the LC sample, the electrical field is:

$$E_{LC'} = E_o \begin{bmatrix} \frac{2\cdot n_{glass}}{n_{glass}+n_{air}} & 0 \\ 0 & \frac{2\cdot n_{glass}}{n_{glass}+n_{air}} \end{bmatrix} \begin{bmatrix} \frac{2\cdot n_e}{n_e+n_{glass}} & 0 \\ 0 & \frac{2\cdot n_o}{n_o+n_{glass}} \end{bmatrix} \begin{bmatrix} e^{in_e kL} & 0 \\ 0 & e^{in_\perp kL} \end{bmatrix} \cdot$$

$$\begin{bmatrix} \frac{2\cdot n_{glass}}{n_{glass}+n_e} & 0 \\ 0 & \frac{2\cdot n_{glass}}{n_{glass}+n_o} \end{bmatrix} \begin{bmatrix} \frac{2\cdot n_{air}}{n_{air}+n_{glass}} & 0 \\ 0 & \frac{2\cdot n_{air}}{n_{air}+n_{glass}} \end{bmatrix} \begin{bmatrix} \cos\theta \\ -\sin\theta \end{bmatrix} \qquad (2.51)$$

Then, return back to XY.

$$E_{LC} = R^{-1}E_{LC'} = E_o\begin{bmatrix}\cos\theta & -\sin\theta \\ \sin\theta & \cos\theta\end{bmatrix}E_{LC'}$$

$$= E_o\begin{bmatrix}\cos\theta & -\sin\theta \\ \sin\theta & \cos\theta\end{bmatrix}\cdot\begin{bmatrix}A & 0 \\ 0 & B\end{bmatrix}\cdot\begin{bmatrix}\cos\theta \\ -\sin\theta\end{bmatrix} \qquad (2.52)$$

where A= $\frac{2\cdot n_{glass}}{n_{glass}+n_{air}}\cdot\frac{2\cdot n_e}{n_e+n_{glass}}\cdot e^{in_{//}kL}\cdot\frac{2\cdot n_{glass}}{n_{glass}+n_e}\cdot\frac{2\cdot n_{air}}{n_{air}+n_{glass}}$ and B= $\frac{2\cdot n_{glass}}{n_{glass}+n_{air}}\cdot\frac{2\cdot n_o}{n_o+n_{glass}}\cdot e^{in_{\perp}kL}\cdot\frac{2\cdot n_{glass}}{n_{glass}+n_o}\cdot\frac{2\cdot n_{air}}{n_{air}+n_{glass}}$ , the electrical field perpendicular to the ground is:

$$E_{\perp} = E_o\begin{bmatrix}0 & 0 \\ 0 & 1\end{bmatrix}\begin{bmatrix}\cos\theta & -\sin\theta \\ \sin\theta & \cos\theta\end{bmatrix}\begin{bmatrix}A & 0 \\ 0 & B\end{bmatrix}\begin{bmatrix}\cos\theta \\ -\sin\theta\end{bmatrix}$$

$$= E_o\begin{bmatrix}0 \\ A\cos\theta\sin\theta - B\cos\theta\sin\theta\end{bmatrix} \qquad (2.53)$$

$$E_{\perp} = E_o(A\cos\theta\sin\theta - B\cos\theta\sin\theta) \qquad (2.54)$$

In our experiment,

$$E_{\perp} = E_o(0.903e^{in_{//}kL}\cos\theta\sin\theta - 1.137e^{in_{\perp}kL}\cos\theta\sin\theta)$$

$$= E_o\cos\theta\sin\theta\cdot e^{i\bar{n}kL}(0.903e^{\frac{i\Delta nkL}{2}} - 1.137e^{\frac{-i\Delta nkL}{2}})$$

$$= E_o\cos\theta\sin\theta\cdot e^{i\bar{n}kL}(0.903e^{\frac{i\Gamma}{2}} - 1.137e^{\frac{-i\Gamma}{2}})$$

$$= E_o\cos\theta\sin\theta\cdot e^{i\bar{n}kL}(0.903\cos\frac{\Gamma}{2} + i0.903\sin\frac{\Gamma}{2} - 1.137\cos\frac{\Gamma}{2} + i1.137\sin\frac{\Gamma}{2})$$

$$= E_o\cos\theta\sin\theta\cdot e^{i\bar{n}kL}(-0.234\cos\frac{\Gamma}{2} + i2.04\sin\frac{\Gamma}{2}) \qquad (2.55)$$

Where $\bar{n} = \frac{n_{\Pi} + n_{\perp}}{2}$, $\Delta n = n_{\Pi} - n_{\perp}$

The intensity is

$$I_{\perp} = |E_{\perp}|^2 = I_0\sin^2 2\theta(0.014\cos^2\frac{\Gamma}{2} + 1.04\sin^2\frac{\Gamma}{2}) \qquad (2.56)$$

$$I_{\Pi}=I_{o}-I_{\perp}=I_{0}(1-\sin^{2}2\theta(0.014\cos^{2}\frac{\Gamma}{2}+1.04\sin^{2}\frac{\Gamma}{2})) \qquad (2.57)$$

When the NLC sample acts as a quarter waveplate, $\Gamma=\pi/2$

$$I_{\Pi}=I_{o}-I_{\perp}=I_{0}(1-0.527\sin^{2}2\theta) \qquad (2.58)$$

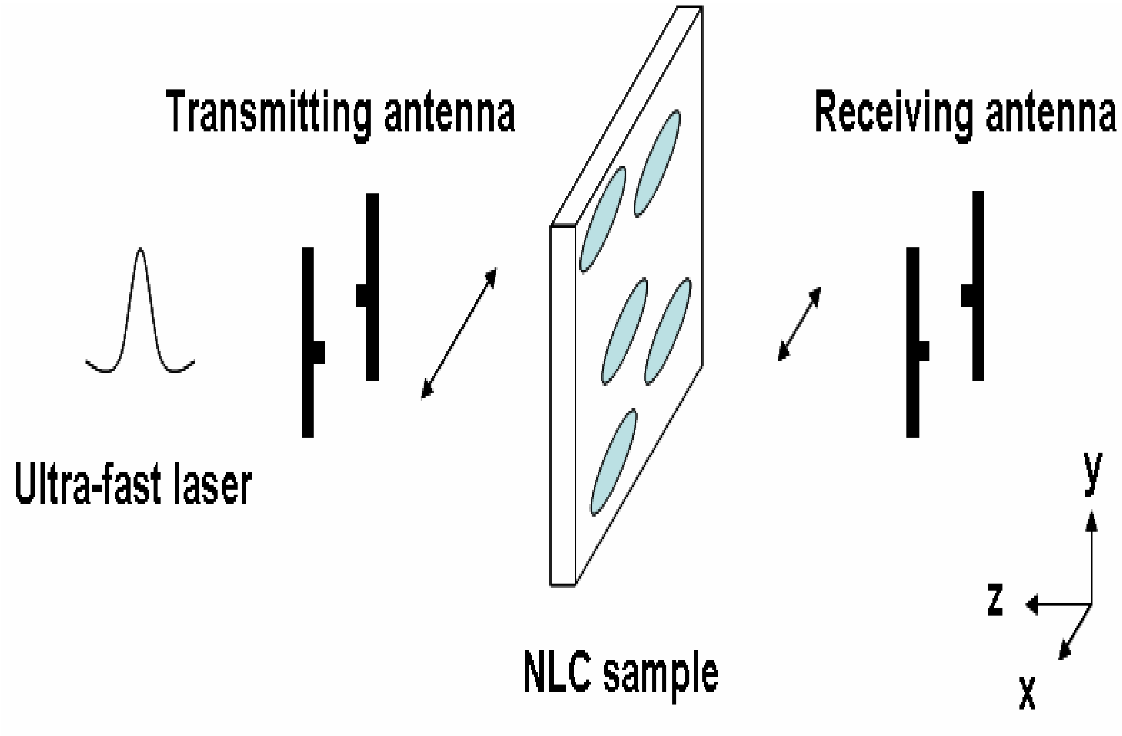

Fig. 2.18 Signal transmitting and receiving are both in the parallel direction

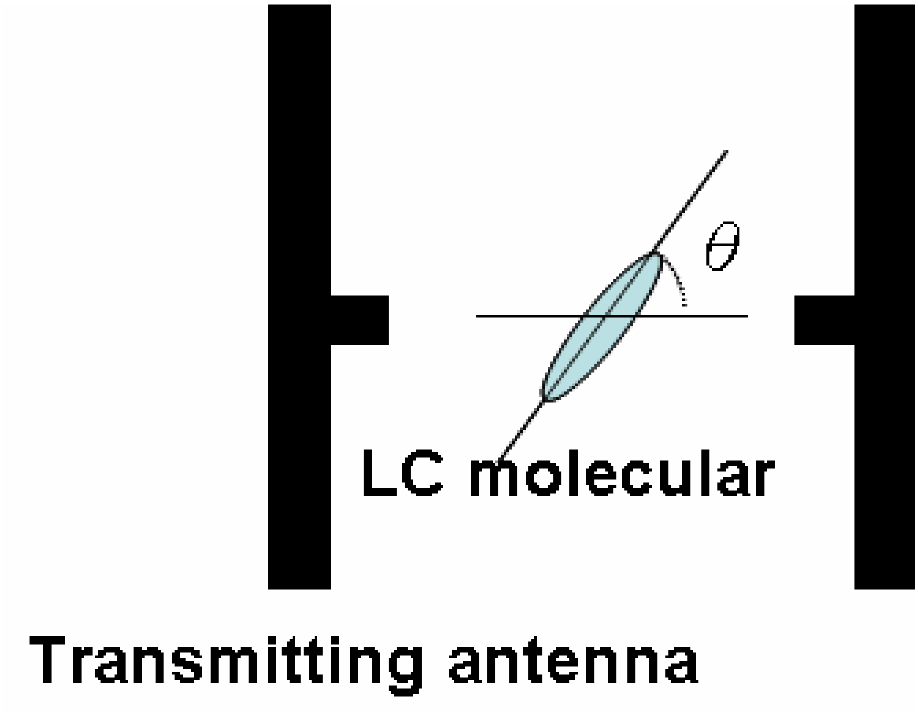

Fig. 2.19 Side view of fig 2.10, θ in this diagram means the angle between antenna horn and long axis of liquid crystal

# 3. Experimental Methods

In chapter 3, we describe our experimental methods, including the mechanism and setup of THz-TDS [35-36] system, procedure of sample fabricating, and data processing.

## 3.1 THz-TDS System

THz-TDS is a powerful technique that allows the broadband generation and detection of the THz field amplitude and phase. A schematic representation of our setup is depicted in Fig.3.1. In this experiment, the device was measured by the conventional THz-TDS system, A diode pumped solid state laser (DPSSL) is used to optically pump a Ti:sapphire laser. This laser produces light pulses at a repetition rate of 90 MHz. The pulses are split in two beams. One of these beams constitutes the so-called pump or excitation pulse. The other beam is referred as the probe pulse. When femtosecond mode-locked laser pulses (1) impinged on a photoconducting material, low temperature grown gallium arsenide dipole antenna (3), which acts as a surface field emitter. Then the THz pulse was collected and guided by gold-coated parabolic mirrors (4) onto the sample, and transmitted through the LC layer (5) between the two electrodes. The transmitted or reflected pulses by the sample are focused onto the THz detector, which in our case is a photoconductive antenna. This antenna is gated by the optical probe pulse and consists of a metallic dipole antenna, which is structured on top of a low-temperature grown gallium arsenide (LT-GaAs). The Ti:sapphire probe pulse that hits the LT-GaAs generates charge carriers, and effectively turns the antenna on for a short time interval. This time interval is determined by the lifetime of the excited carriers and it is typically of a few hundreds of femtoseconds. The carriers are accelerated by the THz electric field and they produce a photocurrent that is measured. The photocurrent is proportional to the THz field amplitude. The transmitted THz pulse was monitored by the probe beam from the identical laser and the same kind of antenna. By connecting the antenna detector to a lock-in amplifier (LIA), when the optical path length of the two branches of the setup (pump and probe) are equal the THz and the probe pulse arrive simultaneously to the antenna. By moving a delay stage, the time window in which the carriers are available in the antenna shifts. Hence, by changing this time window it is possible to monitor the time evolution of the amplitude of the THz pulse, signal from LIA can be easily obtained and analyzed using PC.

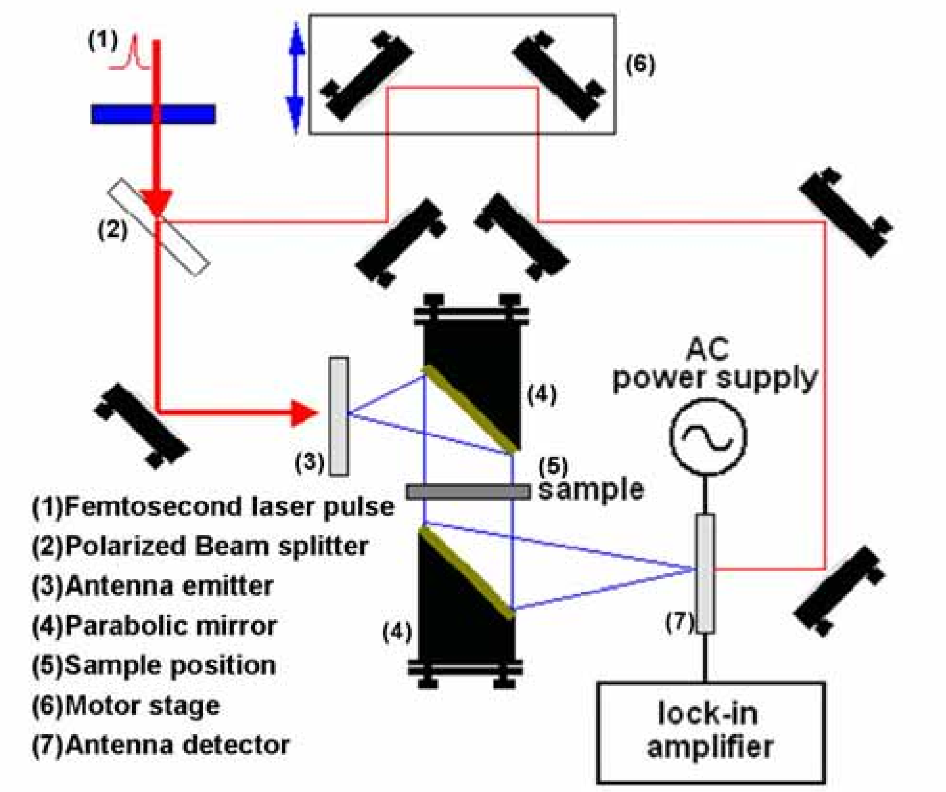

Fig. 3.1 THz-TDS system

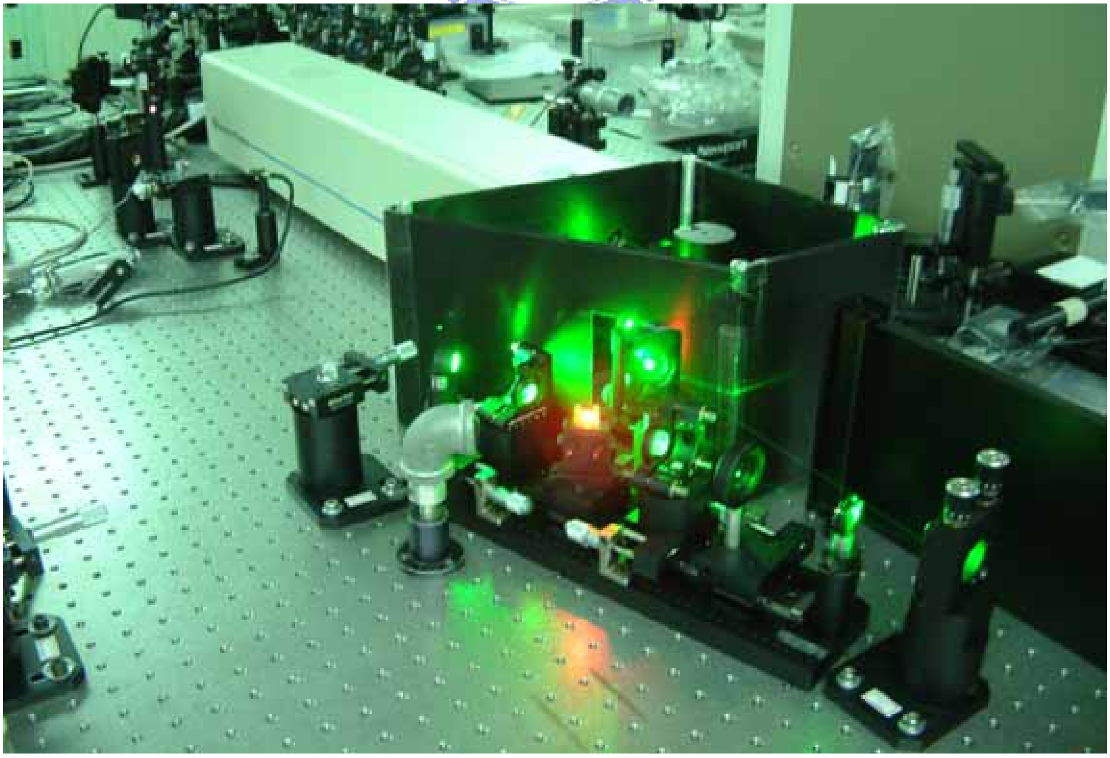

Fig. 3.2 Pictures of Ti-sapphire ultrafast laser

Fig. 3.3 Pictures of THz-TDS system

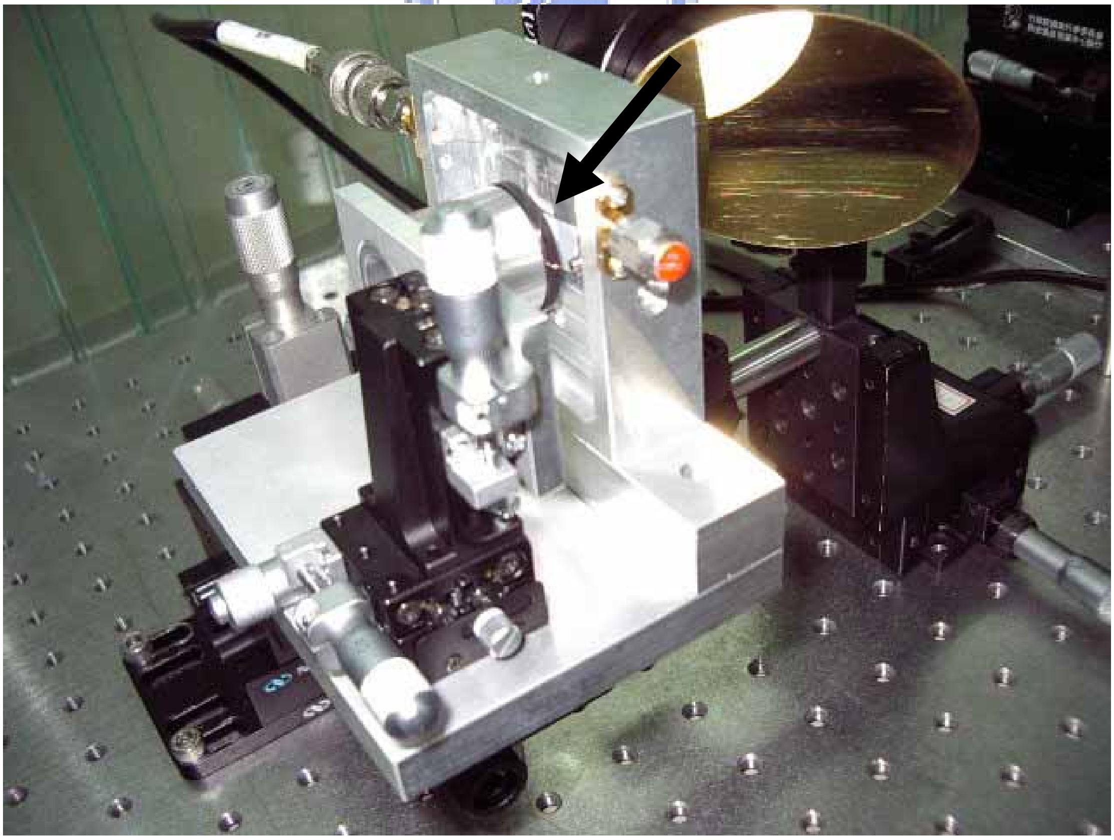

Fig. 3.4 Photoconductive antenna

## 3.2 Sample Fabrication

The sample in this experiment was fabricated by several components, fused silica substrate, copper electrodes, and E7 liquid crystal. First, two pieces of quartz glasses were chosen for substrate, after several cleaning processes treating, dimethyloctadecyl-(3-trimethoxysilyl)-propylammonium- chloride (DMOAP) were coating on them so that the orientation of the E7 was perpendicular to the substrates (so-called homeotropic alignment). The two copper pieces (purity 99.94%) were sandwiched between two substrates as spacers and electrodes. The electrodes were parallel to each other and separated by 11.95±0.05 mm. Then, E7 liquid crystal was filled into the middle of the two substrates, The thicknesses of the substrate and E7 layer were 858±1 and 524±1 μm respectively.

The procedure of manufacturing liquid crystal cell was shown below:

Procedure of manufacturing liquid crystal cell

Glass cutting → Glass cleaning → Alignment layer coating →

Vertical alignment → Sealing the cell → Filling the liquid crystal cell →

Sealing the gap → Sample Checking

Glasses cutting

1. Put on the gloves in order to avoid being cut and pollute glasses.
2. Choose fused silica glass, not ITO coating glasses because that THz can not pass through the ITO film.
3. Using the diamond knife-edge to cut the glasses, in this experiment, 15mm×30mm and 15mm×40mm glasses were chosen for upper half and next half, respectively.
4. Cut two pieces of copper sheets by mechanical-finishing. 15mm× 15mm in length and width, the thickness is 500μm.
5. Measure the thickness of the glasses and copper sheets by screw micrometer.

Fig. 3.5 Glass cutting

## Glass cleaning

1. Put on the mouthpiece to avoid the damage causing by organic chemistry matter volatility.
2. Mount the glasses on Teflon foundation of the beaker; add water to surpass the glasses up to, and pour into the cleaner.
3. Put the beaker into the supersonic oscillator, after shaking it for 5 minutes, take it out and flush it by the distilled, then use the nitrogen to air-dry. The function of this step is for eliminating dusts, ashes and grimes on the glasses.
4. Load the glasses into the beaker with acetone, shake it for five minutes. The function of this step is for eliminating oil-slick and organism on the glasses.
5. Load the glasses into the beaker with methyl alcohol, shake it for five minutes. The function of this step is for eliminating particles on the glasses.
6. Load the glasses into the beaker with pure water, shake it for five minutes. The function of this step is for eliminating the residual solvent on the glasses.
7. After using nitrogen to air-dry, put the glasses into 100 degrees centigrade ovens to dry out the moisture.
8. The copper sheets clean procedure is the same as the glasses.

Fig. 3.6 Equipment for glass cleaning

Alignment layer coating and Vertical alignment

1. Vertically alignment was used in this experiment, therefore DMOAP (dimethyloctadecyl-(3-trimethoxysilyl)-propylammonium-chloride) was chosen. Put the DMOAP solution in the room temperature to warm for 20 minutes. Additionally, acetic acid was prepared for help DMOAP cohere on the glasses.
2. Put the glasses into a beaker with solution which mix water, acetic acid, 50% DMOAP solution according to 95:3:2 in weight percentage concentration.

3. Put the beaker into the supersonic oscillator, after shaking it for 15 minutes, take it out and flush it by the distilled, then use the nitrogen to air-dry.
4. Put the glasses into 100 degrees centigrade ovens to dry out the moisture for 2 hours. Attend that the surface which will contact with liquid crystal should be upturned.

Fig 3.7 Equipment for vertical alignment

Sealing the cell

1. Blow the glass with the nitrogen to remove the dust and the pellet on the substrate surface.
2. Assemble two glass substrate plates and copper sheets by Fig.3.8 way.

3. Fix the cell with the clips; spread the AB glue all around in the sample, only leave a gap for filling the liquid crystal.
4. Do not take off the clip before the glue drying.

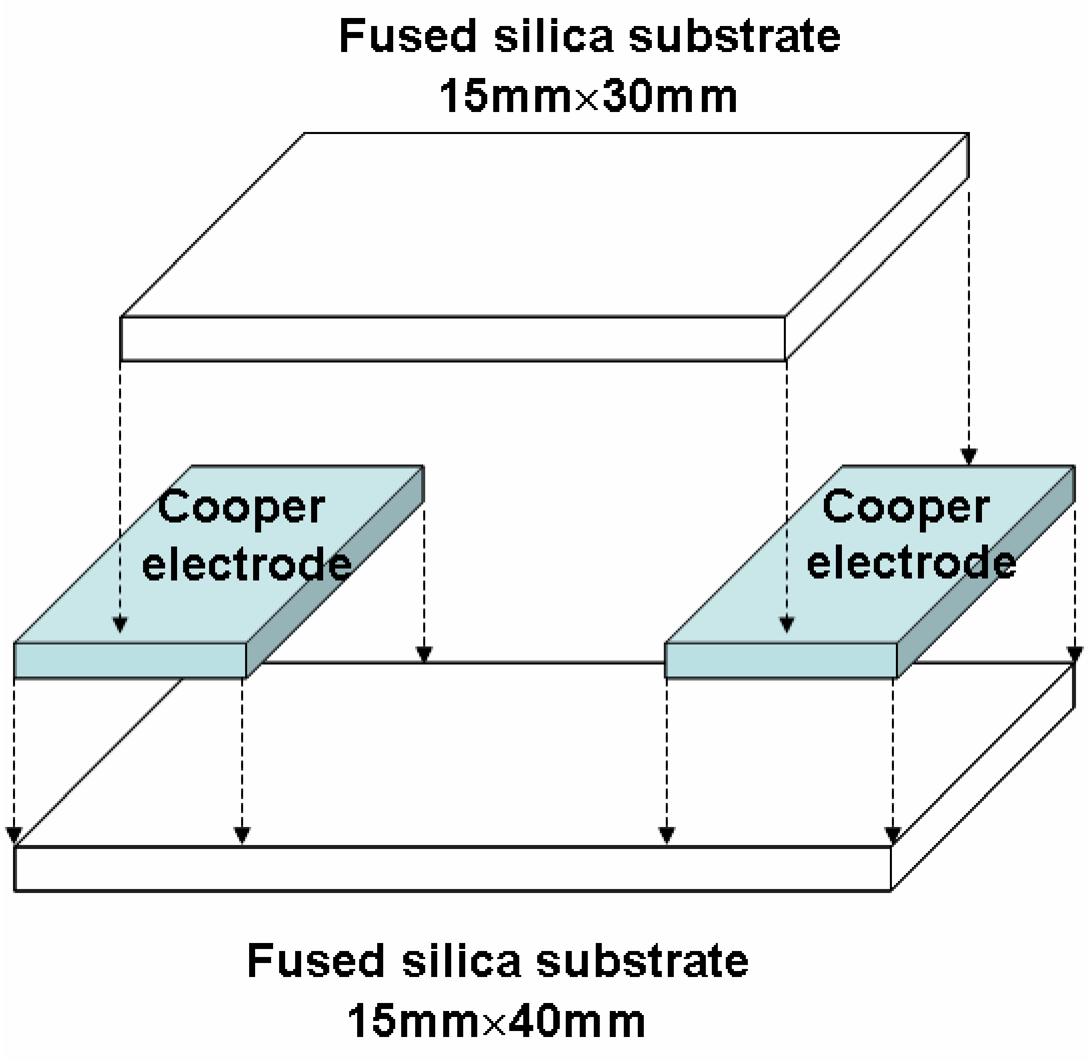

Fig. 3.8 The alignment of the NLC sample

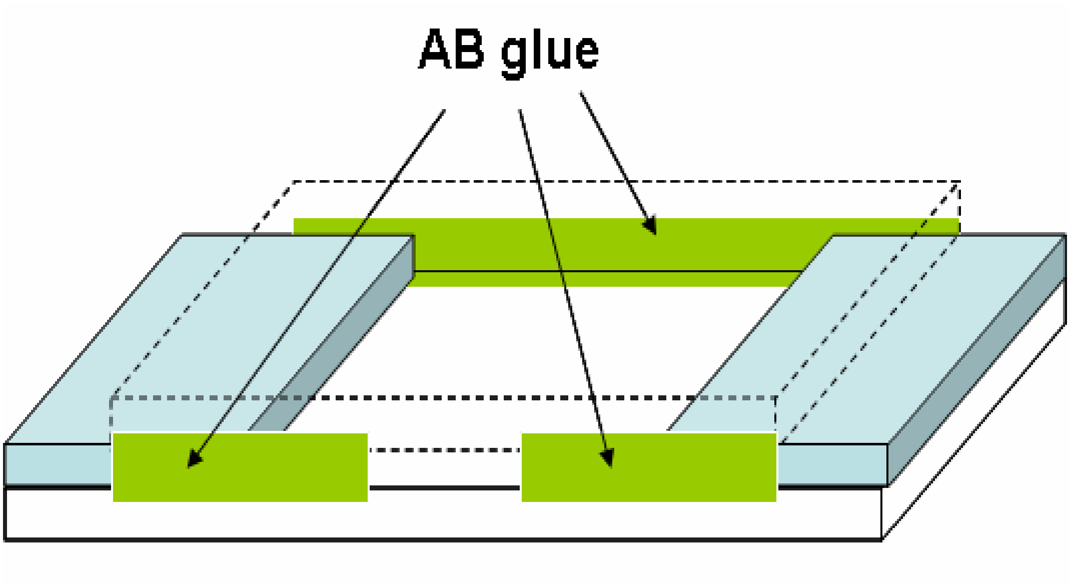

Fig. 3.9 Spread AB glue around the NLC sample but left a gap for filling liquid crystal

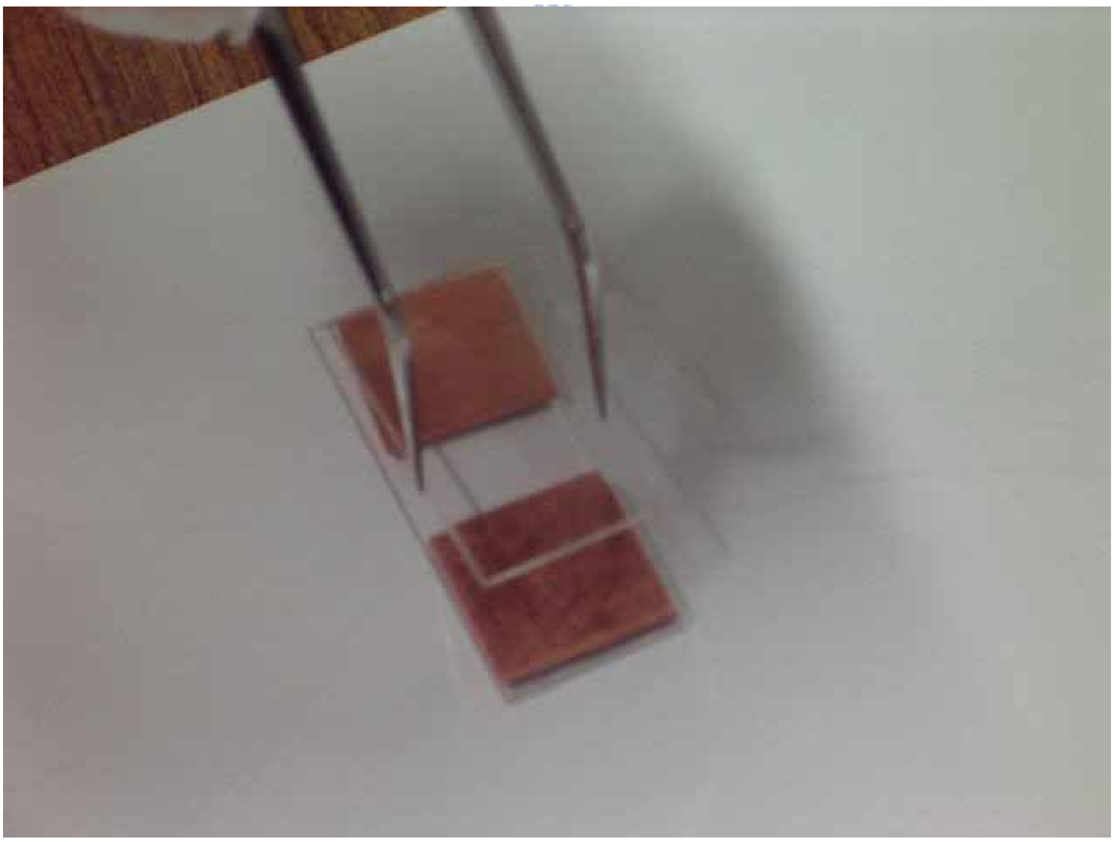

Fig. 3.10 Assemble two glass substrate plates and copper sheets

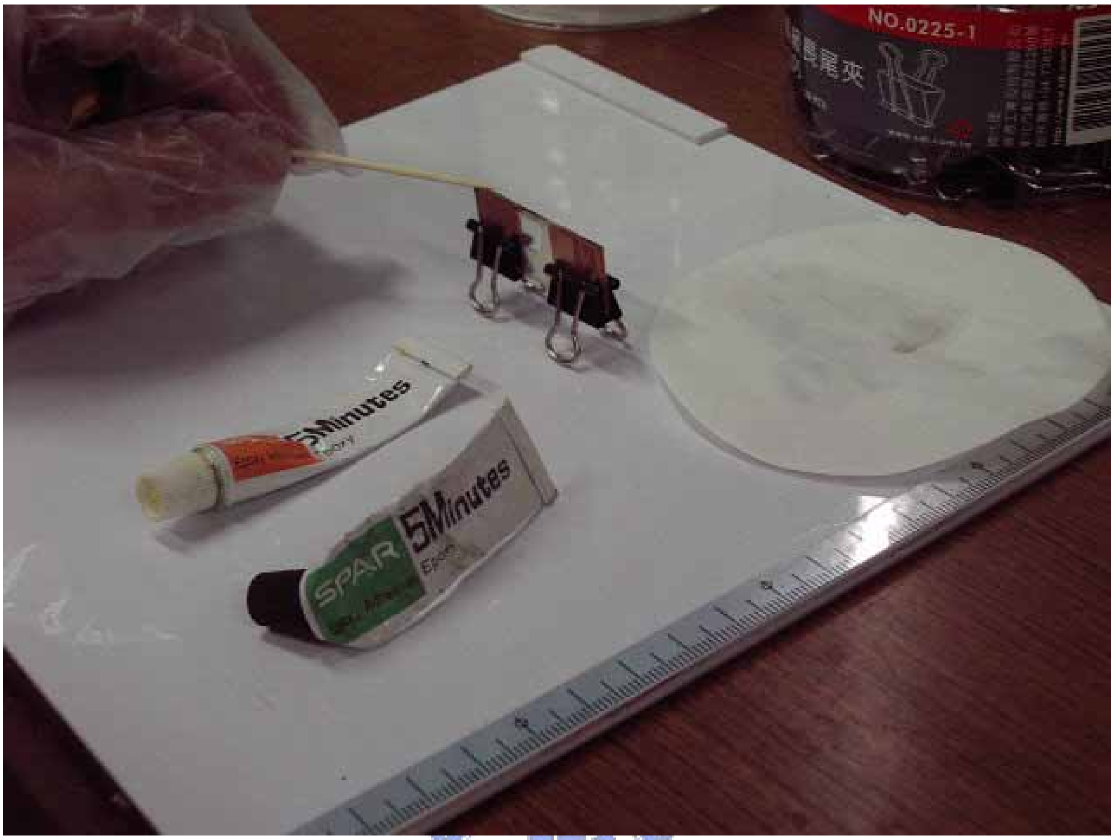

Fig. 3.11 Spread the AB glue all around in the sample

Filling the liquid crystal cell and Sealing the gap

The properties of E7 are listed in table 3.1.

| Manufacture | Merck Ltd |
|---|---|
| Dielectric anisotropy $\Delta\varepsilon$ 20° C | $13.8\varepsilon_0$ |
| $\varepsilon_{//}$ 20° C | $19.0\varepsilon_0$ |
| $\varepsilon_{\perp}$ 20° C | $5.2\varepsilon_0$ |
| Elastic constants K1 20° C | 11.10 $10^{-12}$N |
| K3 20° C | 17.10 $10^{-12}$N |
| K3/K1 20° C | 1.54 |

Table 3.1 Properties of E7

1. The cell gap is enough wide, vacuum is not necessary, directly drip liquid crystal into the cell, pay attention that do not produce bubbles.
2. Seal the gap by using AB glue.

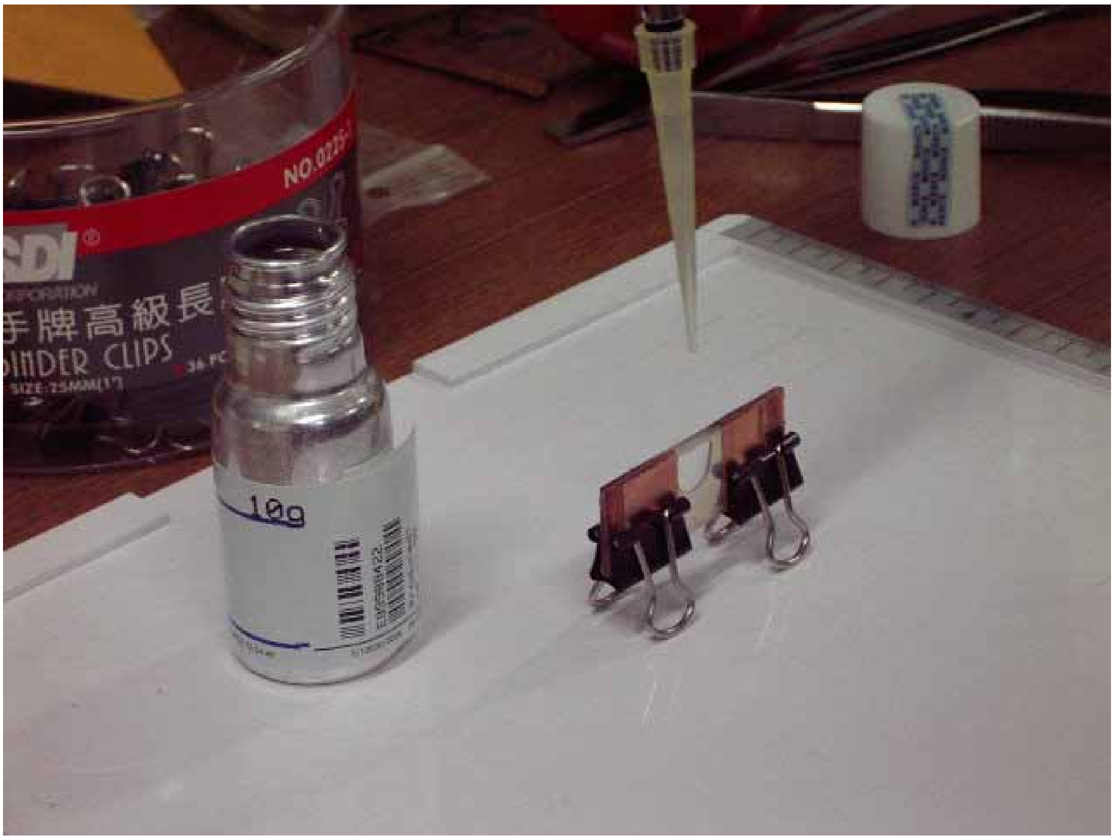

Fig.3.12 Fill liquid crystal into the cell

Sample Checking

1. Observe the sample outward appearance, whether the liquid crystal leak off.
2. There is a simple way for sample checking, we put the NLC sample among cross polarizer, if aligned effect is good, we can discover slightly light to shade change when rotating the cell.
3. Measure the sample thickness by screw micrometer.

Fig. 3.13 Check the alignment

Fig 3.14 Picture of NLC cell

## 3.3 Data Processing

In this experiment, we use the “high voltage source” to generate high voltage, and use the “pulse generator” to transfer the high voltage to voltage pulse. Therefore, if we need a 100V peak to peak square wave to be our bias, we should setup these machines and generate 200V by the high voltage source, and connect it to the pulse generator, then the $100V_{p\text{-}p}$ signal would be obtained from the output of the pulse generator. Of course, the frequency of the output signal can be tuned by changing the synchronized input signal.

Using THz-TDS system, amplitude and phase information can be easily obtained. But not only information of liquid crystal, additional influences of glass substrates, and air are also included in the original data, we can resolve this problem by the following way: at first, we measure the waveform of zero bias applying for referential data, which include above-mentioned information, and then we apply bias voltage to change the refractive index of NLC cell and measure the result (of course it also includes above-mentioned information), subtract the reference and get the data which only includes the influence of liquid crystal. The transmitted THz spectra were deduced from the time domain of the THz pulse with fast Fourier transform (FFT) algorithm.

Two time-domain waveforms can be used to obtain frequency-domain spectra using numerical fast Fourier transform, and then the experimental data divided by the reference should be the amplitude transmittance of this sample. The difference of phase was the phase retardation. Compare the phase retardation data of different voltages applied to NLC samples; the voltage versus phase shift curve can easily be drawn. Also, v-Φ curve in various frequencies are obtained.

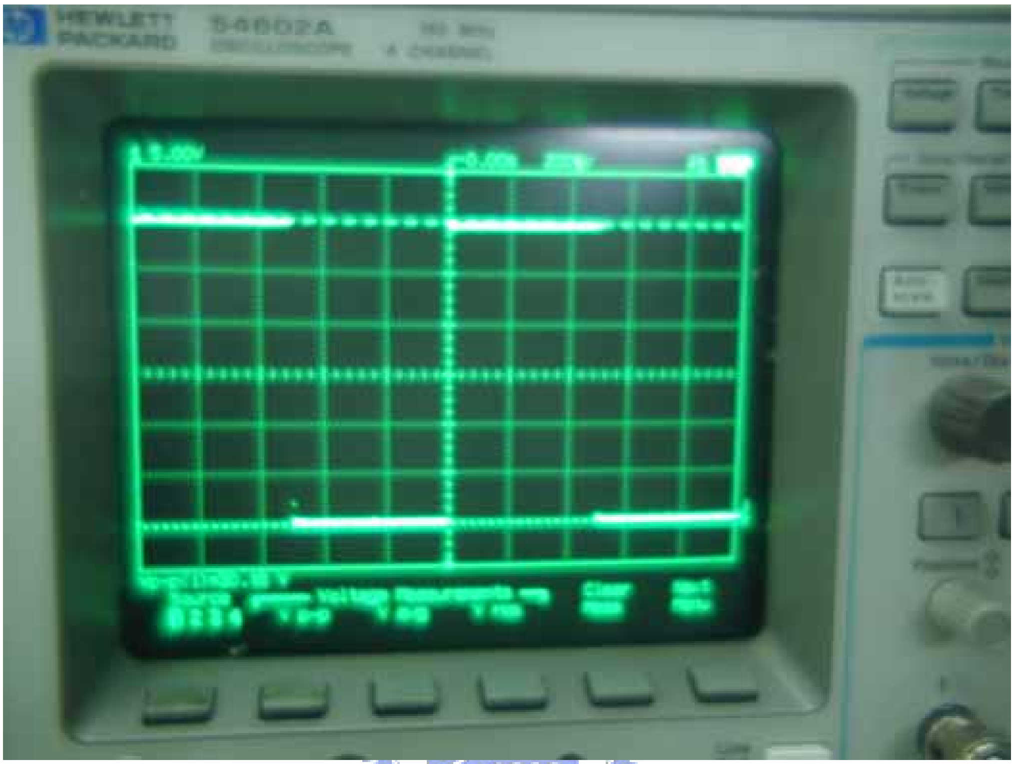

Fig. 3.15 The oscilloscope

Fig. 3.16 The high voltage source and the pulse generator

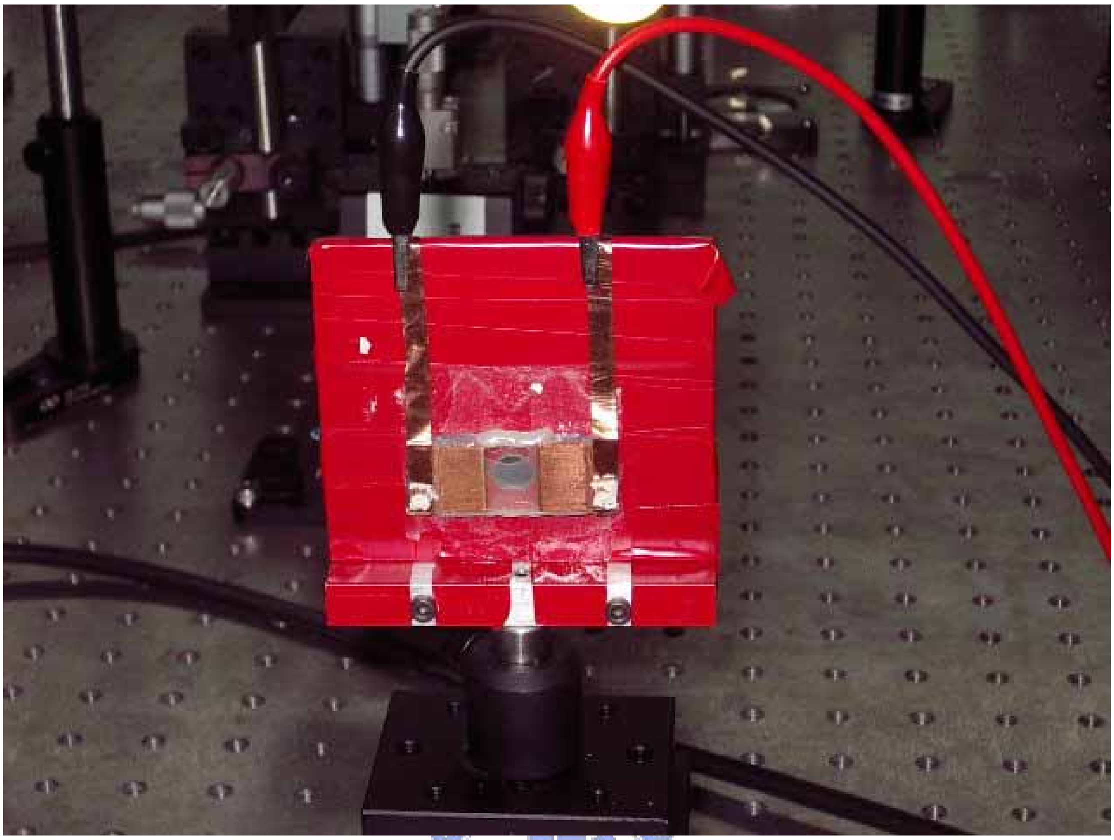

Fig. 3.17 The experimental sample with holder and conductive equipment

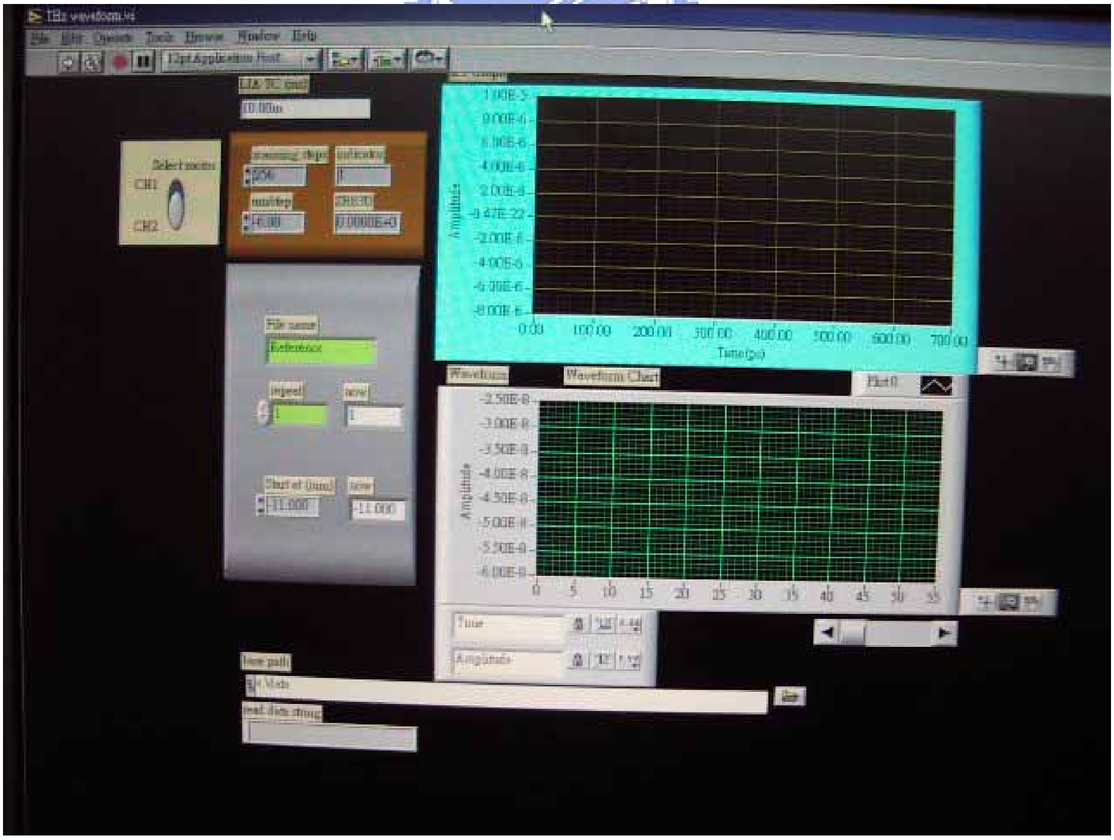

Fig. 3.17 Program for THz-TDS system

# 4. Experimental results and discussion

In this chapter, we show the experimental data, the theoretical curve and discussion, and then compare with the former work to find the characteristics and advantages.

## 4.1 THz-TDS Waveforms and Spectra

Using lock-in amplifier, we can obtain the waveform in time domain, after fast Fourier transform (FFT), spectrum in frequency domain can also be obtained. The reference signal in fig 4.1 means the THz signal which was received by receiving antenna in our experimental system without passing though the NLC sample. The amplitude of signal was expressed in the form of electrical field. In this experiment, we scanned the THz radiation for ~70 Pico seconds, which equals to scan 21 millimeters in the space. By observing fig 4.1, we can get the main signal amplitude is $2.92\times10^{-4}$ units, and locates between 0 to 10 ps, the swing signal behind the main signal mainly comes from the moisture in the air, the SN ratio (signal-noise ratio) can be observed in fig. 4.2 is about $10^{6}$, the bandwidth is about 1 THz.

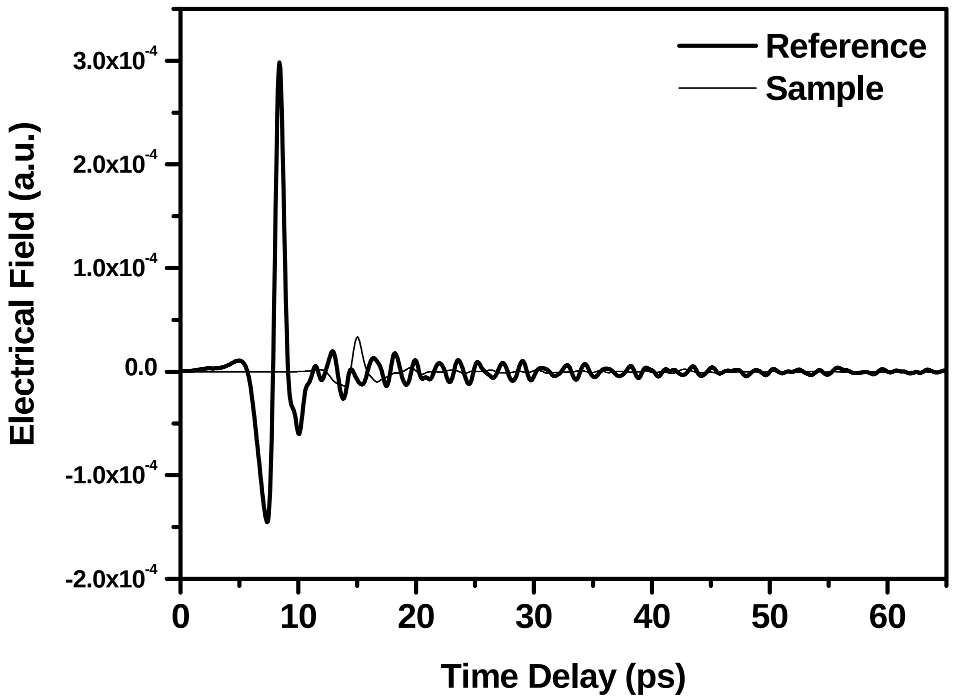

Fig. 4.1 Waveform of reference and NLC sample in this experiment

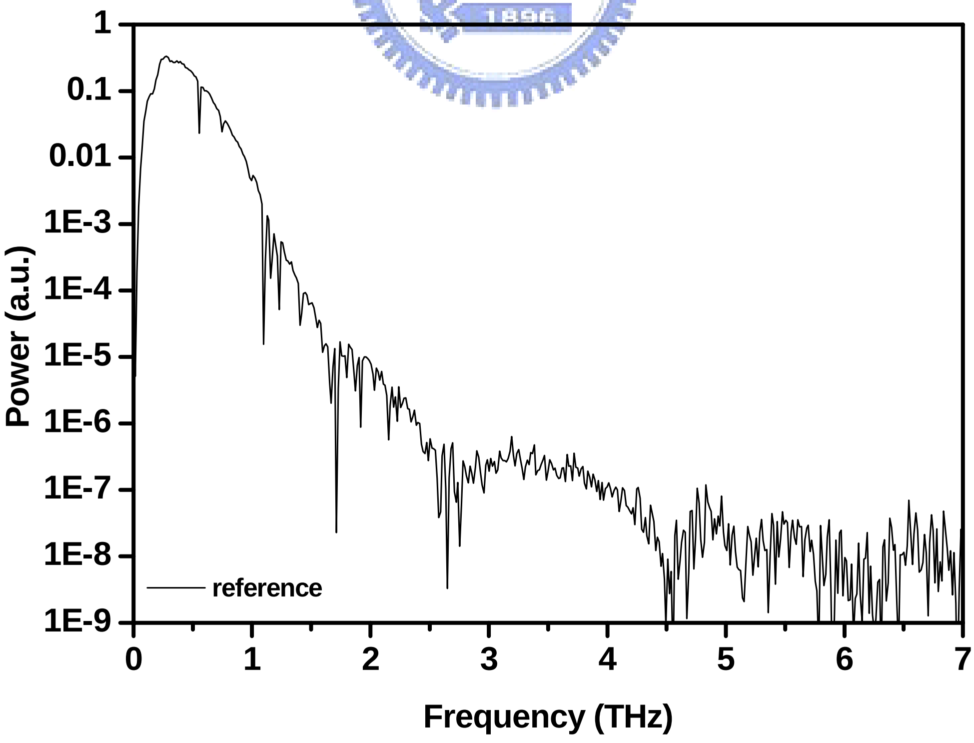

Fig. 4.2 Spectrum of the reference signal

By observing fig 4.1 again, we know the amplitude of sample signal (THz radiate though the NLC sample with 0V applied voltage) is smaller than the reference signal; the peak value is probably $3.35\times10^{-5}$ units, therefore, transmittance of the sample can be derived by dividing the reference data, it is 11.47%. Additionally, there is a period of time delay between main signal and sample signal, we can get 6.603ps time delay by the peak value of the sample signal (15.007ps) subtracting the peak value of the main signal (8.404ps), it also means 1.981 mm optical difference in space.

If we carefully observe the part after the main signal in fig 4.3, we can know that beside the oscillation which was produced by the moisture, there are also some multi-refract signals mixed in it.

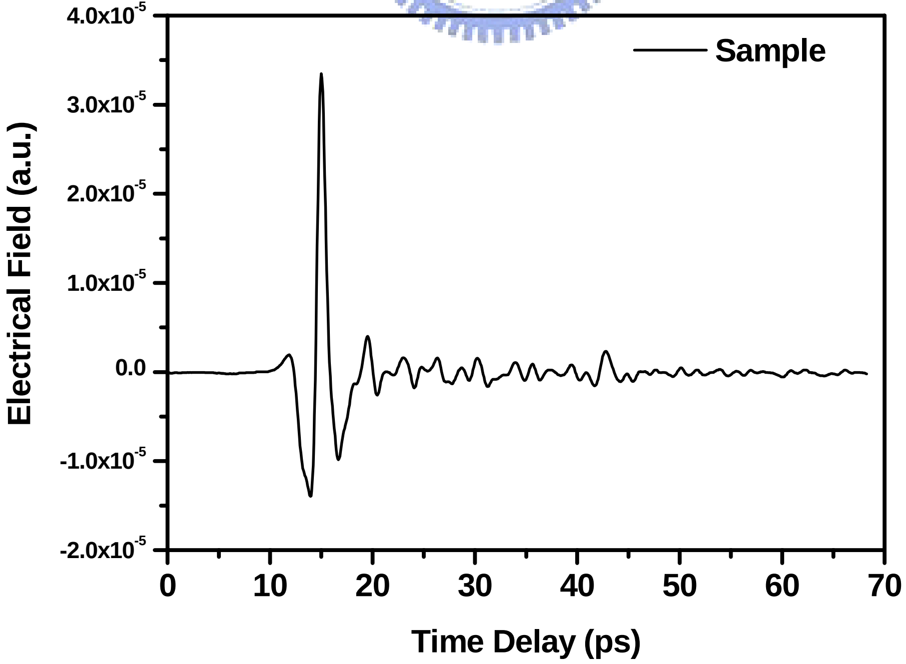

Fig. 4.3 The sample signal without any applied voltage.

Fig 4.4 is the power spectrum of the reference data and the sample data; we can see the phenomenon in 0.55THz, 0.7THz, 1.0THz, etc. the moisture absorption occurred. The maximum value of the power spectrum locates at ~0.3THz.

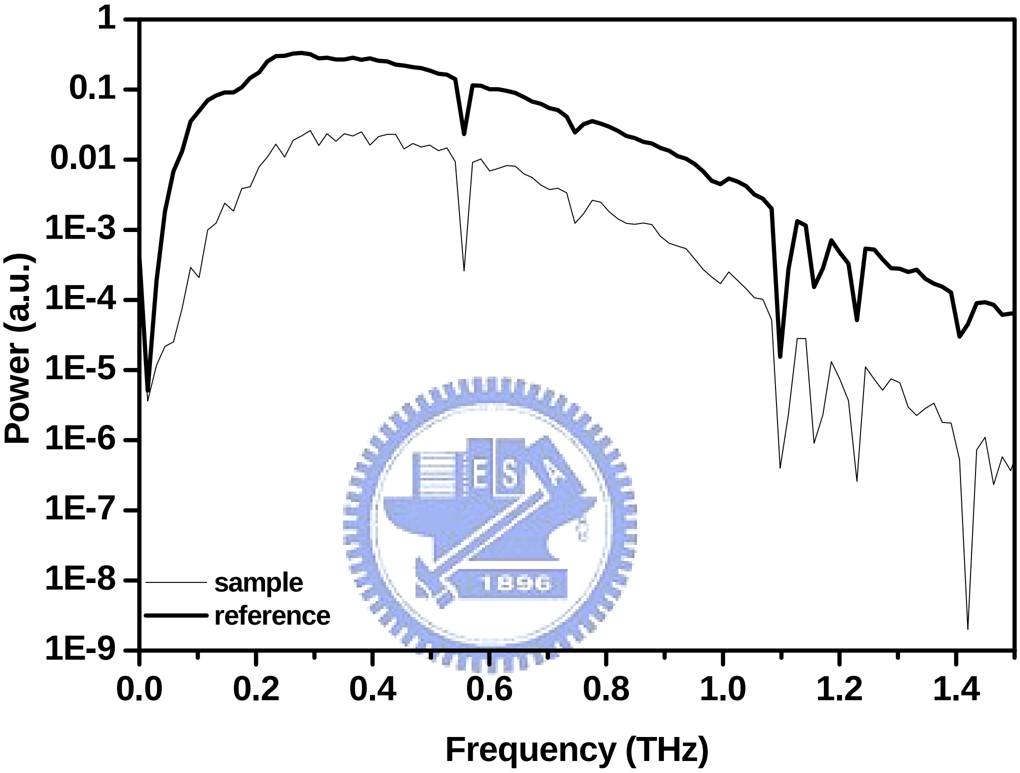

Fig. 4.4 The reference and sample spectrum

Refract index is frequency dependent; therefore the refraction coefficients measured in the visible range are not suitable use in the THz range. Fortunately, refract index of E7 in THz range was measured. In THz range, $n_e$~1.75 and $n_o$~1.6; the birefringence in THz range was also determined (~0.17). These experimental results are shown in Fig.4.5.

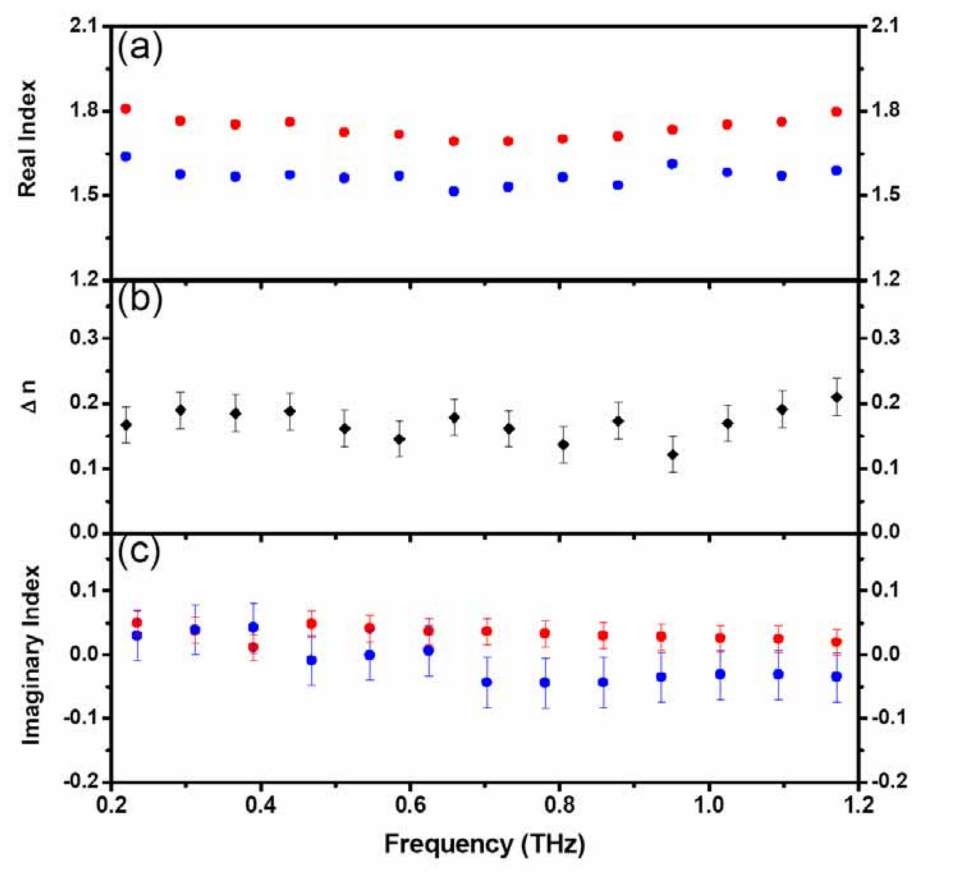

Fig. 4.5 Refract index of E7 in THz range

## 4.2 Electrically Controlled Phase Shifter

### 4.2.1 In-Plane Switch Shifter

The temporal waveforms of the THz beam passing through the 500μm-thick LC phase shifter at various applied field are illustrated in Fig. 4.6. The total scanning range for the time delay was more than 70 ps, and we only show the 10~20 ps for clearly observing the main waveform, and emphasize it in fig. 4.7, the transmitted THz waves for 0V voltage applying show obvious time delay to the wave for 125V voltage applying. The spectral amplitude and phase of the transmitted THz wave were deduced by fast Fourier transform (FFT) algorithms.

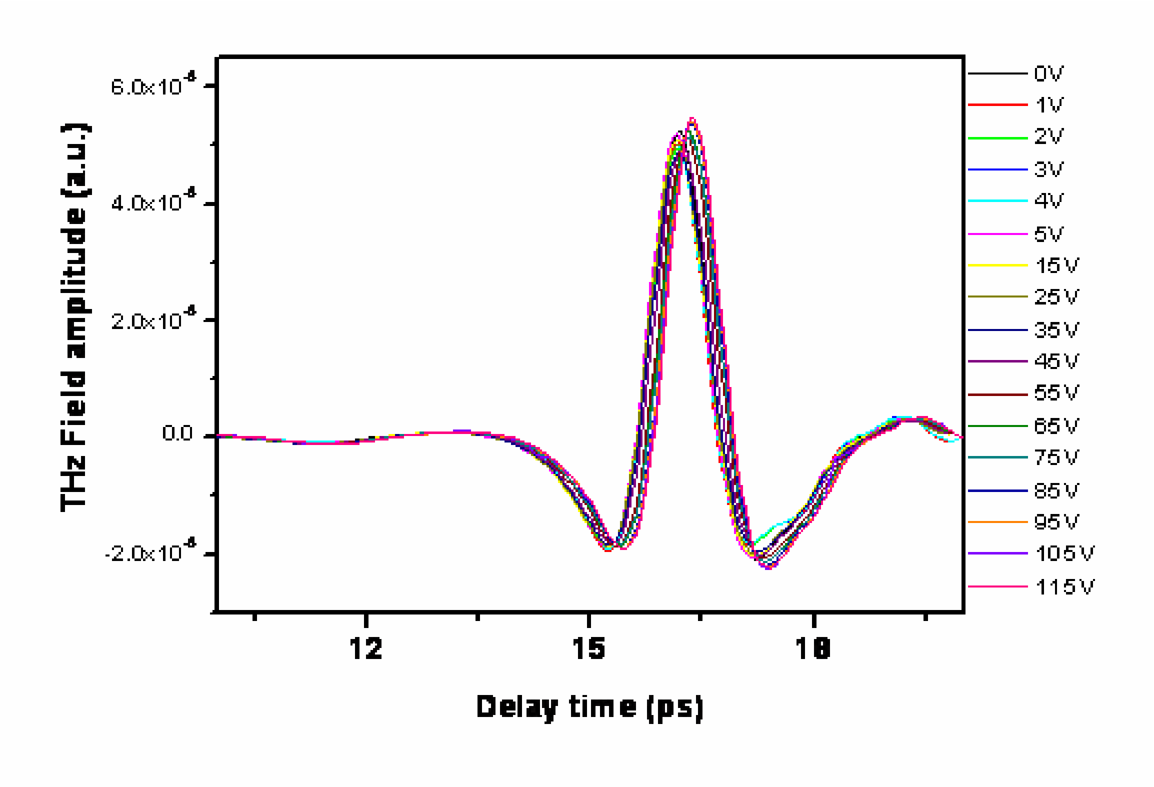

Fig. 4.6 The temporal waveforms of the THz pulse transmitted through the E7 sample at various applied voltages

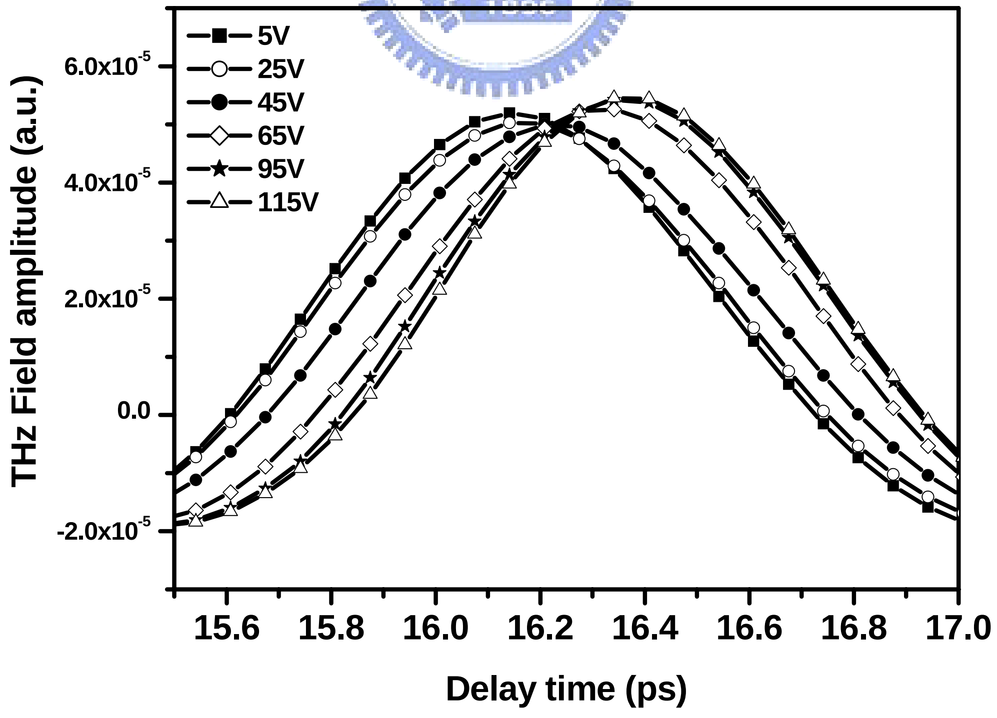

Fig.4.7 The close-up of the temporal waveforms

According to eq. 2.47, the phase shift is proportional to the product of the effective index change $\Delta n_{eff}$ and frequency of the electromagnetic wave. The THz wave is thus expected to experience a larger phase shift at the higher frequencies in the measured THz range. This is also confirmed in Fig. 4.8. The data for the 500μm-thick cell at 1 THz are also show in Fig. 4.8. Maximum phase shift of 84.4° have been obtained at 1 THz by using NLC cells. But 84.4° phase shift is not enough for a quarter wave plate, additionally, compare the in-plain switch phase shifter to the copper electrode phase shifter which will be described in section 4.2.2, the theoretical prediction curve is harder to draw, and the fabricated process is more complex and expensive. Alternatively, newly developed liquid crystal material with high birefringence can be explored for this application. In the experiments, this can be explained simply by considering the Fresnel equations. The ordinary and extraordinary refractive indices of E7 are 1.62 and 1.79, respectively. With the increasing applied voltage, the effective refractive index of LC will increase from 1.62 to 1.79 and become closer to the refractive index of quartz substrate ~1.9. The transmitted field will then increase according to Fresnel equations.

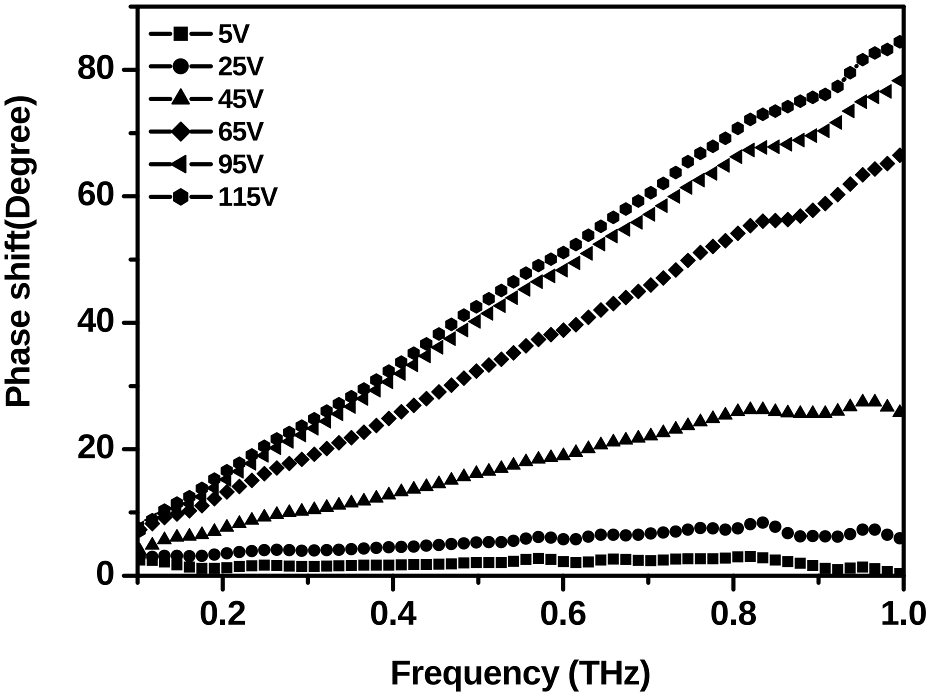

Fig. 4.8 The phase shift from 0.20 to 1.00 THz with varying the driving voltages

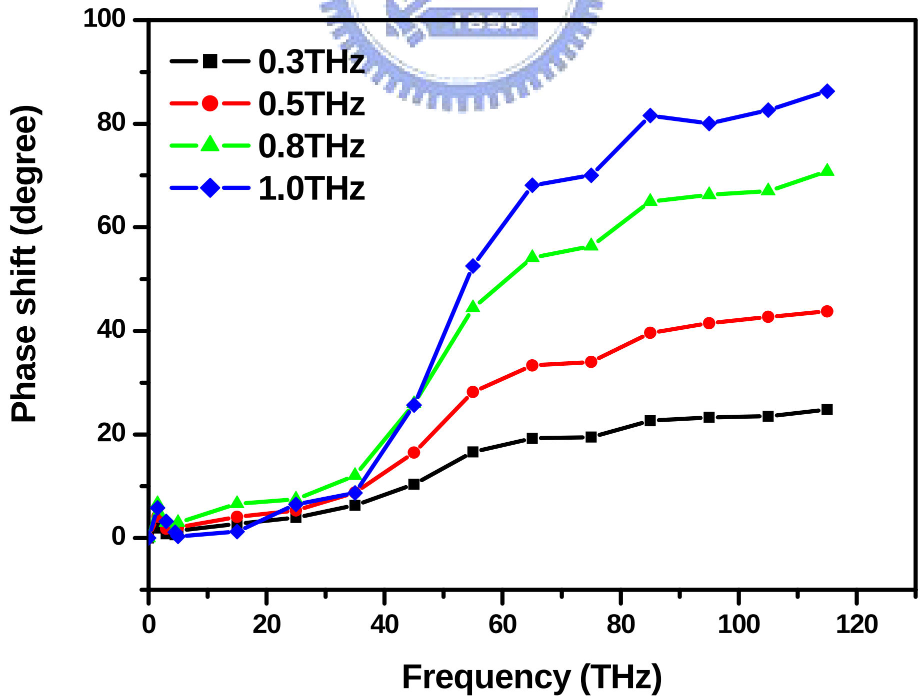

Fig. 4.9 The phase shift as a function of driving voltage for several frequencies.

### 4.2.2 Copper Electrode Phase Shifter

The temporal waveforms of the THz wave, which transmitted through the device at various applied voltages, are shown in Fig. 4.10. In Fig. 4.11, we show the experimental data from 14 to 16 ps so as to emphasize the time shifting of the THz waveforms. The transmitted THz signals exhibit clear large delay and transmittance for the increasing applied voltages in time domain. The reason is mentioned below. The $n_o$ and $n_e$ of E7 are 1.62 and 1.79, respectively, at 0.3 THz. With increasing applied voltages, the effective index of E7 will rise from 1.62 to 1.79 and become closer to 1.95 which is the index of quartz substrate. Along the Fresnel equation, the transmitted THz field increases at the two interfaces between LC layer and quartz substrate.

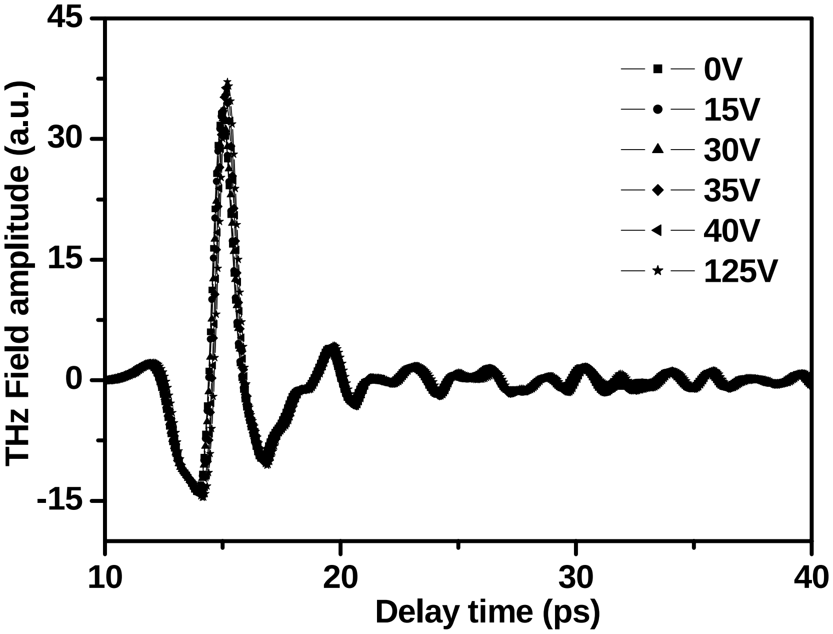

Fig. 4.10 The temporal waveforms of the THz pulse transmitted through the E7 sample at various applied voltages

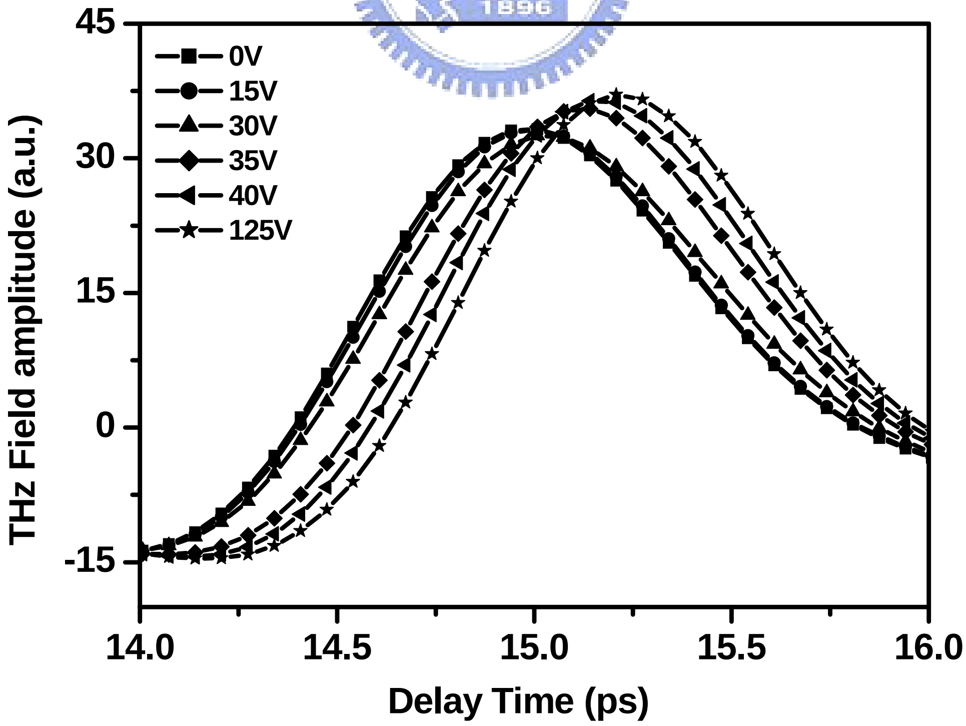

Fig 4.11 The close-up of the temporal waveforms from 14 to 16 ps

The transmitted THz spectra were deduced from the temporal profiles of the THz pulse with fast Fourier transform (FFT) algorithms. Fig. 4.12 is the phase shifts with 0.20 to 1.00 THz by varying the driving voltages. According to equation (2.34),

$$\delta = {2\pi d f \Delta n_{eff}(v)} \big/ {c} \qquad (2.34)$$

The larger phase shift is expected with increasing frequency.

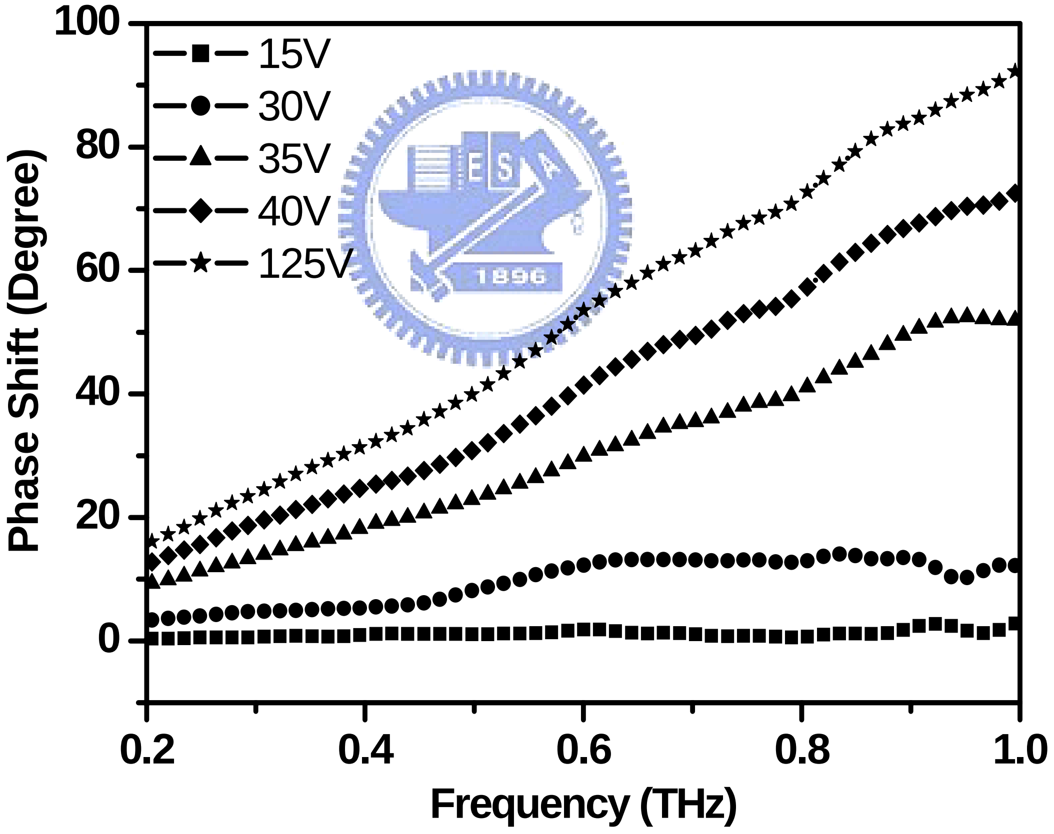

Fig. 4.12 The phase shift from 0.20 to 1.00 THz with varying the driving voltages

According to equation (2.35), the threshold voltage of the NLC sample can be derived by mathematical computation software. In this experiment, we substitute each parameter to obtain the answer by using the convenient software, “MathCad”.

$$v := \pi \cdot \sqrt{\frac{17.1 \cdot 10^{-12}}{13.8 \cdot 8.85 \cdot 10^{-12}}} \cdot \frac{12 \cdot 10^{-3}}{524 \cdot 10^{-6}}$$

$$v = 26.921$$

We obtain 26.9 volts for threshold voltage of our sample; the mention is theoretically we should apply more than 16.9 volts, the liquid crystal molecules can be rotated by electrical field.

Then, we can calculate our theoretical v-Φ curve, form (2.45) and (2.46), we know the theoretical curve divides into two parts, therefore we use MathCAD once more, calculate the two parts of curves with each other.

(a)For $0<v-v_{th}<<v_{th}$

$$\Delta n_{eff}(v) = (n_e - n_o)\frac{n_o}{n_e}\left[\left(1+\frac{n_o}{n_e}\right)\left(\frac{v-v_{th}}{v_{th}}\right)\right] \qquad (2.50)$$

$$\rightarrow \qquad n(v) := 0.17\cdot\left(\frac{1.62}{1.79}\right)\cdot\left(1+\frac{1.62}{1.79}\right)\cdot\left(\frac{v-26.9}{26.9}\right)$$

$$\delta = {}^{2\pi d f \Delta n_{eff}(v)}\!\big/_{c} \qquad (2.44)$$

$$\rightarrow \qquad \phi(v) := \frac{180}{\pi}\cdot n(v)\cdot\frac{2\pi\cdot 0.9956\,10^{12}}{3\cdot 10^{8}}\cdot 524\,10^{-6}$$

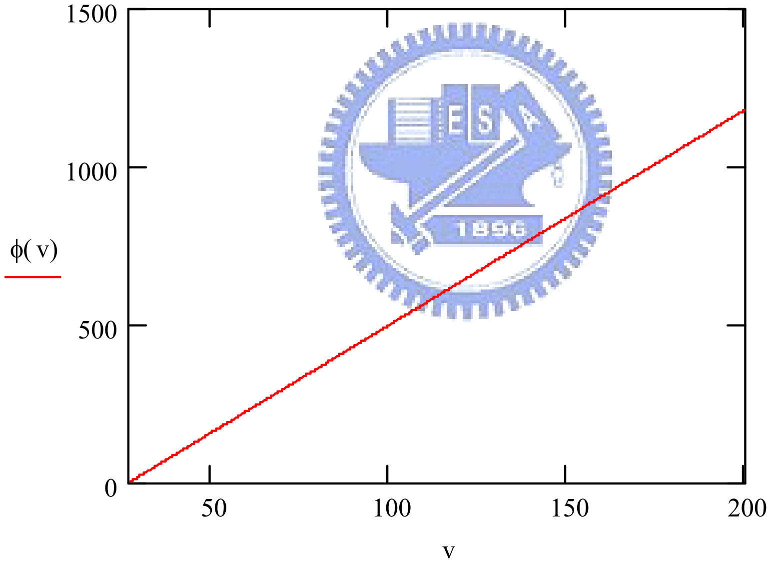

$v := 5, 15..\ 125$

$\phi(v) =$

| |
|---|
| -149.383 |
| -81.172 |
| -12.96 |
| 55.251 |
| 123.463 |
| 191.674 |
| 259.886 |
| 328.097 |
| 396.309 |
| 464.52 |
| 532.732 |
| 600.943 |
| 669.154 |

(b)For $v\text{-}v_{th} \gg v_{th}$

$$\Delta n_{eff}(v) = (n_e - n_o)\left[1-\frac{2}{v}\left(\frac{k_3}{\varepsilon_a\varepsilon_0}\right)^{\frac{1}{2}}\frac{L}{d}\right] \qquad (2.51)$$

$$\rightarrow \quad n(v) := 0.17\cdot\left[1-2\cdot\left(\frac{17.1\cdot 10^{-12}}{13.8\cdot 8.85\cdot 10^{-12}}\right)^{\frac{1}{2}}\cdot\frac{12\cdot 10^{-3}}{v\cdot 524\cdot 10^{-6}}\right]$$

$$\delta = {}^{2\pi d f \Delta n_{eff}(v)}\!\big/_{c} \qquad (2.44)$$

$$\rightarrow \quad \phi(v) := \frac{180}{\pi}\cdot n(v)\cdot\frac{2\pi\cdot 0.9956\times 10^{12}}{3\cdot 10^{8}}\cdot 524\cdot 10^{-6}$$

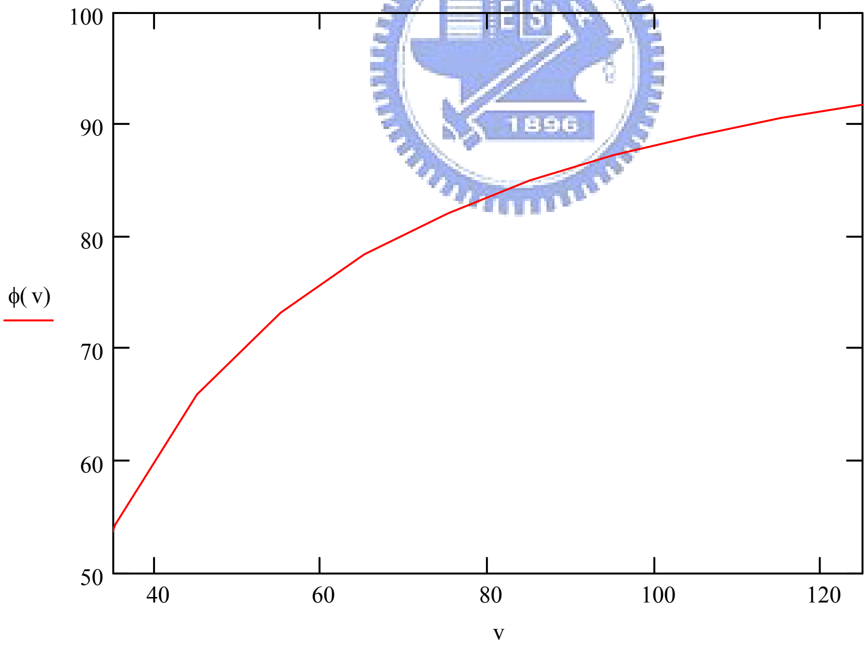

$v \equiv 5, 15..\, 125$

$\phi(v) =$

| |
|---|
| -258.365 |
| -15.171 |
| 33.468 |
| 54.313 |
| 65.893 |
| 73.263 |
| 78.365 |
| 82.106 |
| 84.967 |
| 87.226 |
| 89.055 |
| 90.565 |
| 91.834 |

We combine the $0<v-v_{th}<<v_{th}$ part of (a) and the $v-v_{th}>>v_{th}$ part of (b), a theoretically curve in one frequency can be obtained. If we want to obtain the theoretical curve in another frequency, so long as change the frequency value for the new one. Fig 4.13 shows the theoretically curve in ~0.3, ~0.6, ~0.8 and ~1.0 THz, respectively.

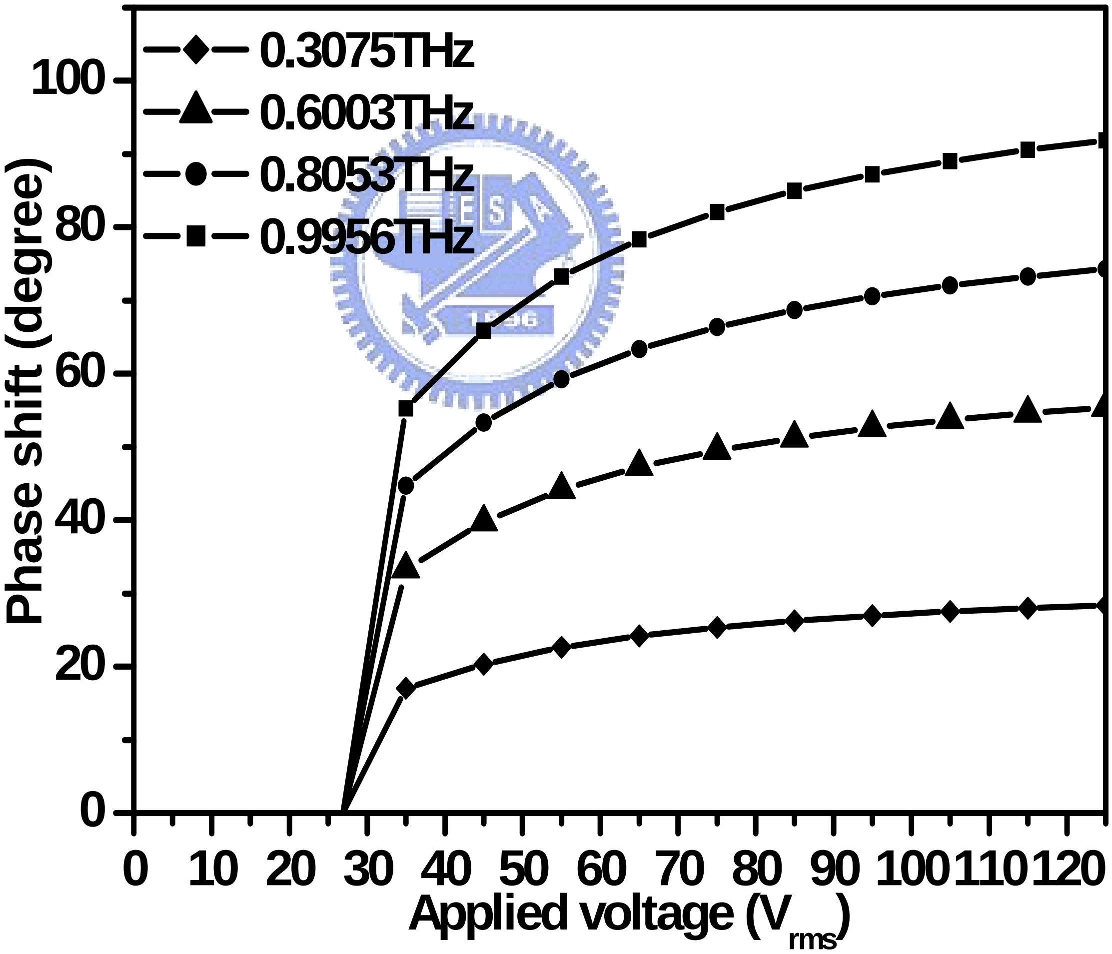

Fig. 4.13 The theoretical curves in different frequency

Fig. 4.14 shows the phase shifts as a function of driving voltage for 0.31, 0.60, 0.81 and 1.00 THz. A maximum phase shift of 93.7° was obtained at 1.00 THz when the LC cell was driven at 125 V (rms). For a 524-μm-thick E7 layer, the theoretical phase shift is 91.8° at 1.00 THz according to equations (2.45) and (2.46). In Fig. 4.14, the theoretically predicted phase shifts were also drawn as the solid curve in order to be compared with experimental data. We can observe that the tendency of the experimental data pretty matches the theoretical curve; the slope of the data curve is very sharp from 25V to 35V. fig. 4.15 emphasizes the applied voltage axis from 25V to 35V, the experimental results have a good agreement with theoretic values.

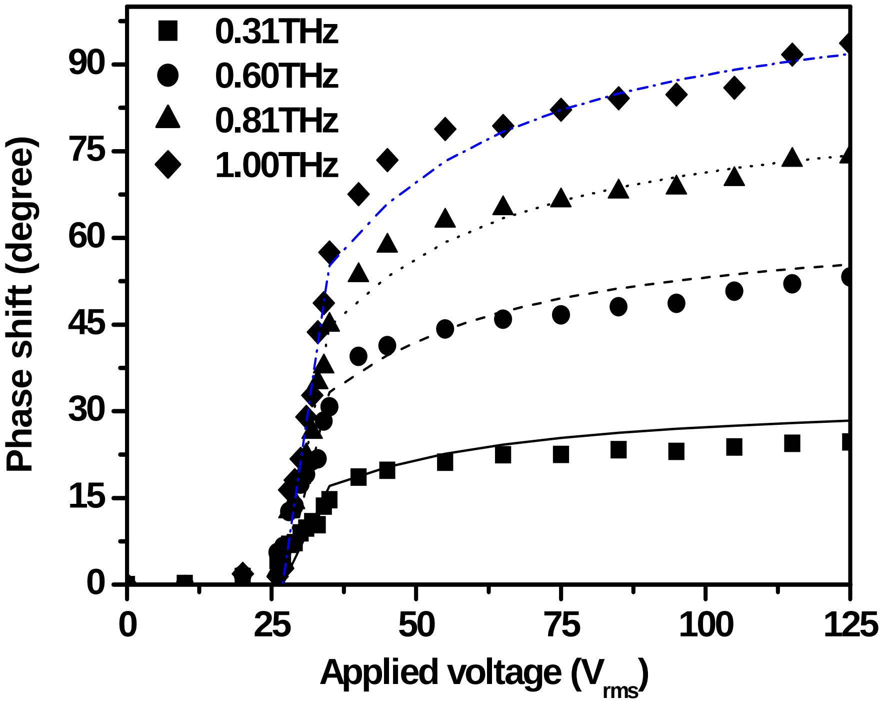

Fig. 4.14 The phase shift as a function of driving voltage for several frequencies.

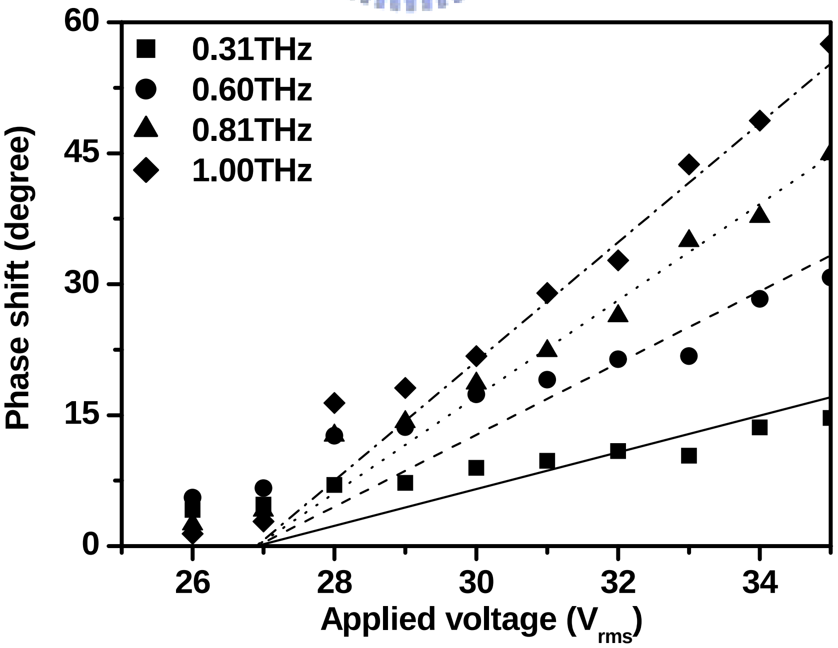

Fig. 4.15 The emphasis of fig.3.15 from 25V to 35V

We measured the response time and demonstrate the results in fig. 4.16 and fig. 4.17. By utilizing multi-meter to measure the current of the receiving antenna, we can obtain the transmitted electrical field of the NLC sample, therefore, we record the transmittance of the NLC cell with zero bias or with saturated voltage applying, respectively, and then, Bias from $0V_{rms}$ was instantaneously increased to saturation voltage ($125V_{rms}$), i.e. switch ON, the transmitted electrical field can gradually increase to the saturated state in a few seconds. According to definition, after normalizing we can obtain the demanded time as the normalized transmittance achieving 10% and 90%, the value of 90% normalized transmittance subtracts the value of 10%; we can get the rise time. The calculating result is shown in fig. 4.16. In the similar way, bias from $125V_{rms}$ was decreased to $0V_{rms}$, i.e. switch OFF, the transmitted electrical field can gradually decrease from saturated state to original state, let the 10% normalized transmittance subtracts the value of 90%, fall time can be achieved as shown in fig. 4.17. The rise time of the electrically controlled quarter wave plate is 7.5 seconds, and the fall time is 373.5 seconds.

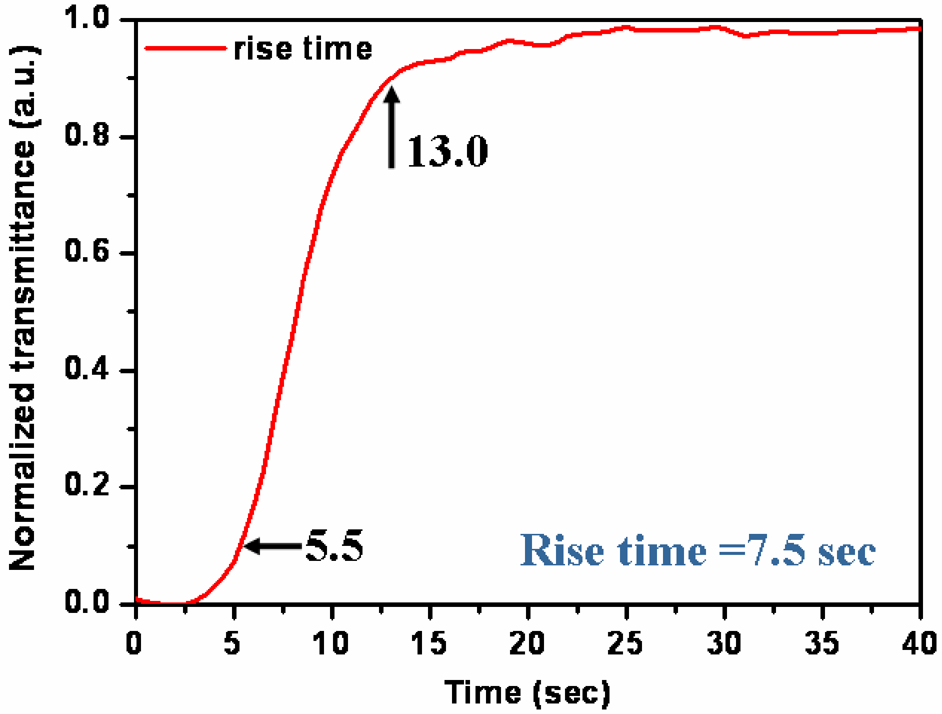

Fig. 4.16 The rise time of the NLC cell

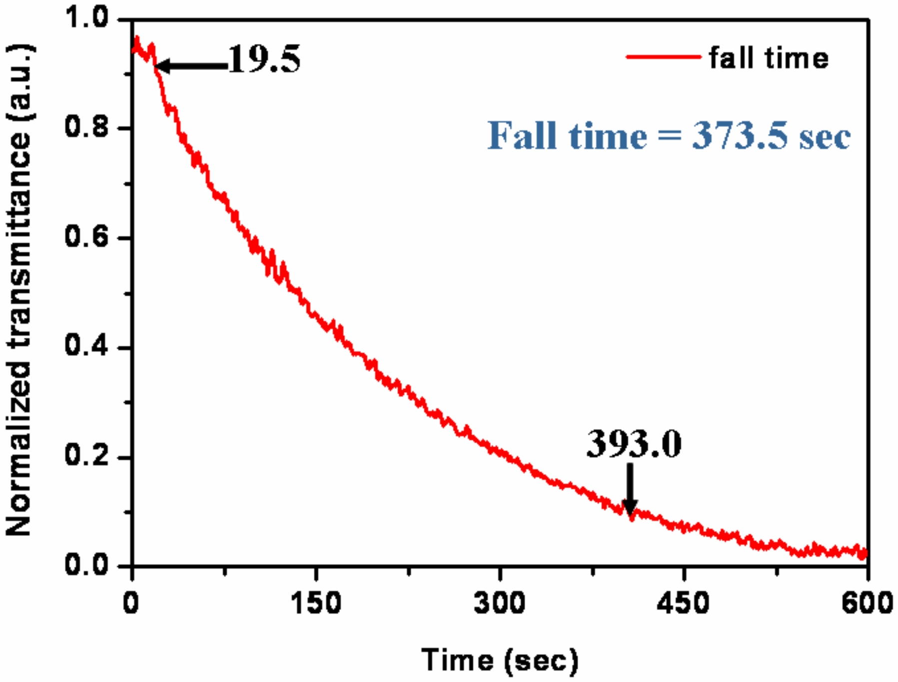

Fig. 4.17 The fall time of the NLC cell

Fig. 4.18 and fig. 4.19 illustrate the results of stabilization in this experiment, we measured the phase shift angle at 45V (rms) (linear changed area) and 125V (rms) (saturated area) for several times, and find the difference of each result. Fig.4.18 shows the original phase shift angle, by observing fig. 4.19, we could know the inaccuracy is smaller than 2°.

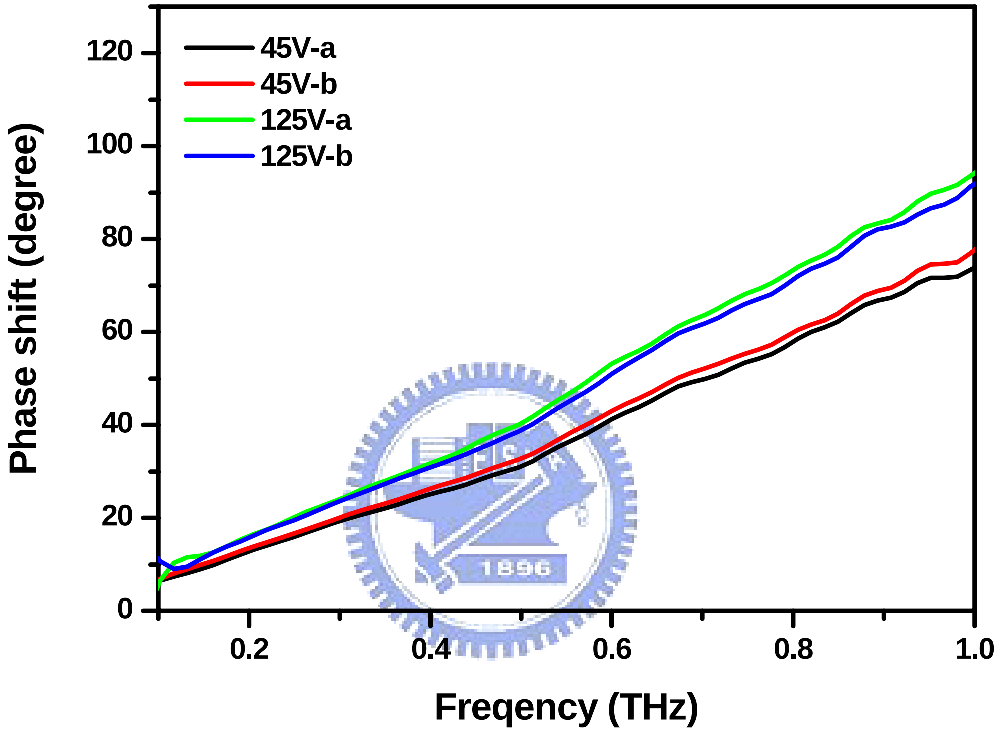

Fig. 4.18 Stabilization of shift angle at fixed applied voltage

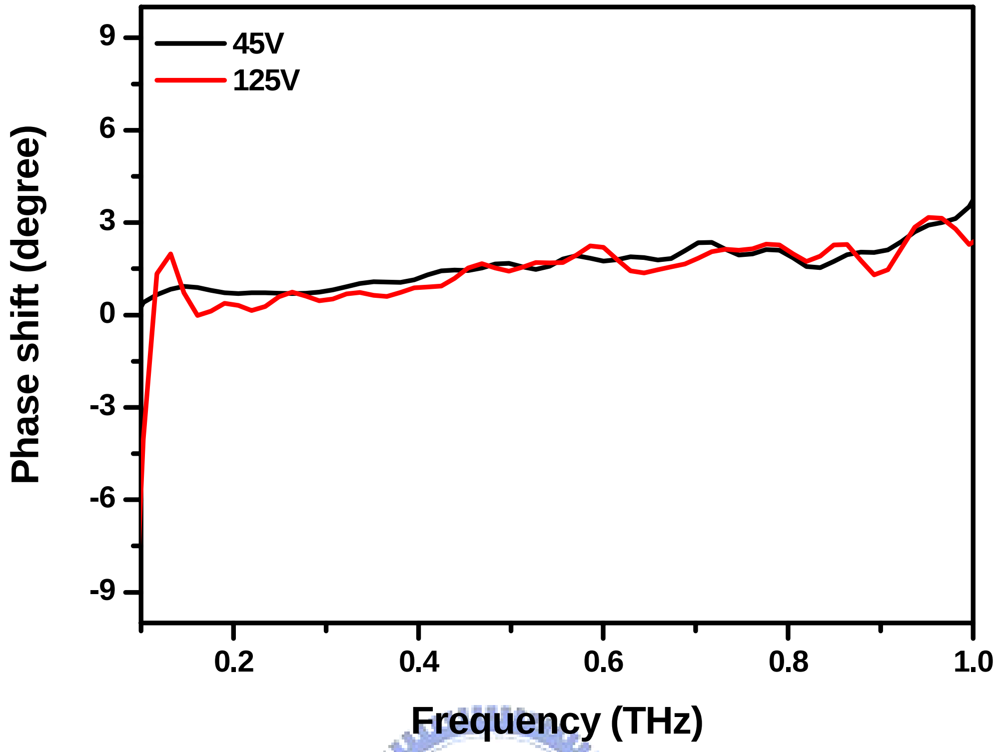

Fig. 4.19 Stabilization of shift angle at fixed applied voltage

Fig. 4.20 and fig.4.21 show the stabilization of phase shift angle with tuning applied voltage from one to another, we tuned the applied voltage from 85V (rms) to 120V (rms), after period of time (more than the rise time ) we measured the shift angle; then return to 85V (rms) and after another period of time (more than the fall time) we measured the shift angle again, repeated for several times and recorded the result in fig. 4.20, fig.4.21 shows the deviation of shift angle of fig. 4.20, it is smaller than 4°.

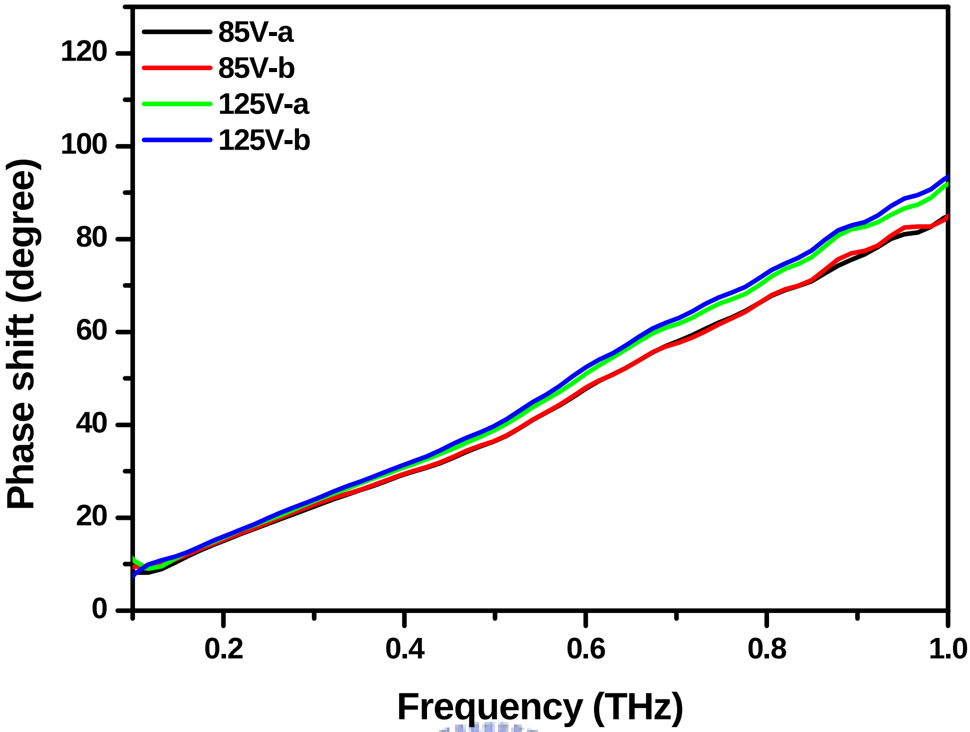

Fig. 4.20 Stabilization of shift angle after tuning the applied voltage

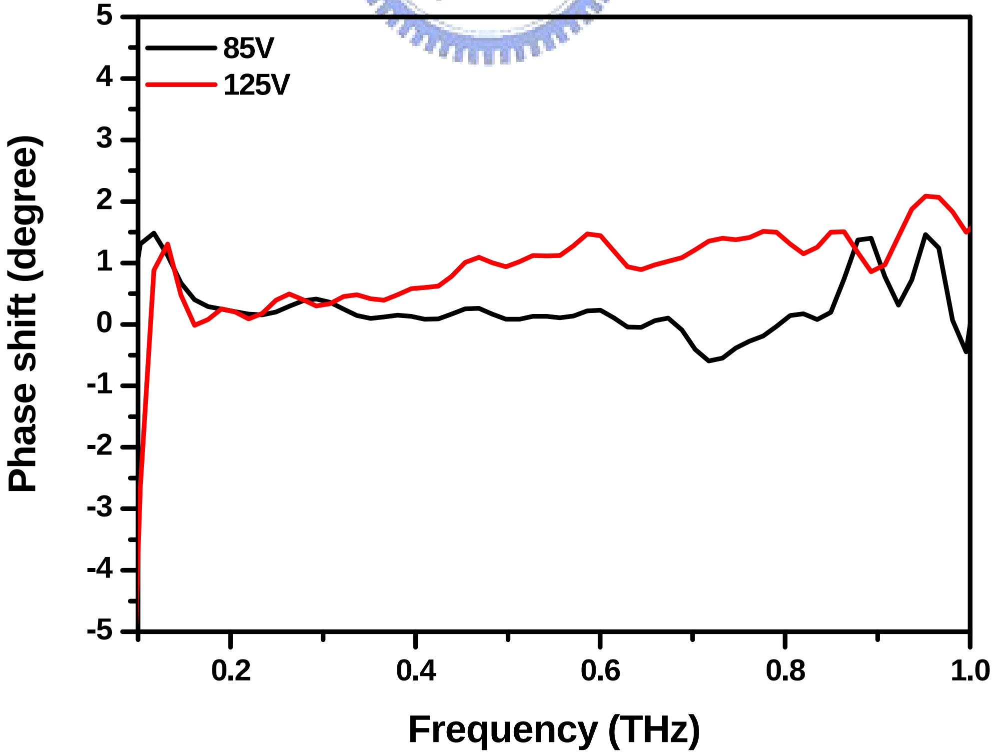

Fig. 4.21 Stabilization of shift angle after tuning the applied voltage

Fig. 4.22 shows the normalized power (at 1THz) received by the receiving antenna when we rotated our sample at different angle; we rotated our sample from 0° to 180° and measured the power every 15°. By eq. 2.xx we can draw a theoretical curve, compare with the experimental data, we can discover some deviation, we infer the deviation was produced by the instability of laser source and the scattering of our sample.

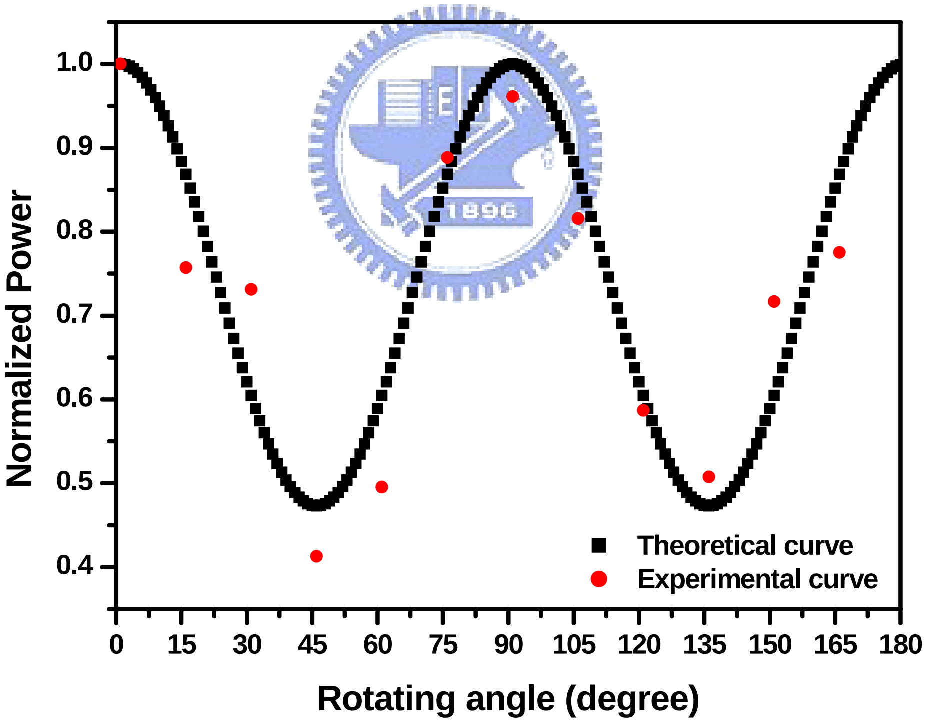

Fig. 4.22 The receiving power with rotating the sample at different angle

### 4.2.3 Compare with the Former Work

We compare the experimental data with our sample and of the former sample, and we can discover their respective characteristics and find a suitable way to use.

#### 4.2.3.1 Compare with the Electrically Controlled Sample with Gold Strip Line

Now we compare our copper electrode sample with the gold strip one. The electrical fields applied to the liquid crystal of the gold strip sample are 0V/cm, 235.7V/cm, 353.7V/cm, and 589.3V/cm, respectively. We know that with the electric field increasing, the delay in time domain moved in order backward. We can observe the space between the leftmost curve (initial voltage) and the rightmost curve (saturated voltage) is clearly distinguished. Therefore, we can predict the phase shift angle. By comparing with temporal waveforms of the gold strip sample, we can qualitatively know the phase shift angle of cooper electrode is bigger.

The transmitted THz wave spectra of the gold strip sample were obtained from the time-domain THz waveform by fast Fourier transform (FFT) algorithm. The threshold voltage required to rotate the LC occurs at 35.4 V (rms), it is slightly higher than the copper electrode sample's. The influence affected by bias voltage is similar to the effect in the cooper electrode sample. When the driving field is smaller than the threshold value, the nematic LC director will maintain their original uniform alignment. and no phase shift was observed. When the bias field is larger than the threshold value, the effective refractive index of the LC will be changed. The phase shift rises above threshold and slowly approaches a steady state value. According to eq. 2.33, the phase shift is proportional to the product of the effective index $\Delta n_{eff}$ change and frequency of the electromagnetic wave. With the same driving voltage applying, the terahertz wave experiences a larger phase shift at the higher frequencies. The phase shift will reach a saturated value when the liquid crystal is completely aligned by the applied electric field. A maximum phase shift of 4.07° was obtained at 1.07 THz when the LC cell was driven at 589.3 V/cm. Compare with the cooper electrode cell, we can find that because of the arrangement of the gold strips, even the gold strip cell fully aligned the liquid crystal molecules, the rotated angle of LC molecules does still not achieve $90^{\circ}$, therefore, higher applied voltage and amendment the structure are both important for achieving higher shift angle.

### 4.2.3.2 Compare with the Magnetically Controlled Sample

For magnetically controlled sample, THz passing through the LC phase shifter at various magnetic inclination angles ($\theta$ = 0°, 30° and 50°). The transmitted THz waves show obviously longer time delay for larger angle, $\theta$. It is because the magnitude of magnetic field is strong enough to almost fully align the LC molecules. The THz field amplitudes increase with $\theta$ for $\theta < 43^{\circ}$. This can be explained by the increasing transmittance at the quartz-LC interface according to the Fresno equations. With increasing $\theta$, the effective refractive index of LC will rise and become closer to the refractive index of quartz substrate, which is 1.95. The transmitted field amplitudes will then increase according to Fresno equations. The THz field amplitudes decrease for $\theta > 43^{\circ}$ due to partial blocking of the THz wave by the magnet. The threshold field required to reorient LC molecules in the LC cell when the magnetic field is perpendicular to the alignment direction is less then 0.01 T, which is much lower than the magnetic field employed in this work (~ 0.43 T). Compare with the cooper electrode cell, magnetic aligned cell does not have threshold voltage because the magnetic field is always the same and strong enough to align whole the LC molecules in the cell. The spectral amplitude and phase of the transmitted THz wave are also deduced from the temporal waveforms by fast Fourier transform (FFT) algorithms. The same as the situation in electrically controlled cell, the THz waves experience larger phase shift at higher frequencies as expected from eq. 2.31. The maximum phase shift achieved was 368° at 1.025 THz and $\theta = 54^{o}$. Compare with the electrically controlled cell again, the characteristic of magnetically controlled cell is aligning LC molecules by rotating the magnet to control the magnetic field; we only need to prepare a magnet and rotating it, and then we can exactly know the direction of the LC molecules and continuously control the phase shift angle.

By observing Fig. 4.23 and Fig. 4.24, we can clearly compare the magnetically controlled phase shift and electrically controlled phase shift. The magnetically controlled sample can tune the phase shift angle by rotating the magnet; the magnet can be precisely rotated by the rotating plate, and the magnetic field is high enough, so the shift angle can be continuously and accurately tuned.

For electrically controlled sample, it is more compact and practical, but restricted by accuracy of the voltage source, the applied voltage is not completely precise, unable to void some distortion, we still have difficulty to obtain the accurate tuning from 26.9 to 35 V. It is hard to control the electric field as so stable, especially under the sharp slope of the δ-V relation. That is why we need magnetic controlled one in the previous work.

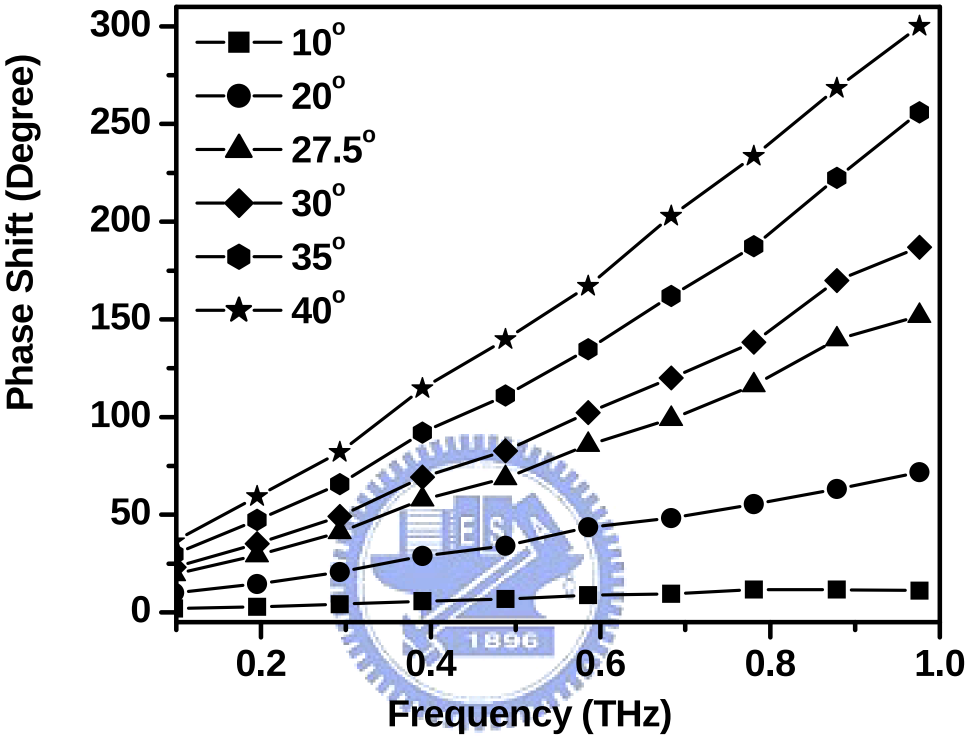

Fig. 4.23 The phase shift of the magnetically controlled sample

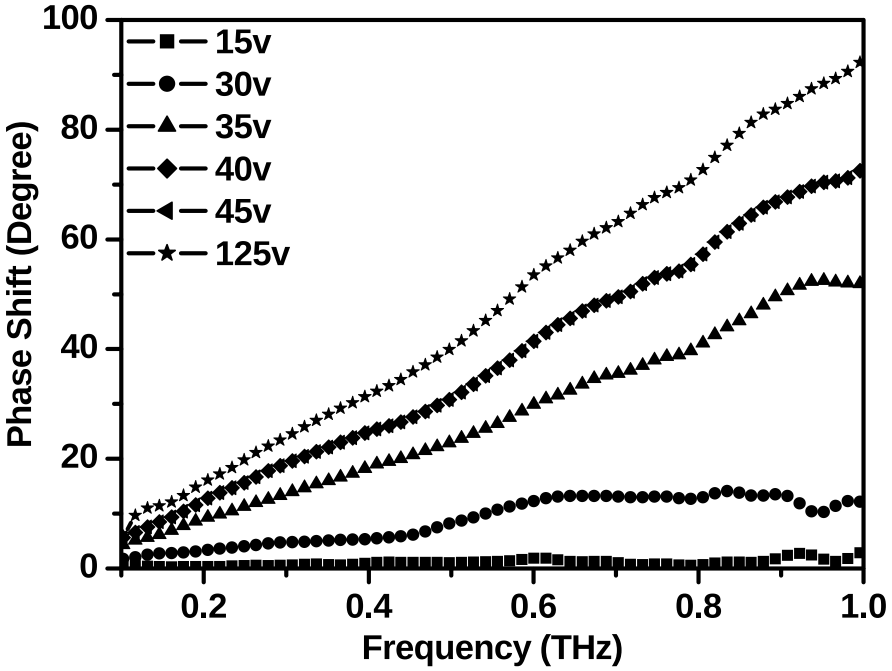

Fig. 4.24 The phase shift of the electrically controlled sample

# 5. Conclusions and Future Works

In chapter 5, we make a conclusion to our experiment and show the future work for further research and more applications.

In summary, we demonstrate the tunable room temperature π/2 NLC THz phase shifters. The phase shift with electrical controlling the effective refractive index of LC E7 layer is achieved. In addition, our measured results in this experiment are in good agreements with theoretical predictions. With the 524μm NLC cell, a maximum phase shift of 92.2° was observed at 1.00 THz when the applied voltage was driven at 125 V (rms). This device is also regarded as the tunable quarter wave plate in the THz region.

In principle, the phase shift can be increased by employing a LC cell with larger optical thickness and/or larger refract index. To achieve a 2π phase shift at 1 THz, we can increase the cell thickness to 2 mm with the same experimental setup used in this work. Alternatively, this can be realized with a 1mm-thick LC cell with Δn ~0.4.

In the future, thicker cell or larger refractive index will be adopted, to avoid the aligned problem, LC layer can not be thicker than the align limitation; therefore, double layer sample (sandwich structure) will be applied.

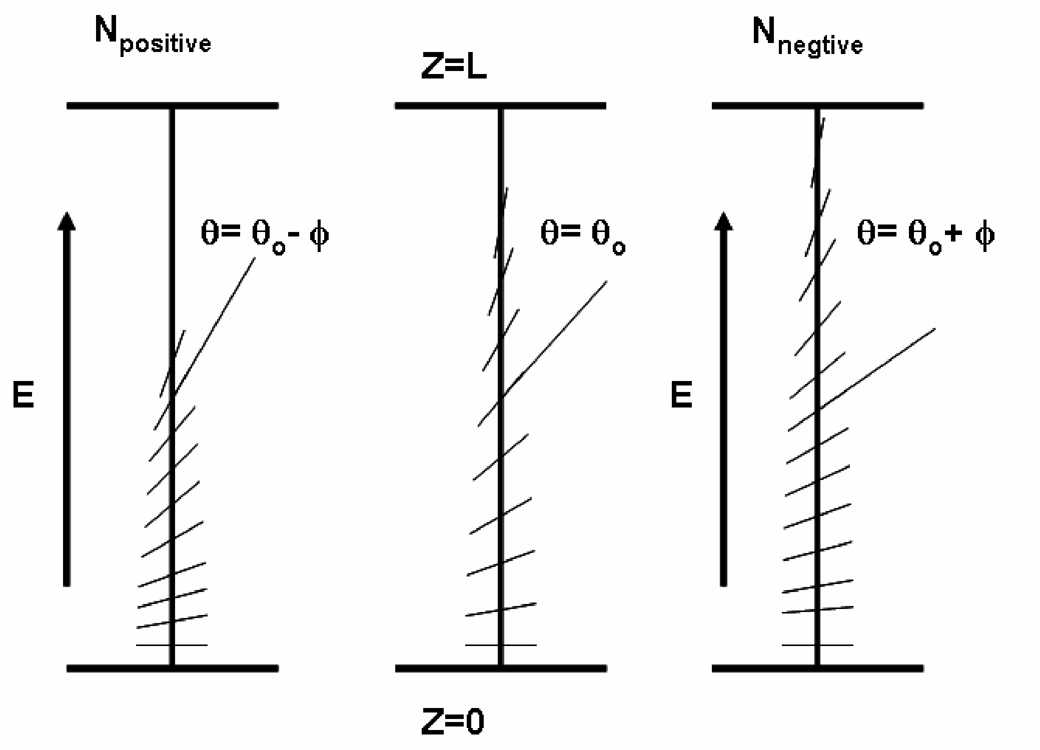

Fig. 5.1 Schematic representation of the deformation θ in the HAN cell

For tunable component, wider tunable range is necessary, it is discovered that hybrid aligned nematic (HAN) cell can decrease the slope of v-Φ curve. HAN cell has independently perpendicular and parallel boundary conditions at the substrates. Whether the used LC has positive or negative dielectric anisotropy, exhibits no threshold in the field-induced birefringence change, the slow variation of birefringence with voltage, and the spatially unidirectional director rotation with voltage. If we reform our cooper electrode NCL cell for hybrid aligned, continuously tunable phase shifter is expected, and lower applied voltage makes our sample better in power dissipation, but may deprive some shift angle, so we can choose the suitable aligned model depend on our situation. Then the well-tunable, wide-ranged, practical electrical controlled phase shifter in THz is anticipated.

# Appendices

## Appendix 1

Composition and Property of Cooper Used In this Experiment

**(1)化學成份(Chemical Composition)**

| 合金編號 | | 化學成份 (wt.%) | |
|---|---|---|---|
| **Material Designation** | | **Cu** | **P** |
| **JIS** | **C1100(ETP)** | **99.9(min)** | **-** |
| | **C1200(DLP)** | **99.9(min)** | **0.004~0.012** |
| | **C1220(DHP)** | **99.9(min)** | **0.015~0.040** |

**(2) Physical Properties**

| 合金編號<br>**(Alloy No. )** | 密度<br>**(Density)**<br>**g/cm3** | 彈性係數<br>**(Modulus of Elasticity)**<br>**(Young's Modulus)**<br>**GPa** | 熱膨脹係數<br>**(Coefficient of Thermal Expansion at 20 oC to 300 oC)**<br>**m/m · K** | 熱傳導係數<br>**(Thermal Conductivity at 20 oC)**<br>**W/m · K** | 導電率<br>**(Electrical Conductivity at 20 oC)**<br>**%IACS** |
|---|---|---|---|---|---|
| **C1100** | **8.94** | **117** | **16.9** | **391.1** | **101** |
| **C1200** | **8.94** | **117** | **16.9** | **386.0** | **98** |
| **C1220** | **8.94** | **117** | **17.1** | **339.2** | **85** |

### (3)機械性質(Mechanical Properties)

| 合金編號 Alloy No. | 質 別 Temper | 抗 拉 試 驗 Tensile test | | | 硬 度 試 驗 Hardness test |
|---|---|---|---|---|---|
| | | 厚度 Thickness (mm) | 抗拉強度 Tensile strength (kgf/mm2) | 延伸率 (50mm) Elongation(in 2”) (%) | Hv Thickness >0.15mm |
| C1100<br>C1200<br>C1220 | O | > 0.2 | < 27 | > 30 | < 65 |
| | H/4 | > 0.2 | 24~30 | > 13 | 60~80 |
| | H/2 | > 0.2 | 26~33 | > 10 | 70~90 |
| | 3/4H | > 0.2 | 29~35 | > 5 | 80~100 |
| | H | > 0.2 | 30~37 | > 4 | 90~110 |
| | EH | > 0.2 | 33~40 | > 3 | 95~110 |
| | SH | > 0.2 | 35~41 | > 2 | 100~125 |

# References

1. Chih-Yang Wang, ”Metallic Photonic Crystals for Controlling Terahertz Radiation”, 2003
2. 巫嗣文, ” THz 顯像技術之研究”, 2003
3. P.H. Siegel, “IEEE Transactions on Microwave Theory and Techniques”, 50, 910-928, 2002.
4. 洪勝富，齊正中, ”短脈衝雷射激發兆赫輻射技術及其研究”, 物理雙月刊二三卷, pp.322-328, 2001
5. Mourou G, Stancampiano C V, Antonetti A and Orszag A, “Picosecond microwave pulse generation,” *Appl. Phys. Lett.*, vol. 38, no. 6, pp. 470-472, Mar. 1981
6. Auston D H, Cheung K P and Smith P R, “Picosecond photoconducting Hertzian dipoles,” *Appl. Phys. Lett.*, vol.45, no. 3, pp. 284-286, Aug. 1984
7. Q. Wu and X. –C. Zhang, “Ultrafast electro-optic field sensors”, *Appl. Phys. Lett.*, vol. 68, no.12, pp. 1604-1606, Mar.1996
8. de Gennes, P.G. and Prost, J. “The Physics of Liquid Crystals”, 1993.
9. Pochi Yeh, Claire Gu, “Optics of Liquid Crsytal Displays”, 1999.
10. 松本正一, 角田市良, “液晶之基礎與應用”, 2002
11. I. H. Libon, S. Baumga¨rtner, M. Hempel, N. E. Hecker, J. Feldmann, M. Koch, and P. Dawson, *Appl. Phys. Lett.*, 76, 2821, 2000.
12. T. Kleine Ostmann, M. Koch, and P. Dawson, Microwave Opt. Technol. 11Lett. 35, 343, 2002.
13. R. Kersting, G. Strasser, and K. Unterrainer, Electron. Lett. 36, 1156 (2000).
14. D. Dragoman, M. Dragoman, “Terahertz fields and applications,” *Pro. in Quantum Electron.*, vol. 28, no. 1, pp. 1-66, 2004
15. P. Uhd Jepsen, R. H. Jacobsen, and S. R. Keiding, “Generation and detection of terahertz pulses from biased semiconductor antennas,” *J. Opt. Soc. Am. B*, vol. 13, no. 11, pp. 2424-2436, Nov. 1996
16. M. van Exter, Ch. Fattinger, and D. Grischkowsky, “Terahertz time-domain spectroscopy of water vapor,” *Opt. Lett.*, vol. 14, no. 20, pp. 1128-1130, Oct. 1989

17. C. Ronne, P. Astrand, and S. R. Keiding, "THz Spectroscopy of Liquid $H_2O$ and $D_2O$," *Phys. Rev. Lett.*, vol. 82, no. 14, pp. 2888-2891, Apr. 1999
18. M. Walther, K. Jensby, and S. R. Keiding, H. Takahashi and H. Ito, "Far-infrared properties of DAST," *Opt. Lett.*, vol. 25, no. 12, pp. 911-913, June 2000
19. D. Grischkowsky, S. Keiding, M. van Exter, and Ch. Fattinger, "Far-infrared time-domain spectroscopy with terahertz beams of dielectrics and semiconductors", *J. Opt. Soc. Am. B*, vol.7, no. 10, pp. 2006-2014, Oct. 1990
20. B. B. Hu and M. C. Nuss, "Imaging with terahertz waves," *Opt. Lett.*, vol. 20, no. 16, pp. 1716-1718, Aug. 1995
21. D. M. Mittleman, R. H. Jacobsen, and M. C. Nuss, "T-Ray Imaging," *IEEE J. Selected Topics in Quantum Electron.*, vol. 2, no. 3, pp. 679-692, Sep. 1996
22. M. Herrmann, M. Tani, and K. Sakai, "Terahertz imaging of silicon wafers," *J. Appl. Phys.*, vol.91, no. 3, pp.1247-1250, Feb. 2002
23. P. Y. Han, G. C. Cho, and X.-C. Zhang, "Time-domain transillumination of biological tissues with terahertz pulses", *Opt. Lett.,* vol. 25, issue 4, pp. 242-244, Feb. 2000
24. A. J. Fitzgerald, E. Berry, N. N. Zinovev, G. C. Walker, M. A. Smith, and J. M. Chamberlain, "An introduction to medical imaging with coherent terahertz frequency radiation," *Phys. Med. Biol.*, vol.47, R67-R84, Mar. 2002
25. http://www.frascati.enea.it/THz-BRIDGE/main.htm
26. Iam-Choon Khoo, "Liquid Crystals", 1995
27. Peter J. Collings, "Liquid Crystals", 2002
28. http://plc.cwru.edu/tutorial/enhanced/files/lc/external/external.htm
29. http://www.arthistoryclub.com/art_history/Liquid_crystal
30. Shiban K.Koul Bharathi Bhat, "Microwave and Millimeter Wave Phase Shifters Volume I", 1991.
31. I. H. Libon, S. Baumga¨rtner, M. Hempel, N. E. Hecker, J. Feldmann, M.Koch, and P. Dawson, *Appl. Phys. Lett.* 76, 2821, 2000.
32. Chao-Yuan Chen, Cho-Fan Hsieh, Yea-Feng Lin, Ru-Pin Pan, and Ci-Ling Pan, "Magnetically tunable room-temperature $2\pi$ liquid crystal terahertz phase shifter", *Opt. Exp.*, 12, 2630, 2004.
33. T.R. Tsai, C.Y. Chen, R.P. Pan, C.L. Pan, and X.-C. Zhang, "Room Temperature Electrically Controlled Terahertz Phase Shifter", *IEEE*

*Microwave Wireless Comp. Lett.*, 14, 77, 2004.

34. F. J. Kahn, Appl. Phys. Lett. 22, 386, 1973.
35. D. Grischkowsky, S. R. Keiding, M. V. Exter, and C. Fattinger, “Far-infrared time-domain spectroscopy with terahertz beams of dielectrics and semiconductors”, *J. Opt. Soc. Am. B*, 7, 2006, 1990.
36. M. V. Exter, C. Fattinger, and D. Grischkowsky, “Terahertz time-domain spectroscopy of water vapor”, *Opt. Lett.*, 14, 1128, 1989.